Internal void fabrication via mask projection micro-stereolithography: A rapid repeatable microfluidic prototyping technique

Paul Francis O'Neill, B.A., B.A.I

submitted as part of the degree of Philosophiæ Doctor (PhD)

from

Dublin City University,

School of Mechanical and Manufacturing Engineering

Supervisor: Prof. Dermot Brabazon

Co-supervisor: Prof. Dermot Diamond

August 2018

Declaration

I hereby certify that this material, which I now submit for assessment on the programme of study leading to the award of PhD, is entirely my own work, and that I have exercised reasonable care to ensure that the work is original, and does not to the best of my knowledge breach any law of copyright, and has not been taken from the work of others save and to the extent that such work has been cited and acknowledged within the text of my work.

Signed: _____ (Paul O'Neill) ID No.: 14210071 Date: _____

List of Publications

Journal Papers

O'Neill P. F., Ben Azouz, A., Vázquez, M., Liu, J., Marczak, S., Slouka, Z., Chang, H. C., Diamond, D., Brabazon, D., Advances in three-dimensional rapid prototyping of microfluidic devices for biological applications, Biomicrofluidics 8, 052112 (2014).[1]

O'Neill, P., Jolivet, L., Kent, N. J. & Brabazon, D. Physical integrity of 3D printed parts for use as embossing tools. Adv. Mater. Process. Technol. 698, 1–10 (2017).[2]

Kent, N. J., Jolivet, L., O'Neill, P. & Brabazon, D. An evaluation of components manufactured from a range of materials, fabricated using PolyJet technology. Adv. Mater. Process. Technol. 698, 1–12 (2017).[3]

International Peer Reviewed Conference Papers

O'Neill, P. F., Kent, N., Brabazon, D., Mitigation and control of the overcuring effect in mask projection micro-stereolithography, Proceedings of the 20th International ESAFORM Conference on Material Forming, ESAFORM 2017[4]

O'Neill, P., Barrett, A., Sullivan, T., Regan, F., Brabazon, D., Rapid prototyped biomimetic antifouling surfaces for marine applications, Advances in Functional Materials (AFM 2015)[5]

McCann, R., Freeland, B., O'Neill, P., "Nanoparticle Fabrication via Pulsed Laser Ablation in Liquid: A Step Towards Production Scale-up", Proceedings of the 20th International ESAFORM Conference on Material Forming, ESAFORM 2017

Oral Presentations

O'Neill P. F., Vázquez, M., Liu, J., Marczak, S., Chang, H. C., Diamond, D., Brabazon, D., Direct fabrication methods for high pressure micro-total analysis systems, Advances in Microfluidics & Nanofluidics (AMN), Academia Sinica, Taiwan, R.O.C, May 2014

O'Neill, P. F., Kent, N., Brabazon, D., Mitigation and control of the overcuring effect in mask projection micro-stereolithography, 20th International ESAFORM Conference on Material Forming, Dublin City University, April 2017

McCann, R., Freeland, B., O'Neill, P., "Nanoparticle Fabrication via Pulsed Laser Ablation in Liquid: A Step Towards Production Scale-up", 20th International ESAFORM Conference on Material Forming, ESAFORM 2017

Brabazon, D., O'Neill, P., McCann, R., Groarke, R., "Photonic assisted fabrication of advanced liquid UTLC and modular SPE chromatographic platforms", 31st International Symposium on Chromatography, 28 Aug – 1 Sept 2016, Cork, Ireland

Poster Presentations

O'Neill, P. F., Vázquez, M., Liu, J., Diamond, D., Brabazon, D., Direct fabrication methods for micro-total analysis systems, 9th International Conference on Surfaces, Coatings and Nanostructured Materials (NANOSMAT Dublin), Trinity College Dublin, September 2014

O'Neill, P. F., Kent, N., Brabazon, D., Mitigation and control of the overcuring effect in mask projection micro-stereolithography, Dublin City University Faculty Research Day, January 2017

Contents

List of figures

List of tables

List of Abbreviations

2D	Two-Dimensional
3D	Three-Dimensional
ABS	Acrylonitrile Butadiene Styrene
AM	Additive Manufacturing
ANOVA	Analysis of Variance
ATP	Adenosine Triphosphate
CA	Contact Angle
CAD	Computer Aided Design
CAM	Computer Aided Manufacturing
CI	Confidence Interval
COC	Cyclo Olefin Co-polymer
COP	Cyclo Olefin Polymer
DENV	Dengue Virus
DEPC	Diethylpyrocarbonate
DI	De-ionised
DLP	Digital Light Processing
DMD	Digital Micromirror Device
DRIE	Deep Reactive Ion Etching
EDTA	Ethylenediaminetetraacetic Acid
FDM®	Fused Deposition Modelling
FFF	Fused Filament Fabrication
FWHM	Full Width at Half Maximum
HPLC	High Performance Liquid Chromatography
i3DP	Ink-jet 3D Printing
IC	Ion Chromatography
IEM	Ion Exchange Membrane
IPA	Isopropyl Alcohol
LC	Liquid Chromatography
LED	Light Emitting Diode
LoaC	Lab on a Chip
LOM	Laminate Object Manufacturing
MEMS	Micro Electro-Mechanical Systems
MJM	MultiJet Modelling
MJP	MultiJet Printing
MPSL	Mask Projection Stereolithography
MPμSL	Mask Projection micro-Stereolithography
Nd:YAG	Neodymium-doped Yttrium-Aluminium Garnett
PC	Polycarbonate
PCR	Polymerase Chain Reaction
PDMS	Polydimethylsiloxane
PE	Polyethylene
PEEK	Polyether ether ketone
PET	Polyethylene terephthalate
PJ	PolyJet
PLA	Polylactic Acid
PMMA	Polymethyl methacrylate
POC	Point of Care
PP	Polypropylene

PS	Polystyrene
PSA	Pressure Sensitive Adhesive
PTFE	Polytetrafluoroethylene
PVA	Poly(vinyl alcohol)
PVC	Poly(vinyl chloride)
qRT-PCR	Quantitative Reverse Transcription Polymerase Chain Reaction
RIE	Reactive Ion Etching
ROI	Region of Interest
SEM	Scanning Electron Microscope
SL	Sterelithography
µSL	Micro-Stereolithography
SLM	Selective Laser Melting
SLS	Selective Laser Sintering
SPE	Solid Phase Extraction
STL	Standard Tessellation Language
TAS	Total (chemical) Analysis System
µTAS	Miniaturised Total Analysis System
TE	Tris-EDTA (pH buffer)
Tg	Glass transition temperature
TPP	Two-Photon Polymerisation
UV	Ultraviolet
UV-Vis	Ultraviolet-Visible
VP	Vat Photopolymerisation

List of Symbols

Symbol	Unit(s)	Equation	Name
D	J.cm^{-2}	tI	Optical energy dose
D_c	J.cm^{-2}	$T_c I_0$	Critical optical energy dose
D_n	J.cm^{-2}	$t_l I_n$	Optical energy dose received at depth z during exposure of layer n
D_{sim}	J.cm^{-2}	-	Optical energy dose numerical solution
E_{rel}	%	-	Relative error limit
h_a	µm	$1/\alpha$	Characteristic resin penetration depth
i_{max}	-	-	Maximum number of iterations
I	W.cm^{-2}	$I_0 e^{-\alpha z}$	Optical irradiance
I_0	W.cm^{-2}	-	Optical irradiance at the interface
I_n	W.cm^{-2}	-	Optical irradiance received at depth z during exposure of layer n
n	-	-	Layer index
N	-	-	Total number of layers
p_x	µm	-	DMD pixel depth
p_y	µm	-	DMD pixel width
t	s	-	Time
t_l	s	-	Layer exposure time
t_p	s	-	Polymerisation time
T_c	s	D_c/I_0	Photopolymer critical time
z	µm	-	Depth
z_l	µm	-	Build layer thickness
z_p	µm	$h_a \ln(t_p/T_c)$	Polymerisation depth
Z_{shift}	-	-	Voxel z-shift
α	µm^{-1}	-	Material absorption coefficient
γ	-	t_l/T_c	Normalised layer exposure time
δ_{in}	-	-	Input voxel array
δ_{mod}	-	$\theta_{ideal} - \phi_{\downarrow}$	Modified voxel array
δ_n	-	-	Binary solid/liquid classifier
ζ	-	z/h_a	Normalised depth
ζ_l	-	z_l/h_a	Normalised layer thickness
ζ_p	-	z_p/h_a	Normalised polymerisation depth
θ_{ideal}	-	-	Ideal solution
θ_{real}	-	-	Numerical solution
λ	-	-	Number of enclosing layers
τ	-	t/T_c	Normalised time
τ_p	-	t_p/T_c	Normalised polymerisation time
ϕ	-	$\theta_{real} - \theta_{ideal}$	Difference between ideal and numerical solution
$\phi_{\downarrow}$	-	-	Shifted difference array
Ω	-	D/D_c	Normalised energy dose
Ω_n	-	D_n/D_c	Normalised energy dose received at depth z during exposure of layer n
Ω_{sim}	-	D_{sim}/D_c	Normalised energy dose numerical solution

Acknowledgements

Firstly, I would like to acknowledge my supervisor Prof. Dermot Brabazon for your patience, advice, guidance, and encouragement in times of doubt over the last four years. Thanks also to my co-supervisor Prof. Dermot Diamond for always being available to offer advice.

I gratefully acknowledge the financial scholarship received from both Science Foundation Ireland and the Naughton Foundation. Thanks to Prof. Dermot Brabazon for encouraging me to apply for the Naughton Fellowship in my first year and to Martin and Carmel Naughton, and all at the Naughton Foundation for sponsoring and running such a great exchange program between Irish Universities and the University of Notre Dame.

A special thanks to Ronan and Brian for the countless cups of coffee (and pints of beer) when a break was needed, the PhD process would have been unendurable without you.

To my colleagues and friends Huw, Stephen, Ben, Cleo, Louis, Aoife, Claire, Adam, and David for sharing the PhD experience with me; and to Dr. Bert Ellingboe, and members of the plasma research laboratory, this research would have ‘ground’ to a halt long ago without the use of your coffee machine.

To past and present members of the Advanced Processing Technology Research Centre including Dr. Mercedes Vazquez, Dr. Nigel Kent, Dr. Robert Groarke, Dr. Shadi Karazi, Dr. Muhannad Obeidi, Dr. Inam Ul Ahad, Cian Hughes, and Dr. Komal Bagga. Thanks also to the staff in the school of Mechanical and Manufacturing Engineering in DCU and the technical staff in the Nano-bioanalytical Research Facility including Liam Domican, Michael May, Lorcan Kent, Stephen Fuller, and Josephine Ozoani.

To all in the Centre for Microfluidics and Medical Diagnostics at the University of Notre Dame, in particular Prof. Hsueh Chia Chang, Assistant Prof. Satyajyoti Senapati, Dr. Sunny Shah, Dr. Yongfan Men, and of course the newlyweds Drs Steven and Chun-Mei Marczak for making my time at Notre Dame so enjoyable.

To my friends Aran, Niall, Alexi, Mike, Leddy, Kev, Mick, Annie, Niall, Jill, and many others near and far, for keeping me grounded and giving me perspective of life

beyond academia. Thanks also to Booka Brass Band for giving me a creative outlet outside of the lab.

I could not have completed this PhD without the constant support and encouragement of my girlfriend Gemma. Thanks for being my partner in crime, for showing me the way, and for putting up with me over the last three years; without you this would not have been possible.

To my brothers Dermot and James, thanks for being by my side through thick and thin, I know I can always rely on you.

Finally, I owe this PhD to my parents. To my late father Frank, who passed away suddenly before publication of this final version yet whose encouragement and faith was instrumental in seeing this thesis through to completion, thank you and for teaching me the importance of honesty, perseverance and humour; and to my mother Rena, whose unwavering strength and compassion have always kept me going through difficult times, thank you for your patience and guidance. Thank you both for giving me every possible opportunity in life, I am eternally grateful.

To my mother Rena,

for your strength and guidance in difficult times

and to my father Frank,

for teaching me the importance of perseverance.

Abstract

Miniaturisation of common laboratory techniques has gathered significant interest in the last few decades with both academic and industrial researchers seeking to reduce waste, sample volume, and limits of detection for a wide range of applications. These goals present a unique challenge that originally spurred the creation of the multidisciplinary field of microfluidics in the 1980s. In the same time-frame 3D printing has progressed from its inception by Charles Hull in 1983 and developed into a common industry technique used at the design and prototyping stage of product development. 3D printing is now also used in custom end-user products in automotive, aerospace, and biomedical industries. Despite this, achieving internal features and voids at the micro-scale via 3D printing remains a major challenge.

In this thesis, Mask Projection micro-Stereolithography (MPμSL) was used as a fabrication method for the production of microscale internal voids and features toward achieving an ultra-rapid prototyping method for microfluidic applications. MPμSL is an ideal replication method for microfluidic applications as the working material is a liquid photo-polymer resin and thus can be removed from internal structures with relative ease. In addition, unlike classical multi-step fabrication methods that are prone to delamination, MPμSL enables the production of micro-scale capillaries capable of withstanding higher pressures in a single step.

MPμSL build quality, channel reproducibility, channel size and channel shape were examined, and process limitations were characterised. The so-called ‘overcuring’ of the liquid polymer resin presents the main obstacle in the creation of microscale channels and features using this technique and hence was a primary focus of this thesis. Material characterisation techniques used to determine the nature of the photopolymer materials were applied and a mathematical model was developed and applied to predict areas where overcuring is likely to occur. This model forms the basis of the novel design algorithm developed in this thesis to mitigate for the overcuring effect. Finally, the new algorithm was applied to the production of internal features. The resulting increased control over microchannel dimensions and improvement in repeatability of the technique was quantified.

Chapter 1
Introduction

1.1 Overview

Microfluidics plays an important role in an ever-expanding number of industries and disciplines including, but not limited to, synthetic and analytical chemistry, biochemistry, and biology. Despite this, design and fabrication of such microfluidic systems has remained largely unchanged since the introduction of soft lithography in the early 90's. This is especially true in academia, where soft lithography via moulding in polydimethylsiloxane (PDMS) has become the de-facto microfluidic prototyping method. However, the multi-step nature of this method is problematic in many applications where fast concept-to-chip prototyping intervals are required for efficient experimental throughput and optimization. Additive manufacturing (AM) also known as three-dimensional (3D) printing offers a solution to this problem.

AM is changing the field of microfluidics, requiring less equipment, labour, and processing time than conventional methods. However, there are still several problems that need to be addressed with current 3D printing methods. Firstly, the resolution of current 3D printing techniques is generally limited to the macroscopic regime, with a few notable exceptions, with typical best commercial accuracies providing layer thickness capabilities of ~16 µm at high cost, as is the case for Stratasys' PolyJet (PJ) and 3D Systems' MultiJet Modelling (MJM) 3D printing methods. Although these devices can deposit very thin layer thickness, lateral accuracies are typically less with best achievable wall thicknesses for example being 600 µm for state of the art ultraviolet (UV) 3D printing equipment. Secondly, 3D printing methods are predominantly concerned with creating external features; thus, it becomes difficult to produce fluidically sealed internal channels and voids necessary for microfluidic devices. Support material presents an obstacle in the case of microfluidic channel fabrication; post-fabrication the support material bound into micro-scale channels during the build cannot be fully extricated.

Of the currently available AM techniques, stereolithography (SL), also sometimes referred to as micro-stereolithography (μSL) offers the most promise for the creation of polymeric microfluidic channels[6]. This technique is a layer-on-layer process where photocurable resins are used to build up strong covalently bound components in a single step enabling automated production of complex 3D shapes at low to medium volume throughputs[7].

μSL is well suited to microfluidic chip fabrication for a number of reasons:

- The working photopolymer material is liquid and is thus easily removed from internal structures.
- There is no need for support structures for micro-scale internal features.
- Equipment is cost effective, and small-sized offering an exceptionally high resolution-to-cost ratio[1,8].
- Fabrication speeds offer low to medium throughputs enabling prototyping of components at faster speeds when compared with traditional fabrication methods[7,9].
- Feature size limits range from as low as 10 μm to ~75 mm in the same build, ideal for microfluidic applications where connections from macro- to micro-scale are needed.
- A wide range of photopolymer materials are available with a variety of material characteristics including biocompatibility, high strength, rubber-like materials, temperature resistance, chemical resistance, and optical transparency.

Despite these strengths, fabrication of microfluidic channels <500 μm in diameter is challenging due to inadequate control of the photopolymer cure depth in the *z*-direction, resulting in the so-called 'overcuring effect'. Penetration of the curing light through the enclosing channel layers often causes the resin inside the internal channel void to cure in place blocking the channel and resulting in poor *z*-resolution[4,8,9]. Current research in this area aims to address these limitations via improvements in SL hardware[10,11], and by doping the photopolymer material with a chemical light absorber[12–14].

In this thesis, a third approach is taken to solve the problem of overcuring. This approach is based on a novel design algorithm developed in the current work.

1.2 Objectives

The main objective of this work is to address the limitations in the direct production of internal microfluidic channels via the MPμSL 3D printing method.

The main objectives of this thesis include:

- To investigate MPμSL for fabrication of internal microfluidic channels in a bulk substrate material in a single step.
- To develop a rapid prototyping technique for common laboratory-based microfluidic geometries.
- To address the limitations in the direct production of internal microfluidic channels via the MPμSL 3D printing method.

1.2.1 Thesis outline

The structure of this PhD thesis comprises seven chapters in total beginning with an initial investigation into the use of the MPμSL technique for fabrication of internal microfluidic channels in a single step and culminating in a new design algorithm that facilitates high resolution production of internal channels via this technique. The contents of each chapter are highlighted below.

Chapter 1 – The aim of this chapter is to provide an overview of the project and to introduce the reader to the main objectives of the thesis.

Chapter 2 – This chapter reviews the necessary background theory and reveals previous work carried out in the field, highlighting the current shortcomings and need for further study.

Chapter 3 – The MPμSL 3D printing technique is used for fabrication of a new solid phase extraction pretreatment device for nucleic acid purification demonstrating the ability of this technique for rapid prototyping of microfluidic devices. Limitations of resolution in the *z*-direction due to overcuring are overcome by orienting the device in the vertical direction on the build plane.

Chapter 4 – In this chapter the MPμSL technique is applied to the fabrication of microfluidic channels. Dimensional accuracy and limitations of the technique in creating microfluidic channels are characterised. The suitability of the technique toward fabrication of end-use microfluidic devices is assessed.

Chapter 5 – A novel design algorithm is developed to mitigate for the effects of overcuring in the MPμSL technique. Characteristics and limitations of the new algorithm are assessed.

Chapter 6 – The new design algorithm developed in Chapter 5 is applied in the design of microfluidic channels to mitigate for the overcuring effect in MPμSL. Microfluidic channels are designed, and the algorithm is applied to generate mitigated microfluidic models. Mitigated and unmitigated models are compared, and results are presented and discussed. Repeatability of the new technique in creating internal voids shows a marked improvement on previous methods.

Chapter 7 – This chapter offers a summary of the thesis highlighting important findings and concludes by providing direction for future research.

Chapter 2

Literature review

2.1 Microfluidics

Microfluidics is defined as the study of flows that are simple or complex, mono- or multiphasic, circulating in artificial microsystems[15]. As a discipline, it falls under the broader heading of MEMS (micro electro-mechanical systems), a term coined in the 1980s as the advent of new fabrication technologies brought about a size reduction in many mechanical and electronic systems. Historically microfluidic systems were only used in the processing of silicon chips for the computer industry, however the field took a leap forward in the 90's with the advent of inkjet printing which spurred further research and innovation in microfluidics. Since then microfluidic systems have become widespread, evolving from single-function devices to complex multiple-function analytical systems also known as micro-total analysis systems (μTAS)[16], and encompassing an ever expanding range of disciplines from biological and chemical sciences, to physical sciences and engineering. Beginning with applications including electrophoretic separation systems[17–19], micro pumps, micro mixers [20], and centrifugal separation systems [21,22], the field has spread to biological applications in clinical and forensic analysis[23], proteomics and metabolomics[16], immunoassays[24], cell analysis[16], point-of-care (POC) diagnostics[16], drug discovery[25], genetic analysis[26], and organs-on-chip[27–30].

Operating at the micro scale offers huge advantages to scientists and medical professionals including the capability of:

- streamlining complex assay protocols
- providing investigators with accurate manipulation of the cell microenvironment
- reducing the sample and reagent volume, maximising the information obtained from samples and particularly from precious samples
- reducing costs.

2.1.1 A brief history of microfluidics

The development of microfluidic systems began with the creation of the field of MEMS in the 1980s. This in turn had been spurred on by the development of silicon processing techniques in the microelectronics industry. MEMS are defined as electromechanical systems whose total size varies between 1 and 300 micrometers[15], however for most practical applications including microfluidics, MEMS devices exist outside of this size range extending from the submicrometric scale to larger than 300 micrometres. The main goal of MEMS lies not in the creation of new sensing methods but in the integration of many elements onto a single chip including detection, information analysis, and signal processing, although novel sensing methods and platforms are often a welcome by-product. In addition, the micro-fabrication methods adapted from the semiconductor industry can easily be reproduced by the millions and at low cost, a critical aspect to the success of many devices. One such early industrial success of MEMS technology was an integrated accelerometer for detection and deployment of airbags in automobiles[15].

MEMS took another leap forward in the 1990s with the invention of inkjet printer heads, thus spurring the creation of the field of microfluidics in the process. It was in 1990 that Manz et al.[31] published the seminal paper on miniaturised total chemical analysis systems, thus creating the field of μTAS. The μTAS acronym is also commonly associated with the expansion of the term 'micro-total analysis systems' with both terms being used interchangeably. Figure 2.1 outlines the concept of μTAS as proposed by Manz et al.[31].

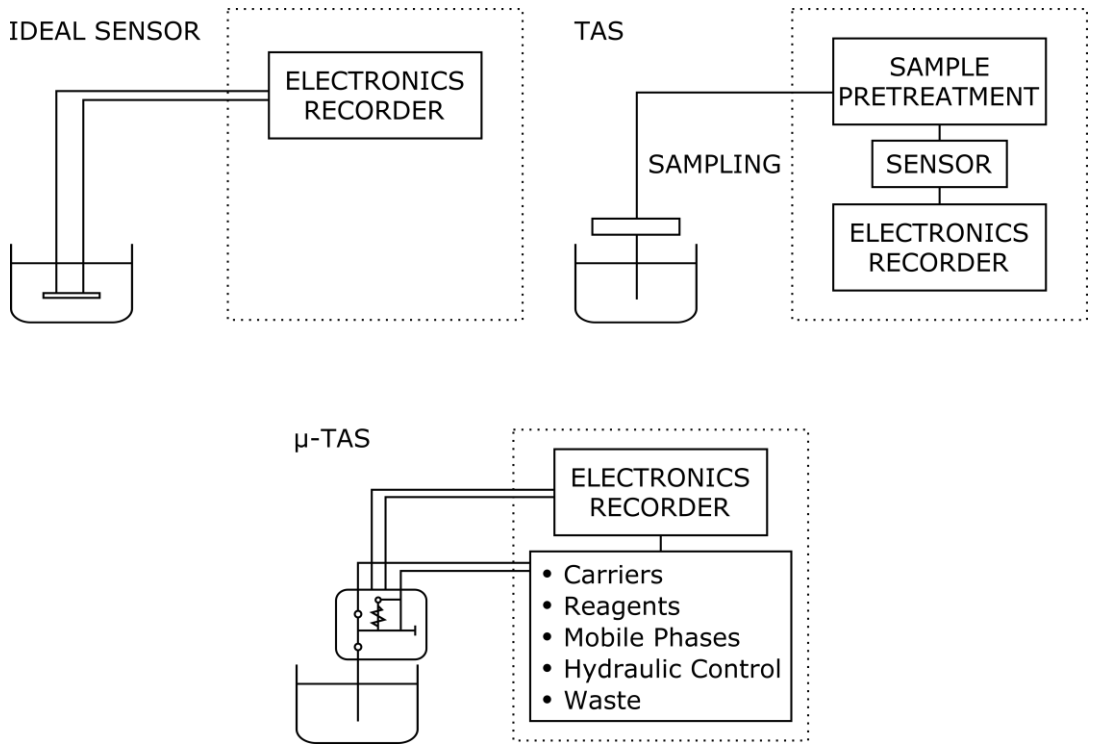

Figure 2.1. Schematic diagram of the concept of an ideal sensor, a 'total chemical analysis system' (TAS) and a 'miniaturised total chemical analysis system' (μ-TAS) adapted from the 1990 publication by Manz et al.[31].

The concept proposed by Manz was one of a miniaturised total chemical analysis system for automating common time- and labour-intensive laboratory techniques, such as chromatography, by integrating sample pretreatment, mixing, separation, detection, and calibration in a single modular platform. The proposed devices would be miniature and monolithic, with networks of interconnected microchannels integrated into the planar substrate surfaces replacing the tubing and fittings needed in conventional systems. In addition, the theoretical performance of chromatographic and electrophoretic separation systems increases with a reduction in microchannel size leading to faster separations, shorter transport times and a reduction in consumption of the carrier, reagent or mobile phase. It is important to note that the enhancement of analytical performance, rather than miniaturisation, is often cited as the main goal of μTAS[31]. As a result, most μTAS devices could be thought of as chip-in-a-lab systems, often being connected to large peripheral pumping and detection apparatus.

It was only after 1990 that miniaturisation of laboratory techniques began to gather speed. In the ensuing decade, a range of microfluidic systems were fabricated

including electrophoretic separation systems, electro-osmotic pumping systems, micro-mixers, DNA amplifiers, cytometers, and chemical microreactors[15]. These microfluidic devices enabled researchers to *act* at the micrometre scale where previously they were only able to *observe*. Thus, microfluidics is an enabling technology in many fields and can be accredited with many discoveries on the molecular scale.

It is only since the late 1990s that the terms "Microfluidics" and "Lab-on-a-chip" (LoaC) began to replace the term μTAS. "Microfluidics" became a general term to describe the manipulation of all fluids at the micro-scale while the term "Lab-on-a-chip" represented the concept of a miniaturised portable analytical device that performs all sample handling, chemical functions, and detection in a monolithic sample-to-answer device. Figure 2.2 describes the relationship between the different terminologies.

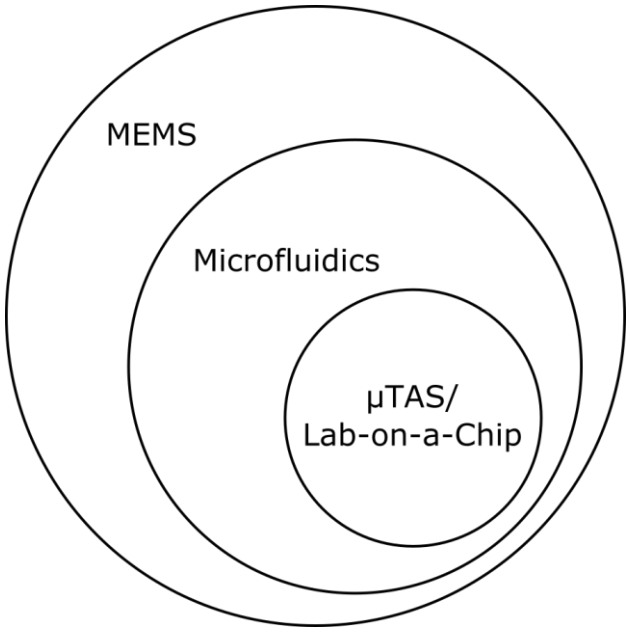

Figure 2.2. A Venn diagram showing the relationship between the different micro-scale device categories.

2.1.2 Applications of microfluidic devices

Today the field of microfluidics has matured with less time being spent on development of microfluidic devices and more time spent on the investigation of concrete applications. Common commercial applications of microfluidics include:

inkjet printing heads, glucometers for measuring concentration of glucose in the blood, pregnancy tests, DNA sequencing using high throughput droplet microfluidics, and capillary electrophoresis – mass spectrometry (CE-MS). Despite this, microfluidic device development is mainly limited to well-equipped industrial laboratories due to the prohibitive cost of microfluidic fabrication techniques.

2.2 Traditional microfluidic materials and fabrication methods

2.2.1 Materials

The first microfluidic devices were fabricated in silicon and glass using techniques adopted from the semiconductor industry, namely photolithography and etching. These techniques are complex and time consuming, consisting of a multi-step process and requiring clean room facilities and highly trained staff. As a result, soft-lithography in PDMS and laminate object manufacturing using thermoplastics are more popular in modern labs[32] enabling prototyping of microfluidic devices in a shorter time period. In fact, use of polymeric materials for the fabrication of microfluidic devices has grown exponentially in the last decade due to the availability of a wide range of new polymer materials and processing methods. These 'soft' technologies are attractive as they enable rapid prototyping. Compared with silicon, polymers can be optically transparent allowing integrated on-chip flow visualisation and optical detection on the microfluidic platform. Furthermore, transfer of the initial idea from prototype to market is facilitated using polymeric materials in the initial design due to the scalability of polymer processing techniques such as injection moulding.

PDMS remains the most common polymeric substrate for microfluidic devices since the advent of soft lithography in the late 90's[33,34]. In comparison to silicon and glass materials, PDMS is relatively cheap, permeable to gases (which is important for cell culture applications[35]), biocompatible, and enables fast prototyping of new designs. Thermopolymers such as polymethylmethacrylate (PMMA), polyethylene terephthalate (PET), polycarbonate (PC) are commonly used to create microfluidic devices via Xurography[36], laminate object manufacturing (LOM)[37,38], injection moulding[39], precision micromachining[40], or a combination of these techniques. These thermopolymer materials are popular due to their low cost, availability and high

optical transparency. A range of newly developed cyclo olefin polymers (COP) and co-polymers (COC) have gained traction amongst the microfluidic community due to their high chemical resistance to a variety of organic solvents, high optical transparency, biocompatibility, and low water absorption[41,42]. Although not widely used for microfluidic device fabrication, thermoset photopolymer materials have recently gained prevalence due to their high chemical resistance, wide range of mechanical properties, stability at high temperatures, and ability to fabricate using common AM methods[43,44].

Recently, paper-based microfluidic analytical devices (μPAD) have emerged as a low-cost alternative for point-of-care diagnostics in resource constrained settings[45–48]. The emergence of this low-cost alternative represents a change in the field from complex fabrication techniques toward simple cost-effective methods with shorter lead times.

2.2.2 Fabrication methods

Traditional microfluidic fabrication methods in silicon and glass consist of micropatterning of the substrate material to form the microchannel structure, followed by a bonding step to create a fluidically sealed device. Micropatterning techniques most commonly employed in the field of microfluidics include photolithography[49], etching[50–52], soft lithography[33,34,53,54], hot embossing[55–59], injection moulding[60,61], precision micromachining[40], and laser ablation[62,63].

2.2.2.1 Replication methods

Photolithography, the enabling technology of microfabrication, is characterised by the patterning of a liquid photopolymer material (the photoresist) with light. This is achieved by projecting light through a high-resolution photomask printed on transparent glass or polymer material onto a thin film of photoresist that has been spin-coated on a silicon or glass substrate. The photoresist forms a strong chemically resistant, protective layer masking the material during the etching step. SU-8, a high-sensitivity, high-contrast, epoxy-based negative tone photoresist is commonly used for microfluidic device fabrication, offering good mechanical, chemical, and thermal material properties as well as biocompatibility and transparency to visible light above 360 nm[50,64–66]. Common etching techniques include wet and dry etching, and reactive ion etching (RIE)[51,52]. Deep reactive ion etching (DRIE)[67] is used to form deep

channels with high aspect ratio compared to RIE. Low throughput, high running costs, the need for skilled operators, and the requirement for cleanroom facilities are significant drawbacks of the photolithography technique, limiting the manufacturability of the resulting microfluidic devices[9].

Soft lithography[33], based on the principle of photolithography, was the first technique to allow fabrication of microfluidic structures in an elastomeric material (PDMS) in less than 24 hours. First a photolithography mask with the channel design is printed on a transparency by a high-resolution printer. A positive relief photoresist is spun and exposed to light through the transparency. After development of the photoresist, PDMS is cast against the resulting pattern to form the microfluidic channels. Finally, the PDMS surface is oxidised in an oxygen plasma and brought into contact with a flat surface sealing irreversibly with PDMS, glass, silicon, silicon dioxide, or oxidised polystyrene[34]. The soft lithography fabrication process is shown in Figure 2.3. This method has since been used to fabricate multilayer microfluidic devices with three-dimensional channel networks[68,69].

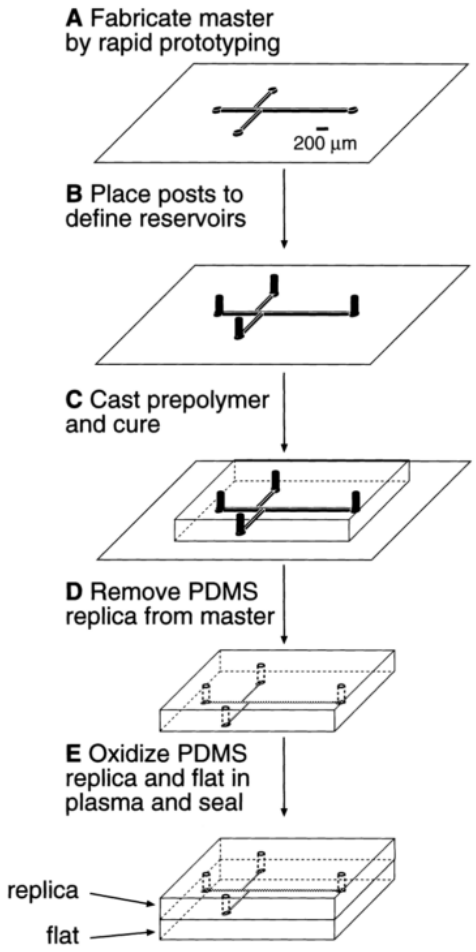

Figure 2.3. Fabrication of microfluidic channels in PDMS via soft lithography as reported by Duffy et al [34]. The soft lithography technique represents the first step toward rapid prototyping of microfluidic devices.

Hot embossing is a popular technique for microfluidic device fabrication due to the ability to form high-resolution structures in thermopolymer substrates[55–59,67,70–72]. Despite the initial high cost of equipment, hot embossing offers fast fabrication times and lends itself to scale up for high volume applications. As a first step, the thermopolymer substrate is heated to a temperature above its glass transition temperature (*Tg*) (see Table 2.1). The molten thermopolymer is then pressed against the master replica under vacuum and allowed to cool to a temperature just below *Tg*, after which demoulding is performed. Production of nano-scale features in thermopolymer materials for applications in nano-fluidics has also been reported[57,59].

Table 2.1. *Tg* for common thermopolymers used in microfluidic device fabrication.

Amorphous Polymer	***Tg* (°C)**
Polylactic acid (PLA)[73]	59
Poly(ethylene terephthalate) (PET)[73]	72
Poly(vinyl alcohol) (PVA)[73]	80
Poly(vinyl chloride) (PVC)[73]	83
Polystyrene (PS)[73]	100
ZEONOR® Cyclo-olefin polymer (COP)[74]	100-102
Polymethyl methacrylate (PMMA)[73]	105
Polycarbonate (PC)[73]	108 - 187
Polytetrafluoroethylene/Teflon (PTFE)[73]	119
ZEONEX® Cyclo-olefin polymer (COP)[75]	123 - 156
Polyether ether ketone (PEEK)[73]	146

Injection moulding has the capability to produce high quality microfluidic devices with optical grade surfaces and the ability to scaleup to high volume manufacturing[40,61]. However, use of injection moulding in microfluidic device development is limited mainly to industry and microfluidic service bureaus due to the high initial cost of tooling which is a barrier to entry for most microfluidic labs[76]. The process begins with pellets of the raw thermopolymer material which are fed into the injection chamber via a heated screw mechanism. The polymer melt is then injected into the mould cavity under high pressure. The temperature required at this point in the process depends on the type of polymer used and can range from ~ 200°C (for PMMA and PS) to ~ 280°C (for PC) and up to ~ 350°C (for PEEK) at the higher end[77]. The mould cavity contains the master structure, usually machined in a metal or ceramic heat-resistant material. To fabricate high-resolution microscopic features, it is necessary to heat the mould cavity close to the melting point of the polymer material to promote polymer flow into small structures on the surface of the mould. This type of injection moulding process is called Variotherm, and results in longer cycle times than standard macroscopic cold-cavity moulding due to the addition of extra heating and cooling cycles. Typical microinjection moulding production times are between 1-3 min per cycle[77].

The dimensional accuracy of this technique is a significant advantage enabling integration of high tolerance robust microfluidic interconnects for high pressure applications. This was demonstrated by Mair et al.[42] who achieved operational pressures up to 15.6 MPa. In addition, the ability to scale up to high volumes makes injection moulding an ideal candidate for manufacture of medium- to high-volume, disposable microfluidic cartridges[60,61]. Figure 2.4 shows an injected moulded disposable smart LoaC developed by Ahn et al.[61]. Injection moulding is an ideal candidate for disposable point-of-care microfluidic applications due to the ability to fabricate devices at high volume throughput and at low cost.

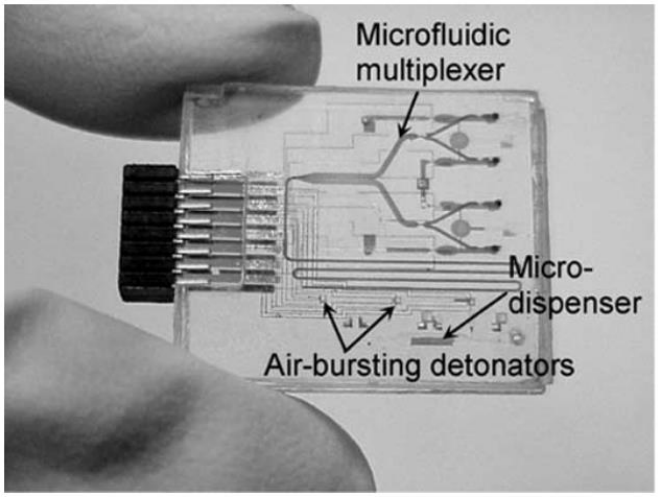

Figure 2.4. An injection moulded, disposable LoaC device for applications in clinical diagnostics and point-of-care testing[61].

2.2.2.2 Chip bonding

Bonding of substrate layers to enclose channels still remains one of the most critical and inconsistent steps in microfluidic chip fabrication. The two main techniques currently used to encapsulate open microfluidic channels include solvent-assisted and thermal-fusion bonding.

Solvent vapour bonding is a technique used to bond polymers while simultaneously reducing surface roughness as a side effect[40]. This technique has been used extensively in the literature to bond substrates including PMMA and COP/COC[40,41,78,79]. The procedure involves exposing the substrate to an appropriate solvent vapour

(chloroform for PMMA, cyclohexane for COC)[40]. Figure 2.5 presents scanning electron microscope (SEM) images of PMMA (Figure 2.5 (A)) and COC (Figure 2.5 (C)) microchannels before and after solvent exposure to chloroform (Figure 2.5 (B)) and cyclohexane (Figure 2.5 (D)) respectively.

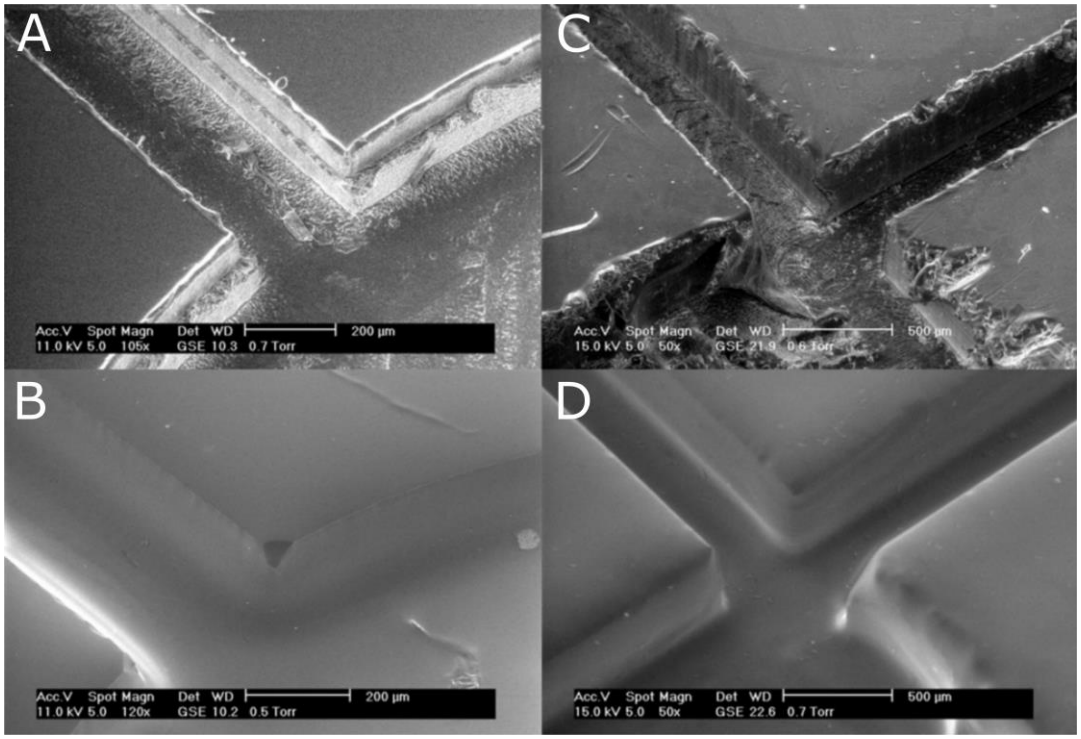

Figure 2.5. SEM images of a microchannel demonstrating the smoothing effect of exposure to a solvent vapour; (A) PMMA post-milling; (B) PMMA after 4 min chloroform solvent vapour and 30 min 60°C heat cycle; (C) COC post-milling (D) COC after 4 min cyclohexane solvent vapour and 30 min 60°C heat cycle[40].

Mair et al.[78] developed a solvent vapour bonding method at room temperature capable of producing high quality bonds, enabling chips resistant to pressures as high as 34.6 MPa. Although demonstrated only on COC chips, the technique is generic and can easily be applied to the bonding of chips made of other plastics such as PMMA, polyethylene (PE), and polypropylene (PP).

Thermal fusion is one of the most popular bonding techniques for sealing the channels of plastic microfluidic chips due to ease of implementation and reduced risk of delamination. It involves increasing the temperature of the substrate to or above *Tg* of the material while applying pressure to bond the substrate surfaces together. As the

plastic chip is heated close to or slightly above *Tg*, the entire substrate becomes soft and very sensitive to small heterogeneities in load distribution during the bonding process, this requirement is difficult to achieve as the chip, bonding jig, and plates of the bonding press must all be precisely parallel across the length of the chip[78]. Precise control of all bonding parameters is essential in order to minimise deformation of the microfeatures, especially for low aspect ratio channels and thin substrates.

2.2.2.3 Direct fabrication methods

Direct structuring of polymer substrates is made possible by a range of micromachining techniques including micromilling[79,80], xurography[36,41], laser ablation[81] and micro-Stereolithography.

Micromilling is a material removal technique that enables fast prototyping of microfluidic devices by milling the substrate surface using a precision cutting tool. Cutting tools are available in a wide variety of sizes allowing both macro- and micro-scale features to be cut in a single device. This technique is also used for fabrication of replication masters in soft lithography, hot embossing, and injection moulding providing faster fabrication than lithography and etching but at lower resolution[80].

Xurography[36] is a low-cost technique adopted from the graphic design sector used to rapid prototype microfluidic channels in thin polymer or paper substrates that are then thermally laminated or sealed via adhesive or solvent bonding[82]. Positive and negative structures can be fabricated using this method in polymer films ranging from 25 - 1000 μm thick[36]. Using this method, 3-D layered channels for microfluidic devices can be produced (Figure 2.6). This technique has been successfully employed with a range of materials including pressure sensitive adhesive (PSA)[83,84], PMMA[85], PC[86], PET[84], COP[41] and PVC[36] for fabrication of microfluidic platforms with minimum channel width as low as ~ 78 μm[36]. In addition, this technique has the potential for large scale production via roll-to-roll lamination processes[87].

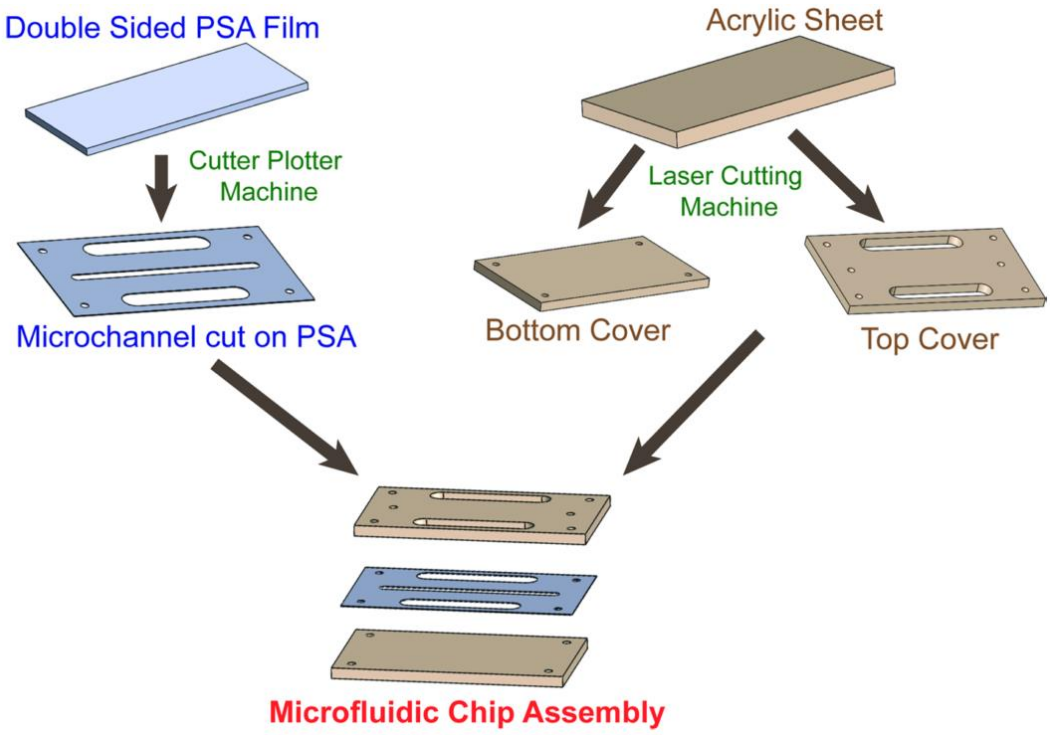

Figure 2.6. Microfluidic chip fabrication via xurography[84].

Ultra-fast pico- and femto-second lasers have been applied to write microfluidic channels and optical waveguides directly in ceramic and polymeric materials for a range of biological and chemical applications[88–91] with advances in this area outlined in a number of reviews[92,93]. To achieve smooth-walled channels necessary for microfluidic applications using this subtractive method, the material is first laser-processed to form the microchannels and then subjected to thermal treatments and chemical wet etching; hydrofluoric acid or piranha solution can be used for this purpose[92,93]. An example of the subtractive multi-step direct write procedure is shown in Figure 2.7.

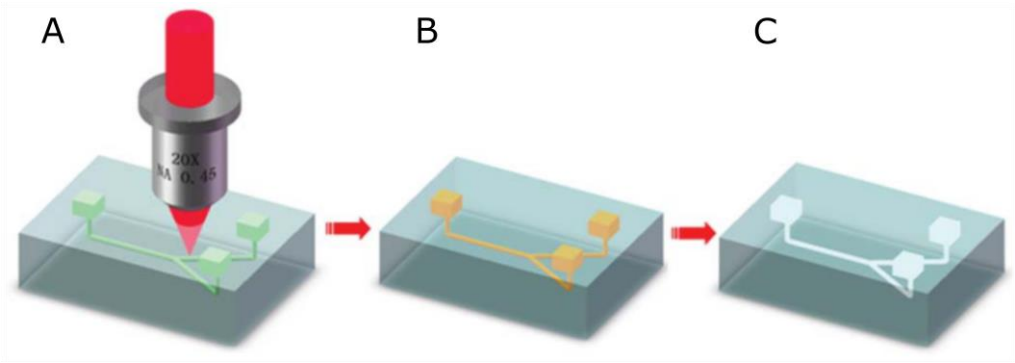

Figure 2.7. Direct-write fabrication of 3D microstructures inside photosensitive glass via femtosecond laser ablation, adapted from [93]. (A) Femtosecond laser direct writing; (B) heat treatment, 505°C 1hr - 605°C 1hr; (C) ultrasonic etching in 10% hydrofluoric acid solution.

Low-cost nanosecond lasers have also been used to fabricate microfluidic channels in bulk material in a single step[62,81]. The process involves focusing an Nd:YAG laser beneath the surface and machining channels inside the bulk material using a galvanometer scanning across the horizontal plane in a subtractive-type procedure. Although this process is repeatable, the shape of the internal channel produced is difficult to control[62].

Internal channels can also be built using a method known as laser drilling that involves moving the laser focal point into the sample material; this yields a uniform circular channel cross section but channel lengths are limited by how far the laser can penetrate into the sample[62]. Furthermore, the laser drilling process is limited to production of straight channels in a single orientation and is thus incapable of producing complex internal structures.

A European project “Femtoprint” offers an all-in-one solution for 3D printing glass microdevices comprised of a femtosecond laser head and integrated optics, with sub-micron resolution[94]. This system has been used to combine several applications including optofluidics, optomechanics, marking, and photonics. Although the technique can produce 3D microstructures and channels with aspect ratios comparable to DRIE in glass and other materials, the production of internal microchannels remains a challenge and a channel sealing step is usually employed. Fabrication of integrated optical components (including waveguides, microlenses, and nanogratings) in-situ is one of the greatest advantages of this system.

2.3 3D printed microfluidic devices

Additive manufacturing (AM), commonly known as 3D printing, has brought about a sea-change in modern manufacturing, enabling the creation of components with complex 3D geometries. The design freedom offered by these new technologies has already revolutionised industries such as biomedical[95,96], aerospace[97], and automotive[98], enabling more efficient designs with a higher strength to weight ratio than previously possible. In this section, current 3D printing technologies are discussed with an emphasis on the production of microfluidic channels in polymeric materials.

2.3.1 Fused Filament Fabrication (FFF)

Fused Filament Fabrication (FFF), also termed Fused Deposition Modelling (FDM®), is the method which brought 3D printing to the consumer market and, as a result, has become the most popular 3D printing method in the last decade. It is based on the extrusion of melted bulk material through a heated nozzle[99] (Figure 2.8). As with other 3D printing technologies, each 2D layer is traced out with subsequent layers being added to build up the required 3D design. Common materials used in the FFF process include acrylonitrile butadiene styrene (ABS), polylactic acid (PLA), and nylon. FFF printers can write in multiple thermopolymer materials without the need to change filament by employing multiple extrusion nozzles. Due to the nature of the printing process, the resolution achievable is limited by the xy-plotter (two stepper motors), the z-stepper motor, the thickness of the filament, and the extrusion nozzle diameter. FFF printers are widely available from market leaders such as RepRap, Ultimaker, MakerBot, 3D Systems and Stratasys, but can also be purchased from small companies or made in-house at low cost.

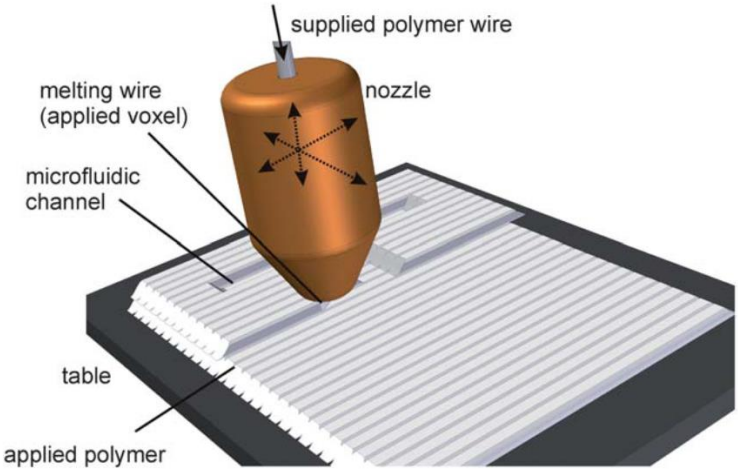

Figure 2.8. The fused filament fabrication (FFF) 3D printing process[6].

Although capable of printing cavernous structures within the bulk polymer a major challenge lies in producing fluidically sealed channels and producing channels with complex cross sections. FFF 3D printers in general do not give sufficient resolution or surface roughness to produce microfluidic channels, the size of the extrusion nozzle being the main limiting factor. However, one significant advantage of FFF over other 3D printing processes is the ability to produce fluidic channels and other enclosed structures without leaving support material or uncured liquid resin behind. Another advantage in using FFF is material selection; with a wide range of thermoplastic polymers (COC, ABS, PP) available for use in the thermal extrusion process.

2.3.1.1 Microfluidic applications

Fabrication of internal microchannel networks via FFF is challenging as resolution is largely confined to the millimetre scale, limiting channel size and cross-sectional geometries. In addition, the channel enclosing step is extremely difficult without the use of support structures to support the overhanging channel ceiling. This often results in poorly sealed channel structures which are prone to leakage.

Despite these weaknesses a number of researchers have created milli-fluidic devices using this method. The Cronin Group at the University of Glasgow report on the use of FDM as a method to produce 3D printed millifluidic and microfluidic devices and reaction-ware for chemical and biological applications[100–105]. Morgan et al.[106] printed fluidically sealed semi-transparent microfluidic devices using an off-the-shelf FFF 3D printer with commercially available materials. Devices fabricated using this method

were used for the encapsulation of dental pulp stem cells in alginate droplets. In order to demonstrate the efficacy of FFF in producing microchannels Gaal et al.[107] successfully employed the technique in the fabrication of a microfluidic device with an integrated electronic tongue sensor.

A microfluidic chip integrating ports for a three-electrode system was produced in PLA via FFF, and used for specific electrochemical detection of influenza virus[108]. Influenza hemagglutinin labelled with CdS quantum dots was first isolated within the reaction chamber by glycan-modified paramagnetic beads via hemagglutinin-glycan interaction. Electrochemical quantification of cadmium(II) ions by differential pulse voltammetry was then carried out to determine the presence of the virus.

FFF has also been investigated for fabrication of capillary valves in centrifugal microfluidic discs[109]. Results showed that 3D printing can be considered a viable alternative to other fabrication techniques typically employed for the fabrication of microfluidic discs (e.g. CNC milling and soft lithography) in view of their application in the development of biochemical assays[85]. Although channels produced in ABS possessed ridged or ‘‘scalloped’’ patterns, structures containing predictably-operable valves were obtained. Valve structures comprising channels with widths of 254 and 508 μm, and heights between 254 and 1016 μm were successfully fabricated.

The first commercial FFF 3D printer designed specifically for the fabrication of microfluidic devices has been developed by Dolomite microfluidics. The Fluidic Factory™ printer offers a resolution of 320 μm (*x* and *y*) and 125 μm (*z*) with a 400 μm or 200 μm nozzle diameter. This translates to a minimum channel cross-section of around 200 x 320 μm. The ability to print fluidically sealed channels in biocompatible COC is a major step forward for the FFF process however higher resolution is required to compete in the field of microfluidics. Other laser-based optical lithographic printing methods including two-photon-polymerisation (TPP), Stereolithography (SL), Ink-jetting of photopolymers (using MJM or MJP) and Selective Laser Sintering (SLS) fare better at the micro-scale.

2.3.2 Ink-jet 3D printing (i3DP)

Ink-jetting of photopolymers using techniques such as PolyJet 3D printing (Stratasys) or Multi-jet printing (MJP, 3D Systems) is a popular commercial technique that enables rapid production of parts in a wide range of materials and in multiple colours.

The technique involves jetting droplets of UV curable resin and a wax or gel-like support structure and instantly curing under UV light (Figure 2.9).

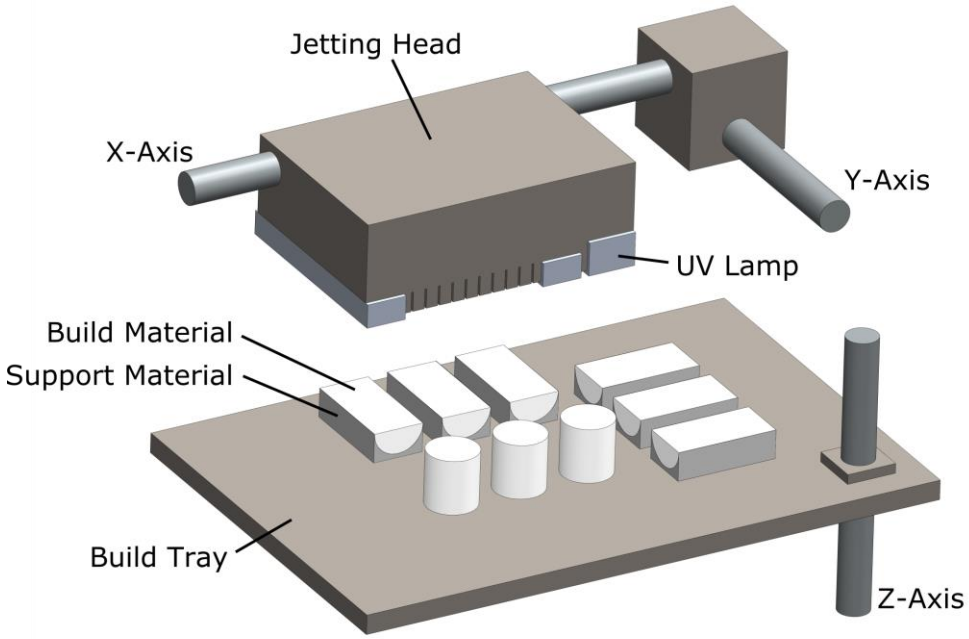

Figure 2.9. The PolyJet 3D printing technique (Stratasys Objet), adapted from [2].

The support structure is deposited in areas that contain hollow sections or overhangs and does not crosslink with the main polymer material. Support material is removed after printing by heating (in the case of the wax material), by using a high-pressure water jet (in the case of the gel-like material), or by sonication in a solution of sodium hydroxide. Internal microfluidic geometries become difficult or impossible to clear as the sodium hydroxide solution often does not fully penetrate the complex network. In difficult cases high pressure hot water and solvents may be used, however this is a highly involved and time consuming process[110]. Resolution of the MJP process depends on the DPI, or dots-per-inch, of the printhead. Modern printers like the Objet Connex™ or the 3D systems Projet™ 3500 can achieve a layer resolution of 16 μm with a DPI of 600-750 in the horizontal plane.

2.3.2.1 Microfluidic applications

Integration of commercially available PC membrane inserts into a reusable microfluidic chip containing eight parallel channels has been demonstrated (Figure 2.10)[111]. The chip, also integrated with standard threaded connectors, was manufactured with a 3D printer by inkjet deposition of a biocompatible photocurable resin within approximately four hours. This chip was successfully employed in studying the transport of drugs (levofloxacin and linezolid) across a polycarbonate membrane in view of its future applications in pharmacokinetic profiling of cultured cells. Cell viability studies were also performed with this platform via exposure of bovine pulmonary artery endothelial cells to a detergent (saponin) which was pumped into the channels inducing cell death.

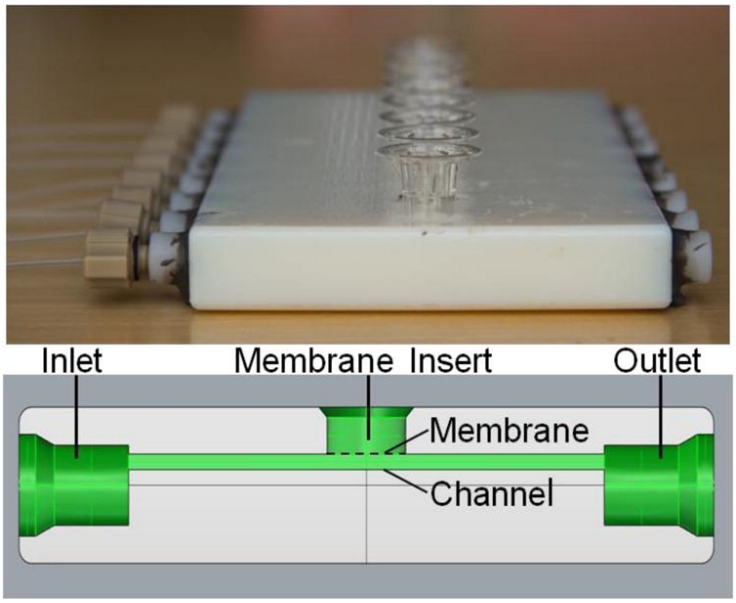

Figure 2.10. Microfluidic chip integrating membrane inserts[111].

Inkjet-based 3D printing technology has also been used for the fabrication of transparent microfluidic devices integrating interchangeable electrodes of different materials (glassy carbon, platinum, gold, and silver) and sizes (from 250 μm to 2 mm diameter) for electrochemical detection[112]. The resulting two-electrode microfluidic cells presented a straight channel and threaded receiving ports for integration of the electrodes as well as the standard connectors to the syringe pump (see Figure 2.11). The removable working and pseudo-reference electrodes were prepared by insertion

into PEEK fitting nuts in a serial configuration. This approach prevented the need for careful alignment of the electrodes with the microchannel each time the electrodes were interchanged. These microfluidic devices were successfully employed in the detection of dopamine (neurotransmitter) and nitric oxide, as well as the collection of adenosine triphosphate (ATP) released from red blood cells flowing through the channels while simultaneously measuring oxygen concentration (release stimulus). For collection of ATP, polyester membrane inserts were fitted into a couple of well ports integrated in the device. Collected ATP was then analysed by chemiluminescence detection.

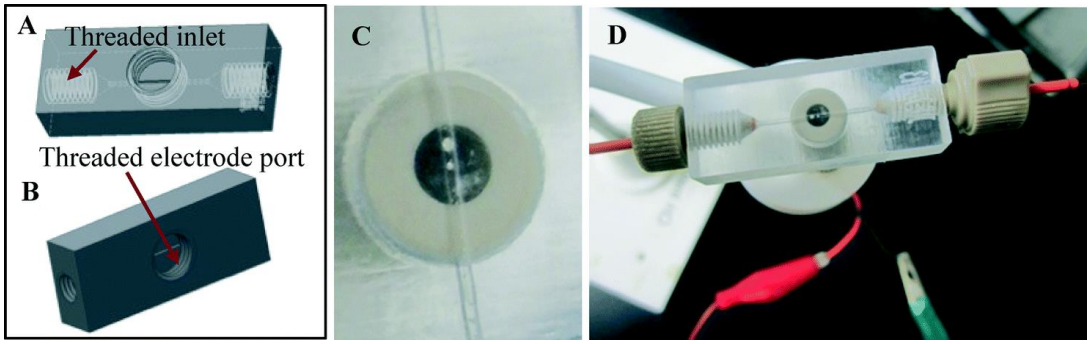

Figure 2.11. Microfluidic chip for electrochemical detection: A-B) schematic of the chip showing threaded ports; C) picture showing alignment of both working and pseudo-reference electrodes within the channel; D) picture showing the chip connected to the syringe pump[112].

Fee et al.[110] produced both packed and monolithic separation columns using a photopolymer ink jetting process despite difficulties associated with support material removal using this technique. Support material was removed using a vigorous and highly involved technique cycling between warm water (70°C) and 100% cyclohexane washes for up to three hours. The highly structured porosities showed good agreement with theoretical calculations for packed and monolithic structures.

2.3.3 Powder bed technologies

Powder bed AM technologies are defined by the use of working material in powder form. Polymer, metal, and ceramic materials can be produced in powder form and subsequently processed using a variety of techniques including selective laser sintering (SLS), selective laser melting (SLM), and binder ink-jetting.

SLS and SLM processes produce parts by selective sintering/melting of the working powder material. The process employed depends on the working material with SLS being used on a variety of materials including polymers, metals, metal alloys, and ceramics; SLM on the other hand can only be used to process metals. A schematic of the SLM process is shown in Figure 2.12. After production of a single layer via raster scanning of the laser beam over the surface of the material, the material tray moves down vertically, and a roller is used to replenish the powder material; this process is repeated until a 3D structure is complete. The SLS process is functionally similar to SLM, however the difference lies in the treatment of the working material. In SLS the material is processed at temperatures below the melting point forming a solid via molecular fusion and resulting in a porous granular material. On the other hand, the SLM process fully melts the material forming a melt pool where the material can consolidate before hardening, resulting in a homogeneous final material.

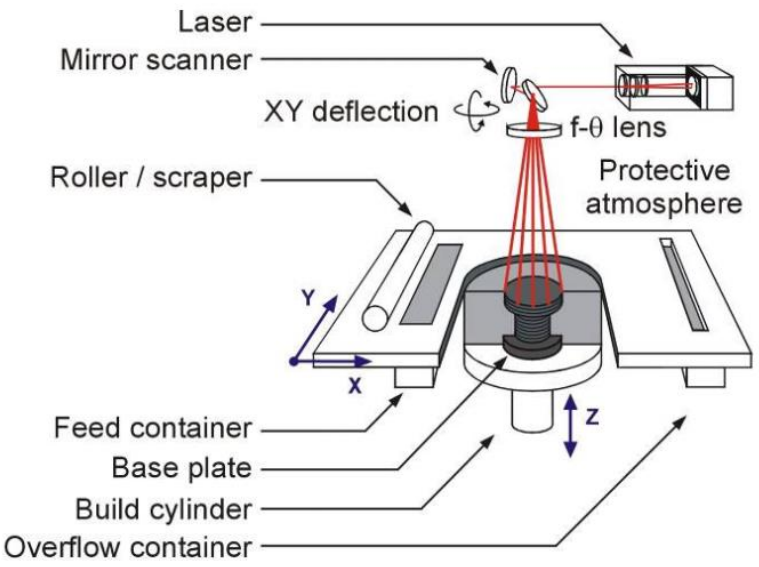

Figure 2.12. Schematic of the SLM process[113].

Inhomogeneity of the final part due to variation in the laser scan path is an issue with the SLS technique. Mechanical properties of the produced part have been shown to vary based on part orientation on the build plane[114]. In addition, the powder working material cannot be removed from complex internal structures. As a result, production of microfluidic channels is limited to the surface of the material substrate.

The binder ink-jetting 3D printing technique enables production of parts in a variety of materials including polymeric and ceramic materials. The binder jetting technology involves the deposition of a binder material, or glue, at defined locations to the working material which is in powder form[6]. When the first layer is complete, a fresh layer of powder material is spread over the build area adhering to the previously deposited binder material. This process is repeated until a 3D part is complete.

2.3.3.1 Microfluidic applications

Metal AM techniques, such as SLM, have been used to fabricate fluidic filters demonstrating the ability to fabricate complex open pore structures[115]. The ability to fabricate these pores together with an integrated support and fixture in a single step could reduce total fabrication time, particularly for bespoke applications. In addition, capabilities of AM methods in producing lattice networks with multiple variations in a single part can lead to a reduction in pressure drop across the filter and a corresponding reduction in the pumping energy required[115,116].

Capel et al.[117] showed the capability of SLM to produce a simple reactor design in Titanium (RD7) incorporating 3 mm diameter flow channels and a reactor tube length of 300 mm. Despite the large size of the flow channels the unmelted powder material proved difficult to remove.

2.3.4 Vat photopolymerisation (VP)

Photopolymerisation processes make use of liquid, radiation-curable photopolymer materials, also called resins, as their primary materials[118]. Most photopolymers react to radiation mainly in the ultraviolet (UV) domain, however many operate at the interface and into the visible domain. Irradiation of the liquid photopolymer working material triggers a chemical reaction causing the material to polymerise. This solidification reaction is termed photopolymerisation, and is a complex chemical reaction involving many reactive chemical participants.

The photopolymerisation reaction is the basis for Stereolithography (SL) which first appeared in the early 1970s when Japanese researcher Dr. Hideo Kodama used UV light to cure photosensitive polymers in a layer-by-layer manner. However, the term Stereolithography didn’t appear until the 1980s when Charles Hull discovered that solid polymer patterns could be produced by exposing them to a scanning laser[119].

Three-dimensional parts could be fabricated in this manner by curing the polymer in a sequential layer-by-layer fashion. Shortly after, the company '3D Systems' was founded by Hull and his SL technology was pitched to the product development industry as a "rapid prototyping" solution.

Since then, the photopolymerisation concept has evolved and is now applied as a rapid prototyping technique in many different configurations that can be classified under the term 'vat photopolymerisation' (VP). In terms of microfluidic device prototyping, VP methods present an inherent advantage over other lithographic methods (i.e. photolithography and soft lithography) in that no alignment or bonding is necessary to produce 3D structures. These methods have only recently (c. 2010) been applied to the rapid production of milli- and micro-scale channels but already show promise in significantly reducing the development times of new microfluidic assays[6–9,120].

Of the currently available VP techniques, mask projection micro-stereolithography (MPμSL) is among the most popular with microfluidic researchers offering the ability to fabricate complex microfluidic architectures at faster throughput than other VP methods. Major advances in LED technology and expiration of key industry patents in recent years has led to a cost reduction and wider adoption of this technique across industry. It is now possible to purchase a desktop MPμSL prototyping machine for less than $2,000[1]. As a result, these techniques have become increasingly popular for microfluidic device prototyping offering faster concept-to-design throughput than any other technique available[1,9,121,122]. Consequently, this technique is given special consideration in the current work.

2.3.4.1 VP configurations

There are three main VP system configurations as shown in Figure 2.13. These include; (1) the vector scanning, or point-wise, SL method developed by Hull (Figure 2.13 (A)); (2) the mask projection, or layer-wise, approach common in modern desktop machines (Figure 2.13 (B)); and (3) the two-photon high resolution approach that is predominantly used in research (Figure 2.13 (C)).

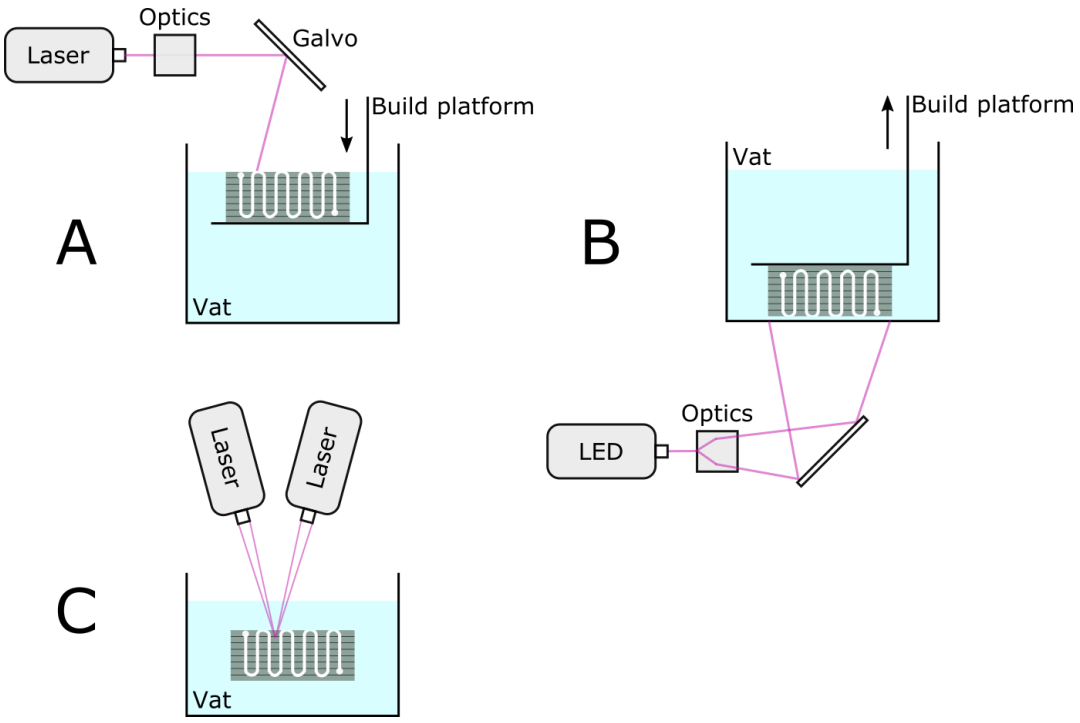

Figure 2.13. Schematic outline of the three main approaches to vat photopolymerisation, adapted from[118]. (A) The laser vector scanning (free surface) method developed by Hull[119], (B) the mask projection (constrained surface) method common in modern desktop 3D printers and (C) the two-photon approach.

Additionally, these VP configurations can be categorised as either ‘free surface’, or ‘constrained surface’ depending on the location of the optics unit in relation to the resin vat and build platform. In the free surface configuration, the optics are scanned or projected from above the resin bath on to the surface of the resin to create a single layer, after which the build platform is lowered into the photopolymer vat as in Figure 2.13 (A). In comparison, Figure 2.13 (B) can be classed as a constrained surface method as polymerisation is constrained between the vat window and the build platform or part. The two-photon polymerisation (TPP) configuration in Figure 2.13 (C) can also be thought of as a free surface method where polymerisation is unconstrained and occurs at the intersection of two scanning laser beams. Other two-photon configurations use a single scanning laser and different photoinitiator chemistries, but these configurations are also unconstrained. Of these configurations, the bottom-up constrained surface configuration is more efficient as the part height is not restricted by the size of the vat, there is less resin waste, and the layer thickness

can be more readily controlled by the z-stage positioning as opposed to controlling the laser depth of focus[1].

MPμSL, sometimes referred to as digital light processing (DLP), is a VP technique based on the bottom up configuration (Figure 2.13 (B)) employing a UV-LED light source instead of laser optics, and a digital micromirror device (DMD) as a dynamic mask. The operation of a DMD is outlined in Figure 2.14.

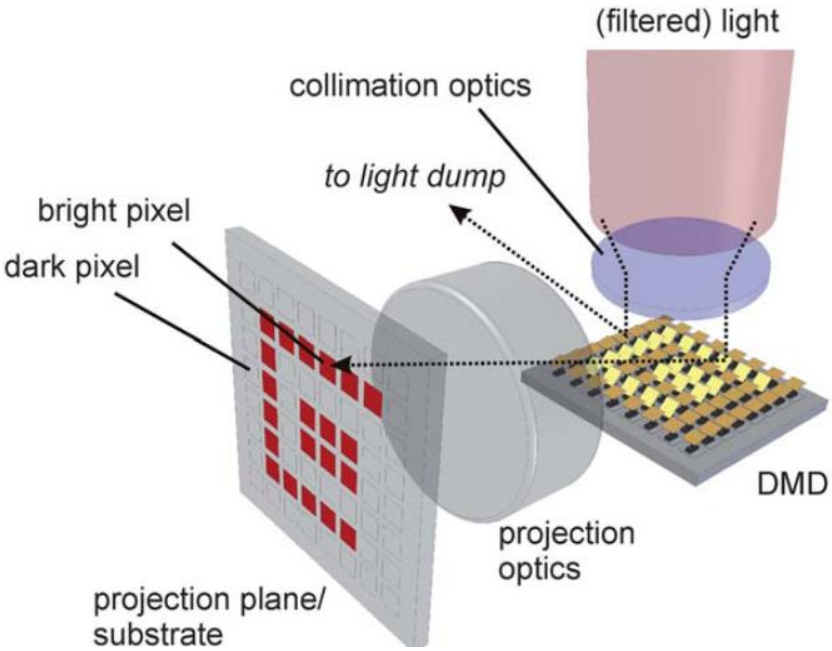

Figure 2.14. Representation of a digital micromirror device (DMD) as used in many modern desktop mask-projection stereolithography systems[6]. The incoming light source is filtered and collimated before being reflected (or masked) in a pattern by the DMD. Depending on the reflect/mask (on/off) state of the individual DMD pixels, the light is either deflected to a light dump or through the projection optics and onto the substrate surface.

DMDs, commonly used in audio-visual projection optics, process light using thousands of individually-addressable micromirrors. These individual micromirrors are so small that an image resolution of 7.6 μm or less is feasible[123]. When in the "on" state, these micromirrors reflect the incoming light from the light source through the projection optics and into the resin bath; in the "off" state the light is reflected to a light dump. This serves to effectively mask the incoming light in a programmable pattern; thus these systems are commonly referred to as dynamic mask projection

systems[6]. Compared to traditional laser-based raster scanning VP methods, MPμSL enables curing of an entire layer in a single step, offering faster throughput for device fabrication with build speeds up to 30 mm/hr in the Z direction. Many raster scanning VP methods offer similar build speeds for low-volume builds, although high-volume builds are comparatively slower. Unlike raster scanning VP methods, MPμSL build speed is independent of part cross-section in the *x-y* plane.

Another distinction that can be made between VP methods is the need to replenish the resin material between consecutive layers. Both vector scan and mask projection approaches require replenishment of the resin material usually by means of a wiper or slider mechanism, whereas in the two-photon approach the part is fabricated below the resin surface, making recoating unnecessary. In the case of the constrained surface methods the resin replenishment mechanism also serves as a method to mechanically unstick the polymerised material from the underside of the build tray. This need for an additional recoating and/or unsticking step is a significant drawback of the constrained surface configuration.

Tumbleston et al.[10,14] have developed a continuous VP method based on the MPμSL technique that does not require recoating or unsticking of the resin material between layers and is thus orders of magnitude faster than similar mask projection methods offering build speeds up to 500 mm/hr. This new configuration can be categorised as a constrained surface method employing an oxygen-permeable membrane to inhibit polymerisation and creating a "dead zone" at the interface between the projection window and the polymerising part (Figure 2.15). This variation is named "Continuous Liquid Interface Production" (CLIP).

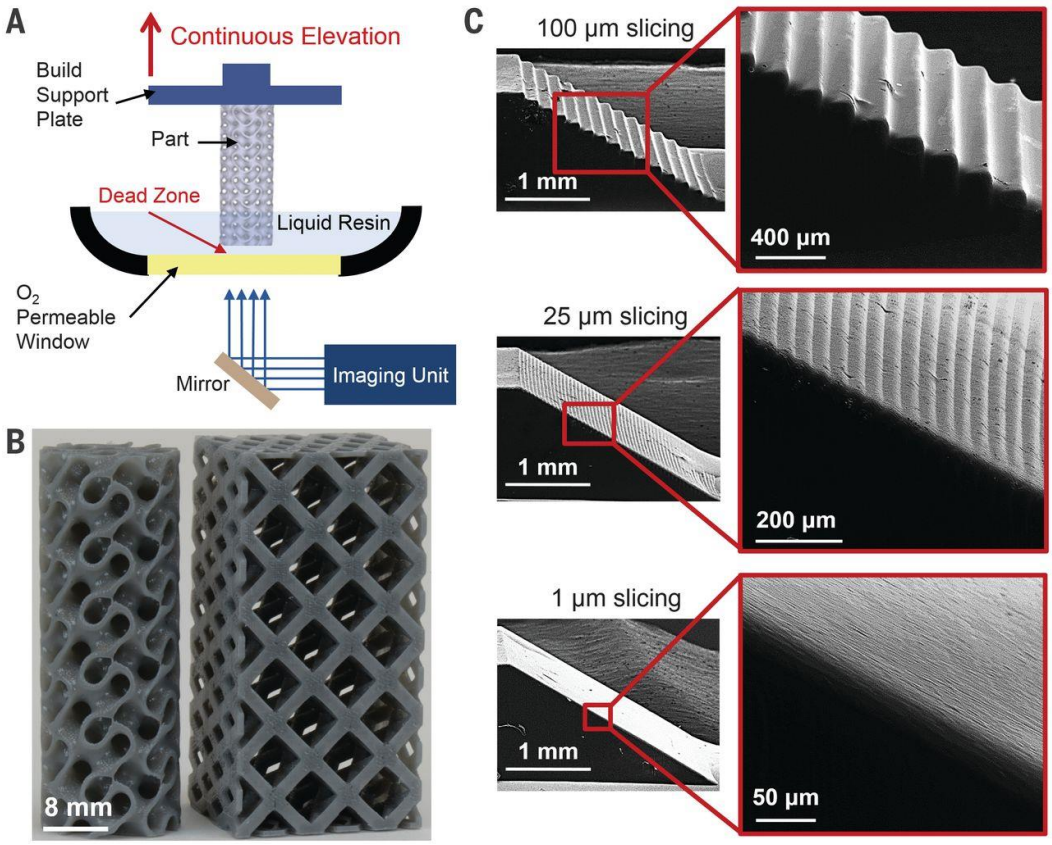

Figure 2.15. The CLIP vat photopolymerisation method enabling continuous fabrication of 3D objects. (A) Schematic of the CLIP printer, the part can be built continuously due to the oxygen-permeable window, (B) a gyroid (left) and an argyle (right) build at speeds of 500 mm/hour, and (C) ramp test patterns built at the same speed but with different model slicing thicknesses (100 µm, 25 µm, and 1 µm).

TPP is based on the polymerisation of a photocurable resin via two-photon absorption upon illumination with a femtosecond pulsed near-infrared laser[124]. Compared to other VP methods, the TPP process is not hindered by the diffraction limit of the light source leading to much better structural resolution[125]. Thus, resolution in the order of 100 nm is feasible for TPP instruments (e.g. Nanoscribe GmbH systems). Build speed and part size are the limiting factors with this technique, with milli-scale parts typically taking hours to build. It is for this reason that TPP is mainly used to produce micro- and nano-scale actuators[124], mixers[126], filters[127], valves[127] and other single-function elements[124] inside larger scale microfluidic channels built using other techniques.

2.3.4.2 Microfluidic applications

MPμSL, has gained popularity among a number of microfluidics research groups offering a fresh alternative to 2D lamination and mask-based etching processes[7–9,121,122,128,129]. Au et al.[7] were the first to conduct a comprehensive review of the SL process for producing internal micro cavities and channels for applications in microfluidics. They cite the ability to produce 3D internal cavities and structures, low cost, and user-friendly design and fabrication workflow as being key benefits of the MPμSL process, giving scientists direct access to scalable rapid prototyping facilities.

Shallan et al.[8] showed that it was possible to produce a 40 mm × 25 mm × 17 mm micromixer chip (including connectors) in less than an hour using a rather cheap MPμSL 3D printer (approx. $2,300) and incurring a material expenditure of only $2 (Figure 2.16).

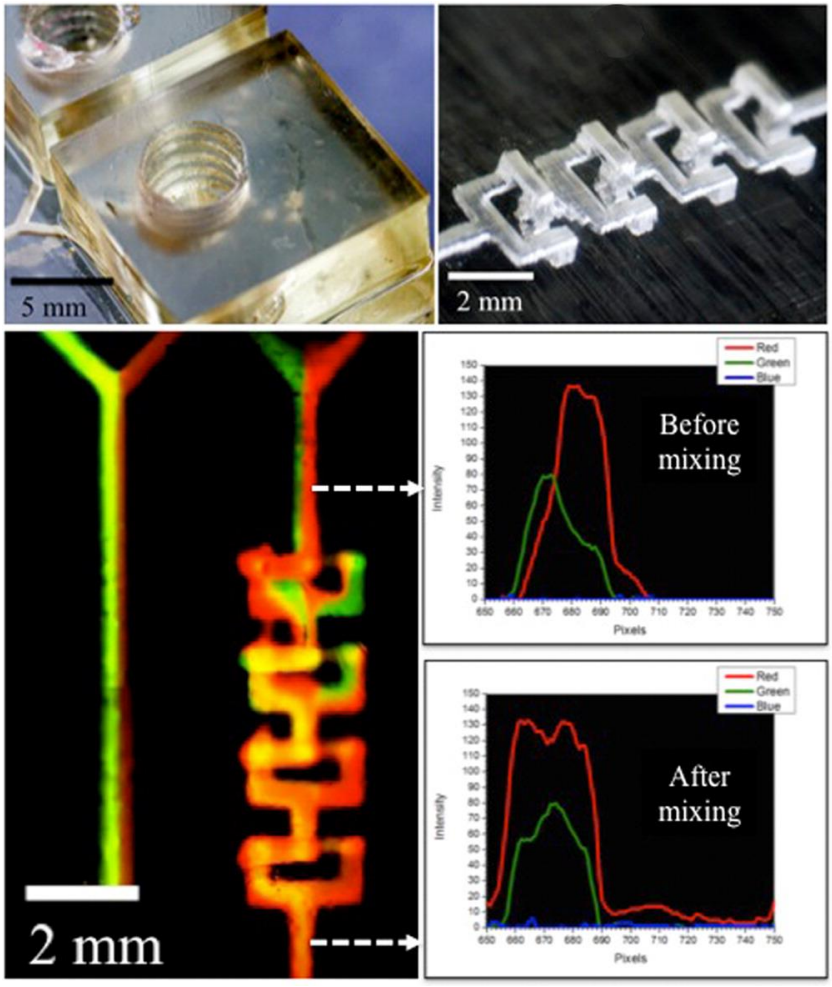

Figure 2.16. Optically transparent microfluidic mixer chip integrating 10-32 threads[8].

They found the process capable of producing micro scale features and voids and characterised the system limitations (Figure 2.17). Gradient generators, droplet extractors and isotachophoresis chips were also successfully generated with the same 3D printer confirming the feasibility of this approach for cost-effective, rapid prototyping of microfluidic devices, which could open the door to many future low-cost analytical applications. However, they cite overcuring or the so-called 'back-side effect' as being one of the main limitations of the MPμSL process.

Fabrication of optically transparent microfluidic devices using SL was achieved by Takenaga et al.[130]. These optically transparent chips were successfully employed in imaging Chinese hamster ovary (CHO) cells previously seeded within the microchannels. Albeit a certain degree of autofluorescence was exhibited by the biocompatible resin employed in the chip fabrication, discrete cells were clearly observed under fluorescence as well as phase-contrast modes. The capability of SL for direct integration of standard connectors to the macro-world within the final device was also demonstrated (e.g. female Luer connectors[7] and 10-32 threads[8]).

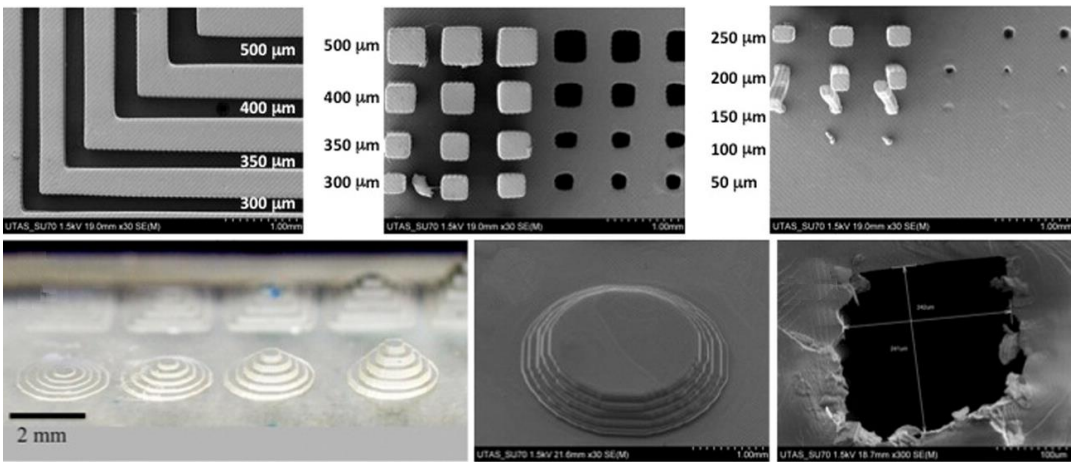

Figure 2.17. Characterisation of the MiiCraft DLP 3D printer by Shallan et al.[8]. The 3D printer is capable of producing repeatable external features of 200 μm, internal microfluidic channels below 250 μm are difficult to produce due to overcuring of the polymer resin.

Design and fabrication of porous media in a single step using MPμSL was recently achieved by a Su et al.[131]. Su, using the same MPμSL printer used by Shallan et al.[8], produced a pre-concentrator for the selective extraction of trace metal ions in salt water

samples. The MPμSL method allowed them to fabricate a porous cubic array in a single step with pore sizes of ~50 um.

2.3.5 Summary

Current 3D printing methods are largely concerned with fabrication of parts with external features and thus were not built to produce internal voids and features such as microfluidic channels. Despite this, interest from within the microfluidic community has spurred an uptake in common 3D printing methods toward the creation of internal voids and microfluidic channels. Some of the methods investigated include FFF, i3DP, and VP methods.

FFF has been used to create leak-tight fluidic channels for a number of applications, however resolution of the technique is limited by the extrusion nozzle size (~200 μm). i3DP has the capability to produce microfluidic channels at higher resolution, however the technique is expensive and removal of the support material from complex internal microfluidic channels is extremely difficult.

Despite the ability to produce complex mesh networks[115], powder bed technologies such as SLS, SLM and binder deposition methods share a similar problem in the removal of unmelted material from channel networks. As a result, production of microfluidic channels is largely limited to the substrate surface[132].

Of all the current AM techniques, MPμSL is uniquely suited to the production of microfluidic channels in a single step for several reasons. First, the working material is liquid which can easily be removed from internal channel structures. Second, there is no need for the use of support structures when fabricating micro-scale internal features. Third, the equipment is cost effective offering a high resolution-to-cost ratio[1,8]. Finally, feature size limits range from as low as 10 μm to ~75 mm in the same build, ideal for microfluidic applications where connections from macro- to micro-scale are needed.

2.4 Photopolymerisation process modelling

As the uptake in AM processes grows across the industry, there is a greater need for predictive modelling to characterise limitations and advantages of each technique. Modelling of AM processes has recently gathered speed as these techniques are applied to critical applications in biomedical, aerospace, and automotive sectors. Advances in the computational power of modern personal computers and wider access to cloud computing resources has brought the ability to model and simulate to the consumer. In this section, the photopolymerisation process is discussed in relation to process modelling.

2.4.1 Photopolymer materials

First developed in the 1960's, photopolymer materials are now widely used across industry for applications in coating and printing, dentistry, audiology, and the fabrication of microelectronic devices using photolithography[118].

Photopolymer materials react to radiation in a broad number of spectral categories including gamma rays, X-rays, electron beams, UV, and visible light, however UV and electron beam are most commonly used. Recent developments in UV-LED technology have led to an increase in availability of UV SL systems. It is now possible to purchase a desktop MPμSL 3D printer for less than $2,000[1] with both UV (385 nm) and visible (405 nm) options.

Polymers can be categorised into linear, branched, and cross-linked structures, as shown in Figure 2.18. Thermoplastic polymers exhibit a linear or branched molecular structure and can be repeatedly melted and re-solidified. These polymer materials are processed using thermoplastic extrusion or embossing methods including injection moulding, FFF, and hot embossing, or by melting in a defined pattern as in SLS.

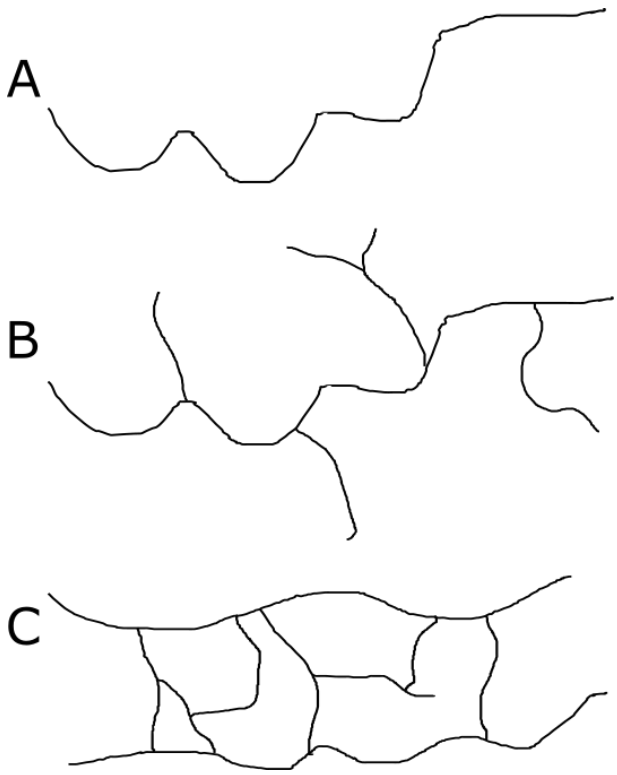

Figure 2.18. Polymer types; (A) linear, (B) branched, and (C) cross-linked, adapted from[118].

On the other hand, VP photopolymers are cross-linked and, as a result, do not melt. In addition, these photopolymer materials exhibit much less creep and stress relaxation.

Photopolymer materials are comprised of three main components; monomers and oligomers, the photoinitiator, and additives. Monomers and oligomers act as the main component in the mixture and are responsible for the mechanical properties of the solidified part. The photoinitiator is the basis for the polymerisation reaction initiating crosslinking upon exposure to light at a specific wavelength (usually 325, 355, 365, 385, or 405 nm)[13]. Functional additives including reactive diluents, light absorbers, and pigments play an important part during the VP build process tuning the photopolymer resin viscosity and light absorption to increase build resolution. Other additives enhance the visual or mechanical properties of the final part. The main functions of each component are outlined in Table 2.2.

Table 2.2. Composition of photopolymer resins, adapted from[133].

Component	Role
Monomers and Oligomers	The main components, carbon chains that will bond together to make a solid part. Final material properties depend mainly on these components.
Photoinitiator	Molecules that react when exposed to UV light producing radicals and initiating the polymerisation reaction.
Additives	Visual and functional supplements, including pigments, dyes, absorbers, and reactive diluents.

The liquid photopolymer material, also called photopolymer resin, is a plastic composed of carbon chains of length ranging from one carbon molecule to a few thousand carbons, it is comprised of all the elements of the final plastic material. When the resin is exposed to radiation at the appropriate wavelength, the photoinitiator reacts producing radicals and initiating polymerisation causing the shorter carbon chains to join covalently; forming longer chains and creating a stiffer material. As polymerisation progresses the chains elongate and cross-link and the resin solidifies; the entire process occurs in a matter of milliseconds. Figure 2.19 outlines the main steps in photopolymerisation comprising radical formation, radical propagation, and radical termination.

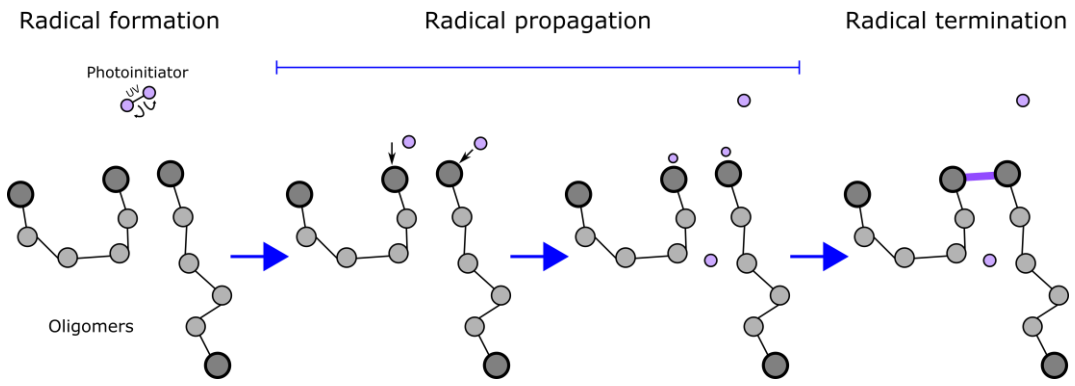

Figure 2.19. Free-radical photopolymerisation, adapted from[133].

Formulation of custom resin mixtures is straightforward and, as a result, many photopolymer blends exist. Variations consist of different backbones and side groups with a wide range of optical, mechanical, and thermal properties.

In the VP 3D printing process, the polymerisation reaction is not fully driven to completion and individual layers are kept in a semi-reacted "green state" with polymerizable groups on the surface. This is necessary for success of the layer-on-layer process as it provides sites for polymerisation and enables covalent bonding with subsequent layers (see Figure 2.20).

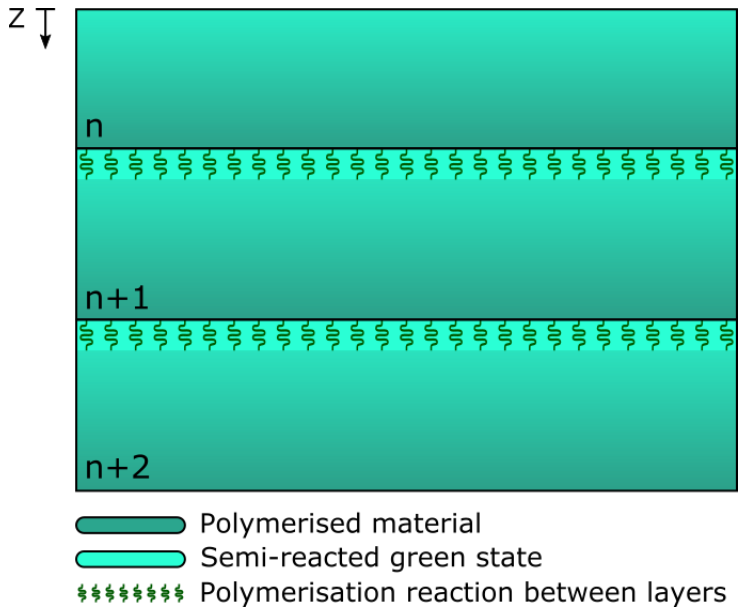

Figure 2.20. The semi-reacted green state of the layer interface enables layers to covalently bond together, adapted from[133]. Image shows build direction (*z*), and layer number (*n*).

This produces an isotropic part with little difference in the number of chemical bonds between lateral and vertical directions, resulting in mechanically sound, fluidically sealed, and optically clear parts with less risk of delamination.

2.4.2 Photopolymer curing kinetics

Photopolymer curing kinetics are governed by the Beer-Lambert law[134] which states that the absorbance of a material sample is directly proportional to its thickness and the concentration of the attenuating species in it. Absorbance and consequent attenuation of the incident light by the photopolymer material is essential for free

radical polymerisation. In modelling this effect, the first parameter of interest in this model is irradiance, I, which is the radiant power of the light source per unit area in W.cm^{-2}. Taking I_0 to be the irradiance at the interface between the polymer and the light source, the irradiance at any depth $z \geq I(z)$ is related to the irradiance at the surface by the Beer-Lambert law where the characteristic penetration depth, D_p, is the depth of penetration of the light source into a resin until a reduction in irradiance of $1/e$ is reached (this is a key resin characteristic with units of μm). The general form of the irradiance equation is given by equation (2.1)

$$I(z) = I_0 e^{-z/D_p} \tag{2.1}$$

The total energy received at depth z, $E(z)$ (J/mm^2), for an exposure time, t (s), is given by

$$E(z) = tI_0 e^{-z/D_p} \tag{2.2}$$

Where tI_0 is the energy received at the surface, $tI_0 = E_{max}$. Equation (2.2) can be re-written as

$$E(z) = E_{max} e^{-z/D_p} \tag{2.3}$$

Taking the natural logarithm of both sides and rearranging we get the equation for cure depth

$$z = D_p \ln\left(\frac{E_{max}}{E(z)}\right) \tag{2.4}$$

If we define E_c as the critical exposure (i.e. the exposure at which resin solidification starts to occur) equation (2.4) yields the working curve equation[134]

$$C_d = D_p \ln\left(\frac{E_{max}}{E_c}\right) \tag{2.5}$$

where C_d is the resin cure depth and the parameters D_p and E_c are photopolymer material characteristics.

A working curve for any photopolymer/light source combination can be generated by exposing the photopolymer material at a known exposure energy (mJ/cm^2) and

measuring the resulting polymer film thickness (μm). By fitting the resulting curve to equation (2.5) the photopolymer material characteristics, C_d and E_c, can be calculated. An example photopolymer working curve is shown in Figure 2.21.

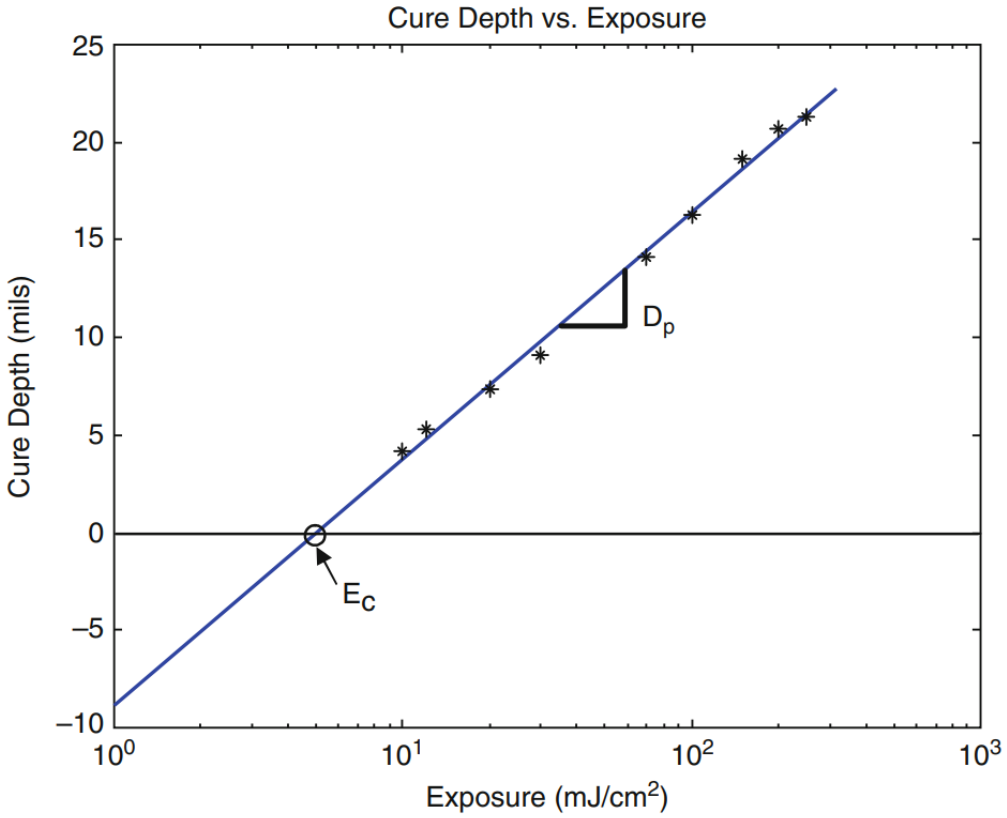

Figure 2.21. Photopolymer resin working curve of cure depth vs. exposure energy. Image from Gibson et al.[118].

2.4.3 Overcure

The main challenge in printing microfluidic channels via VP methods is accurate control of cure depth in the *z*-direction. This has previously been dubbed the "back side effect" by Breadmore et al.[8,135] as it occurs on the back side of the enclosing layer being formed. Overcuring of the resin material limits print resolution and represents the main obstruction to microfluidic channel formation. Figure 2.22 demonstrates the mechanism of overcuring in channels and overhangs oriented horizontally.

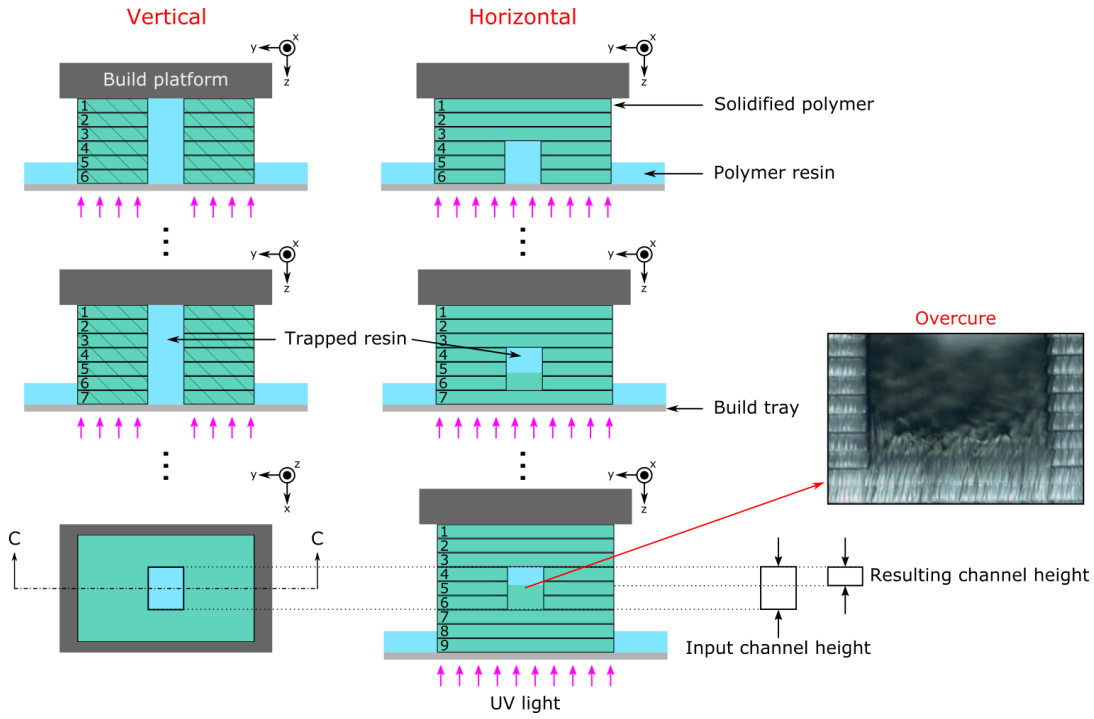

Figure 2.22. Layer-by-layer fabrication process for a microchannel oriented vertically and horizontally on the MPμSL build platform, adapted from[12]. The resulting microfluidic channel height is considerably smaller than the input channel height for the channel oriented horizontally on the build platform due to overcuring of the resin material inside the channel. Overcure does not occur in the channel oriented vertically.

Three approaches have been taken in the literature to address this problem. The first approach involves control of cure depth by doping the photopolymer resin with a light absorbing dye[12,13,123,136]. Using this approach, Zissi et al.[136] succeeded in reducing the polymerisation depth through the addition of a highly absorbing unreactive chemical, reducing polymerisation thickness by 8 to 10 times. Choi et al.[13] employed Tinuvin 327 as a light absorber in four concentrations to control cure depth of an acrylate-

based photopolymer resin. They achieved a cure depth of ~30 μm compared to ~200 μm without the use of a light absorber. Figure 2.23 shows a micro-fan fabricated using an acrylate-based resin with (B) and without (A) the light absorbing additive.

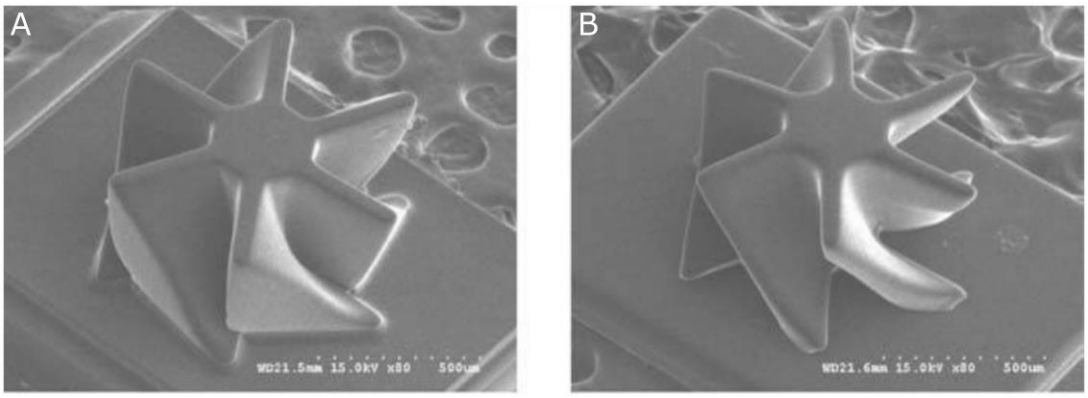

Figure 2.23. SEM images of micro-fans fabricated via MPμSL in an acrylate-based photopolymer material; (A) 0.0 and (B) 0.05 % ($^{w}/_{w}$) Tinuvin 327[13]. The effect of poor depth resolution in the *z*-plane can be seen in (A). This is overcome by doping the photopolymer resin with Tinuvin 327 in (B).

The level of overcuring for the resin material is evident in Figure 2.23 (A) causing the underside of the fan blades to adhere to the plinth. The effect is less pronounced in the doped photopolymer material in Figure 2.23 (B).

This approach was also applied by Gong et al.[12,123] who investigated light absorbers toward the production of a high-resolution resin for microfluidic applications. They investigate the minimum size of a microchannel produced via the MPμSL method for eight resin formulations[12]. They found the minimum channel height to be ~$3.5 - 5.5h_a$, where h_a is the characteristic penetration depth of the resin (also known as D_p, see equation (2.5)). They also describe the construction of a custom MPμSL 3D printer for the fabrication of microfluidic channels[123]. The new 3D printer and custom resin formulation was used to produce microfluidic channels with cross-section of 18 × 20 μm, made possible using a high resolution DLP light engine and a 385 nm UV LED light source. Compared to the 405 nm light source previously used, the 385 nm light source enables matching of the LED wavelength with a greater range of light absorbers. This improvement in equipment represents the second approach to solving the problem of overcuring.

The third approach, called the "Compensation Zone" approach was developed by Limaye and Rosen[137,138] to predict and mitigate for print-through errors caused by overcuring. Using this approach, the MPμSL process is modelled and problem areas where overcuring is present are identified. A defined volume of material (the compensation zone) is then subtracted from underneath the Computer Aided Design (CAD) model to compensate for the predicted increase in dimension that would occur due to overcure. This model could, in theory, eliminate print-through errors completely, resulting in part geometries that closely correspond to the input model geometry. However, this approach only applies to print through errors on the exterior of the designed part. As of yet, no effort has been made to mitigate for the overcuring effect in internal voids such as microfluidic channels.

2.5 Summary

Microfluidics as a field has been around since the 1980s. However, despite significant scientific advances, most microfluidic devices continue to be chip-in-a-lab rather than Lab-on-a-Chip, while the point-of-care diagnostic market remains just out of reach. One area that has held up research and development of such devices is the high-cost and complexity associated with the fabrication techniques which is a barrier to entry to the field for many research laboratories who do not have access to clean room facilities or expensive precision fabrication equipment.

Additive manufacturing techniques can provide a solution in this respect, offering the capability to fabricate custom fluidic devices at a fraction of the cost, time, and complexity of traditional techniques. However, AM fabrication methods have, to date, not been widely utilised within the field of microfluidics. This can be attributed to the poor resolution of cheap equipment, the prohibitively high cost of high resolution equipment, and the lack of availability of suitable materials. The expiration of key patents in recent years has brought many AM technologies to the consumer market, making them more affordable and encouraging competition between the newly formed companies supplying into this area. The rapid increase in the capabilities and availability of these AM technologies, at much reduced cost, has opened the door to the exploration of AM as an alternative to more conventional 2D microfabrication methods typically employed in the fabrication of microfluidic platforms. However,

most AM techniques are limited to creating millimetre scale exterior features: the creation of internal features and voids has proven difficult.

MPμSL stands out in this respect, with the capability of producing internal features and voids from a liquid photopolymer resin that can be removed after production. It is for this reason that this technique is most promising as a new prototyping technique for microfluidic chips. Recent studies have shown that 3D printing methods can effectively be used for producing micrometre scale internal channels within bulk biocompatible and transparent materials for a cost as low as $2 per chip[7], confirming the feasibility of this approach for rapid prototyping of cost-effective microfluidic devices in a single-step. Despite these advantages, MPμSL is still mainly limited to the millifluidic regime, with advances in photonic hardware and polymer technology slowly pushing the resolution limits to the micro-scale[12,123]

Continuous improvements in resolution are expected, even improving on the resolution of currently available TPP devices. However, it is clear that further research is needed in two main areas: removal of support material from complex internal geometries and solving the problem of overcure which represents a significant obstacle in the pursuit of high resolution 3D printed microfluidic channels.

Chapter 3

3D printed microfluidic chip for biological sample pre-treatment

Probe-functionalised Ion Exchange Membranes (IEMs) are a novel sensing method for the detection of nucleic acids in sample mixtures[139]. These label-free high-sensitivity biosensors are promising for on-site diagnostics due to their miniature form factor and potential for automation. However, one of the challenges in the development of an on-site diagnostic platform is the miniaturisation of lab-based cell lysis and pre-treatment protocols for efficient extraction of nucleic acids from the lysed solution prior to sensing. In addition, development of new microfluidic technology is time consuming and highly involved, requiring access to clean room facilities and expensive materials. In this chapter a novel pre-treatment protocol for cell-lysis, volume reduction and buffer exchange in a microfluidic form factor is designed and tested using a new cost-effective microfluidic rapid prototyping technique. A 3D printed microfluidic Solid Phase Extraction (SPE) column was developed and used to capture negatively charged RNA molecules through a chaotropic binding mechanism. The column was fabricated with integrated luer-lock fittings for connection to pumping and sensing peripherals in a single step using a UV curable photopolymer. SiO_2 particles were then packed against the integrated packing weir and the device was sealed using a standard luer-lock fitting and flushed with RNase Zap and RNase-free water to remove RNase enzymes. The SPE column was subsequently loaded with the lysed cell solution and the column was washed using a buffer optimised to reduce the conductivity of the eluted sample while retaining the nucleic acids on the column. Finally, RNA molecules were eluted using deionized (DI) water and volume fractions were analysed using quantitative reverse-transcription polymerase chain reaction (qRT-PCR) and compared with commercially available RNA purification methods.

This chapter demonstrates the strengths of using the MPμSL 3D printing technique for microfluidic assay design, development, and rapid prototyping.

3.1 Introduction

Silica-based SPE is a popular method in biological sample pre-treatment due to the binding affinity and specificity of nucleic acid molecules to the stationary phase. Many commercial spin-column based pretreatment solutions exploit this (e.g. Qiagen RNeasy), offering a wide range of DNA and RNA pretreatment kits. The extraction protocol consists of five main steps including; lysis, binding, washing, and elution facilitated by a silica gel stationary phase to which the nucleic acids bind under chaotropic buffer conditions (Figure 3.1).

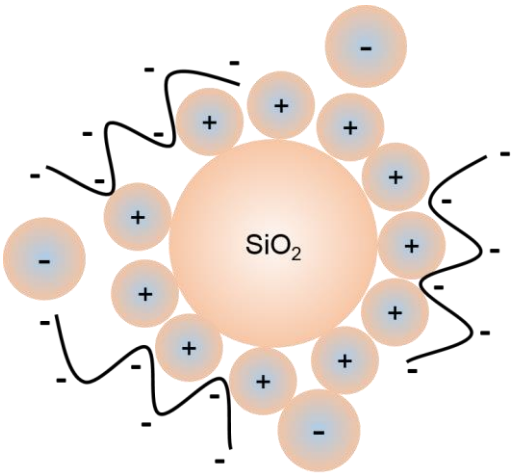

Figure 3.1. The chaotropic binding process. Negatively charged nucleic acid molecules bind to the negatively charged silica in the presence of positive ions (chaotropic salts).

This mechanism lends itself to microfluidic chip-based nucleic acid purification with applications in portable, field-based molecular diagnostics and prognostics when coupled with an oligo-probe based detection system. Development of a solid phase extraction protocol that is not reliant on laboratory equipment would be a considerable step toward a truly portable nucleic acid diagnostic device. However, a number of obstacles exist including integration of the solid phase, and removal of the lysis buffer while retaining nucleic acids on the stationary phase. Previously, Breadmore et al.[140] integrated a silica stationary phase into a microfluidic channel for purification of DNA. This was achieved by packing silica beads against a temporary silica sol-gel frit integrated in the channel. Another fabrication method is reported by Cady et al.[141]. They fabricated a meander-shaped microfluidic channel with integrated silica-coated pillars for SPE using a photolithography etching process. Zhang et al.[142] developed a

disposable cartridge incorporating an etched microfluidic pre-treatment chip with silica coated microchannel. This system was used in line with RT-PCR for dengue viral nucleic acid extraction and detection. In a similar study, a dual-domain SPE chip was developed by Reedy et al.[143]. They fabricated a microfluidic chip with silica and chitosan stationary phases in series for concentration of nucleic acid samples for down-stream applications. This dual domain approach uses the chaotrope-driven binding of the silica stationary phase together with an ion-exchange chitosan phase to remove PCR inhibitors such as guanidine and isopropanol from the lysing and silica extraction steps. The device can be coupled directly to a PCR thermal cycler for downstream amplification and detection.

An electrochemical detection method employing probe functionalised IEMs developed by the Chang group[139,144] at Notre Dame promises rapid, label- and amplification- free detection of nucleic acids for portable diagnostics. Unlike conventional electrochemical DNA sensors[145] these ion selective membrane biosensors enable both pre-concentration and detection of negatively charged nucleic acid molecules on the same platform. This is an advantage over other electrode-based sensors that require a separate flow focusing technique to concentrate the analyte within the sensor recognition layer. However, pre-concentration time is strongly influenced by the conductivity of the buffer solution, with higher buffer conductivity leading to increased pre-concentration times. Efficiency of the detection system can be improved dramatically by purification of the biological sample solution prior to the pre-concentration step.

3.2 Materials and Methods

3.2.1 Protocol design

The pre-treatment protocol was based on the commercially available RNeasy Kit from Qiagen. This kit uses a miniature spin column with a silica plug for chaotrope-driven nucleic acid binding and consists of load, wash, and elution steps facilitated by centrifugal pumping. Figure 3.2 (A) shows the Qiagen RNA purification process. The process was adapted in this case to use a positive pressure syringe pumping system thus facilitating automation and improving portability for on-site applications. The modified assay is shown in Figure 3.2 (B).

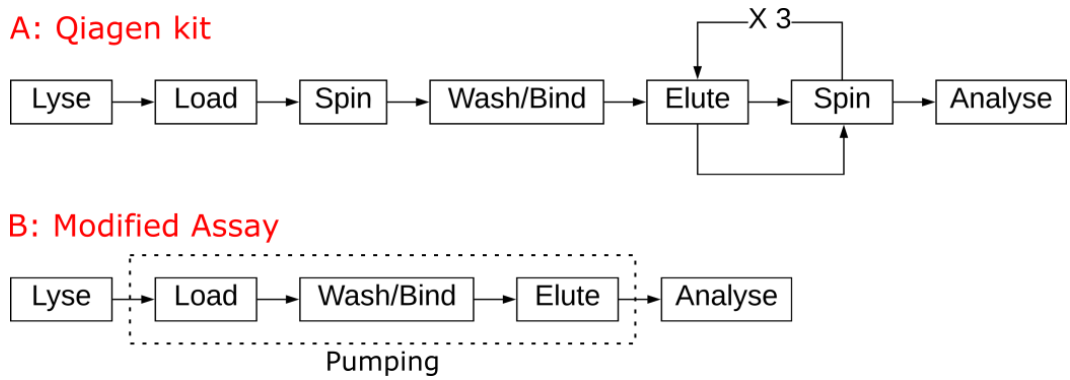

Figure 3.2. A) Qiagen RNeasy kit RNA purification procedure and B) the modified RNA purification assay used in this study. Samples can be used for sensing and amplification downstream applications.

3.2.2 Chip design

Each component was designed using SolidWorks 2015 (Dassault Systems, Waltham, MA) and sliced into individual layers using Asiga Composer 3D printer software (Asiga, Anaheim Hills, CA, USA). There are some key limitations to the fabrication method based on resolution of the 3D printing hardware in the vertical-direction. These limitations have previously been dubbed the "back-side effect"[8] and occur due to overcuring of the resin material inside microfluidic channels. These limitations have been overcome in this case by orienting the packing weir to benefit from reduced levels of overcuring in the horizontal direction as shown in Figure 3.3.

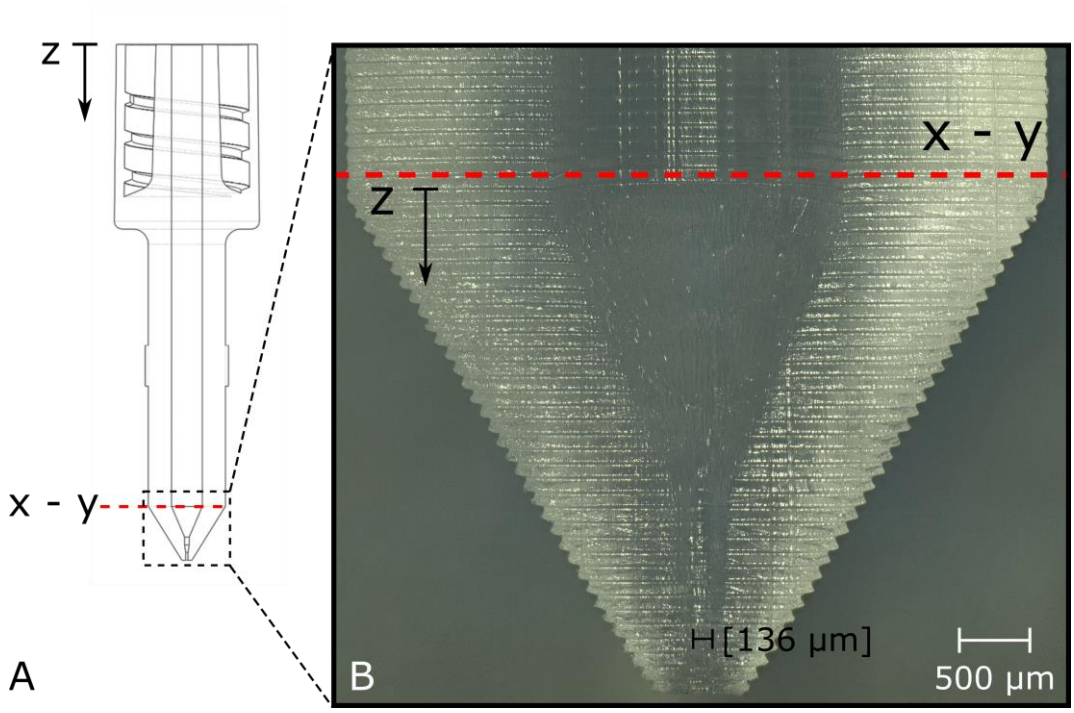

Figure 3.3. The SPE packing weir was oriented to benefit from higher resolution of the MPµSL printing process in the horizontal (*x*-*y*) plane. (A) CAD rendering of the SPE chip with integrated weir and (B) and microscope image of the chip cross-section taken using a Keyence VHX-2000 digital microscope. The integrated packing weir has a total diameter of 136 µm.

3.2.3 Fabrication of the 3D printed pre-treatment device

The SPE pre-treatment device was made using a DLP 3D printer (Asiga Pico Plus 27 - Asiga, Anaheim Hills, CA, USA). The printer has a resolution of 27 µm in the X-Y plane and an adjustable Z resolution which can be tuned to a step height of 10 µm. All pre-treatment devices used in this study were produced at a Z step resolution of 50 µm as this permitted adequate resolution at faster fabrication throughput. All parts were built using a clear methacrylate-based photopolymer resin commonly used to produce ear moulds (Freeprint mould - Detax GmbH & Co., Ettlingen, Germany). The photopolymer cures at a wavelength of 405 nm which is compatible with the Asiga LED light source and is biocompatible when fully cured. The exact composition of the resin material is proprietary; however the material safety data sheet[146] reports that it is a mixture of acrylic/methacrylic resins with auxilliary materials. Material properties of the polymer resin are outlined in Table 3.1.

Table 3.1. Material properties of Freeprint® mould material[146].

Property	**Test method**	**Freeprint® mould**
Colour	Standard light box	Transparent colourless
Viscosity	CP; gap 0.052 mm, cone 35 mm/1°; 23°C, shear rate 80 s^{-1}	622 mPas
Initial hardness (without post curing)	Zwick H04.3150	74 Shore D
Final hardness	Zwick H04.3150	79 Shore D
Flexural strength	Accord. To DIN EN ISO 178	75 MPa
Flexural modulus	Accord. To DIN EN ISO 178	1900-2100 MPa

The column was fabricated in a single step with integrated luer-lock fitting for connection to pumping and sensing peripherals. After fabrication, the part was removed from the 3D printer, submerged in a bath of Ethanol and sonicated for 20-30 minutes (Branson 5510 40 kHz sonicator). After sonication, the columns were removed and attached to a syringe using the integrated luer-lock fittings and flushed repeatedly with Ethanol and DI water until cleared. Finally, the columns were dried using compressed air and post-cured in a UV oven for 10 minutes. After fabrication, the column was filled with high purity grade SiO_2 particles (60 Å pore size, 40-63 µm particle size - Sigma Aldrich) using a small metal tool to pack against the packing weir and sealed using a standard luer-lock fitting. Figure 3.4 shows the fully packed SPE column with integrated luer-lock connection.

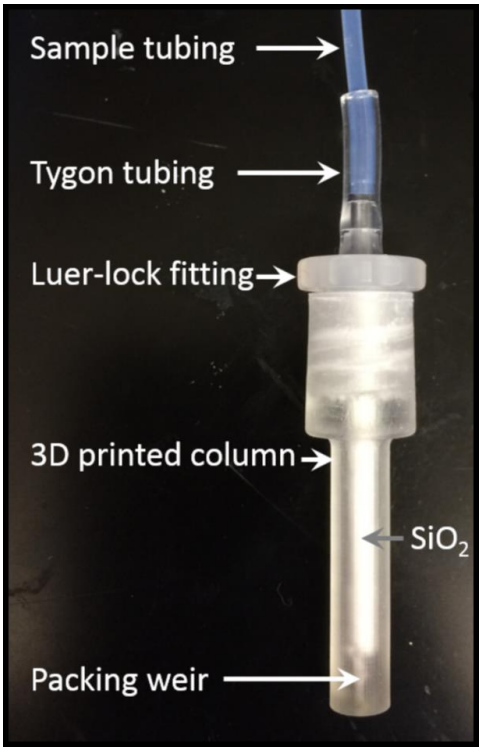

Figure 3.4. Solid phase extraction column with integrated luer-lock fitting packed with SiO_2 particles.

After fabrication, the SPE column was wet-packed and treated using 500 µl of RNase Zap (Sigma Aldrich) to remove RNase enzymes followed by 1 ml diethyl-pyrocarbonate (DEPC) treated water at a flow rate of 20-30 µl/min. During this step, the column and setup were monitored for leaks.

3.2.4 Sample preparation

All reagents were purchased from Sigma Aldrich unless otherwise indicated. Three cell types were used in this study; *E. coli*, *Brucella neotomae*, and Dengue viral cells (DENV). First, the cell samples were lysed using TRIzol® RNA isolation reagent (ThermoFisher Scientific) and the aqueous phase was extracted using a standard phenol-chloroform extraction procedure. An alternative cell lysis protocol adapted for low-resource settings was developed and compared with the standard lysis method for the three cell types used in this study. A comparison of the two lysis methods is shown in Figure 3.5.

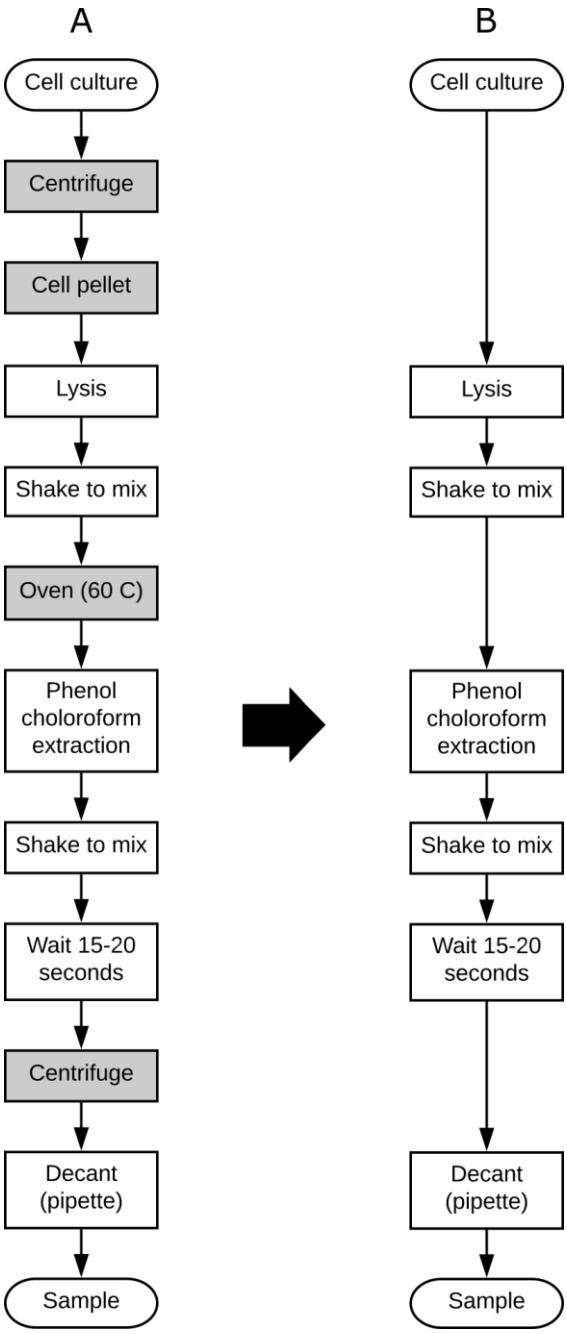

Figure 3.5. Procedure for cell lysis and aqueous phase extraction. Standard procedure (A) and modified procedure for field-based applications (B).

The modified lysis assay was developed for use in resource-poor locations with no access to standard laboratory equipment (e.g. centrifuge, oven). RNA yield for this new assay was compared to the standard method both qualitatively and quantitatively using gel electrophoresis and NanoDrop 2000c spectrophotometer (Thermo Scientific) respectively. The new method resulted in a reduction in RNA yield of 50-70% for the hard-to-lyse bacterial cells (*E. coli* and *Brucella neotomae*), but only 3% for dengue

viral samples. This can be attributed to the viral capsid which is easier to lyse and does not require such rigorous lysing conditions. This new protocol can be readily miniaturised for field based viral diagnostic or prognostic applications.

3.2.5 Solid phase extraction

After cell lysis, the aqueous phase was loaded on to the SPE column. An intermediate wash step was then used to selectively remove excess aqueous phase solution (salts) from the column leaving nucleic acids bound to the silica particles. Finally, nucleic acids were eluted using DEPC-treated water. The experimental workflow is outlined in Figure 3.6.

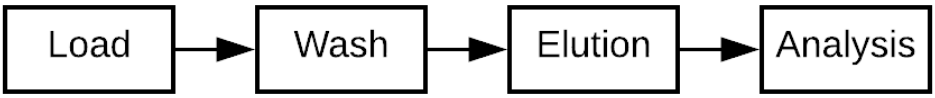

Figure 3.6. Solid phase extraction protocol.

Eluent fractions were taken throughout the procedure for further analysis and characterisation using a combination of methods including conductivity (B-173 conductivity meter, Horiba), UV-Vis (Nanodrop 2000c), gel electrophoresis, and qRT-PCR (q225, Kubo Technology). Conductivity of the eluted sample buffer is a key parameter in the assay design as it has a direct impact on pre-concentration time and thus overall assay time. A target of 2 mS/cm yields a preconcentration time of less than five minutes with pre-concentration time rising exponentially at higher buffer conductivities due to a higher concentration of ions in the solution which need to be depleted[139]. Two wash buffer elements were tested in this study including IPA and ethanol with respect to conductivity of the elution buffer.

3.3 Results and discussion

Initial gel electrophoresis results using the 3D printed SPE column are presented in Figure 3.7. Gel electrophoresis was performed in 1% agarose gel with MOPS buffer run at 120 V for 50 minutes.

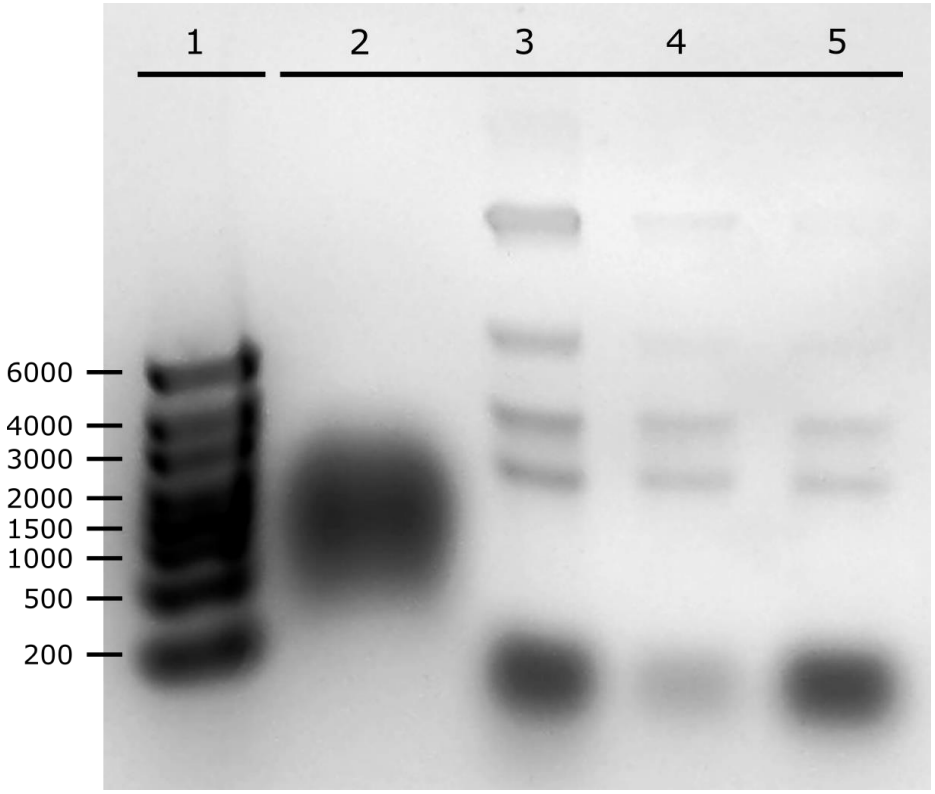

Figure 3.7. Initial verification of the pre-treatment protocol using a packed silica column and lysed *E. coli* cells. Lanes (L-R) include: (1) ribo ruler 6000-200bp; (2) aqueous phase loading buffer eluent; (3) first 40 µl DEPC water buffer elution; (4) second 40 µl DEPC water buffer elution; and (5) third 80 µl DEPC water buffer elution.

Initial verification of the pre-treatment procedure was performed using the standard lysing protocol to obtain the aqueous phase followed by sample loading and three-part elution in DEPC-treated water. This initial gel demonstrates the capability of the silica stationary phase for capture and release of nucleic acids. During the loading step, nucleic acids bind chaotropically to the silica particles due to the presence of bridging counter-ions and no bands are visible in the corresponding gel (lane 2, Figure 3.7). Following three-part elution in DEPC-treated water, the bridging counter-ions dissolve and the nucleic acid molecules become dislodged from the silica substrate, as

demonstrated by clear bands in the gel (lanes 3-5, Figure 3.7). In fact, most of the nucleic acid molecules elute in the first 40 µl of DEPC elution buffer as indicated by sharper bands in lane 3. This is confirmed using qRT-PCR (q225, Kubo Technology) as demonstrated in Figure 3.8 with wash step included.

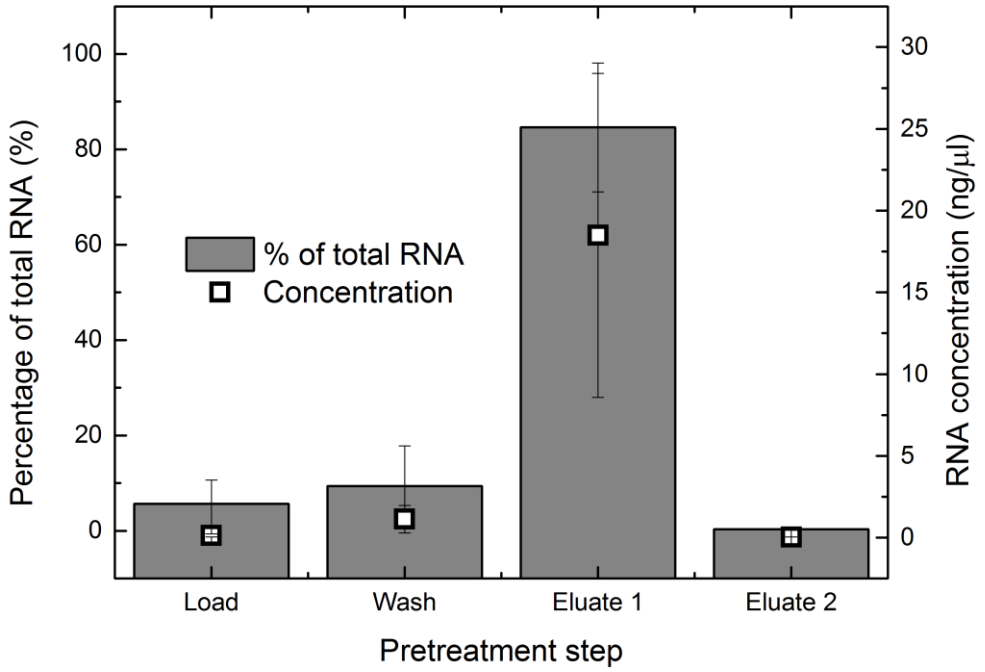

Figure 3.8. Elution profile as a percentage of total RNA measured, with corresponding RNA sample concentration (ng/µl). The bulk of the 16S and 5S RNA strands elute in the first 100 µl aliquot of elution buffer (eluate 1). The RNA (*Brucella neotomae*) elution profile was quantified using qRT-PCR to determine concentration of 16S and 5S RNA amplicons.

The elution profile obtained is typical of SPE elution profiles reported previously by Cady et al.[141] using silica as the stationary phase where bulk RNA elution occurs in the first 50 µl to 100 µl elution buffer. Addition of an intermediate wash buffer has minimal effect on the elution profile with some minimal RNA loss during the wash step. The wash buffer plays an important role in RNA binding and in reducing the conductivity of the eluent. Here, the effect of the wash buffer composition on nucleic acid retention and eluent conductivity was studied by varying two parameters; buffer composition and buffer volume. Eluent conductivity was measured throughout the pre-treatment process using the three wash buffers. Results are presented in Figure 3.9.

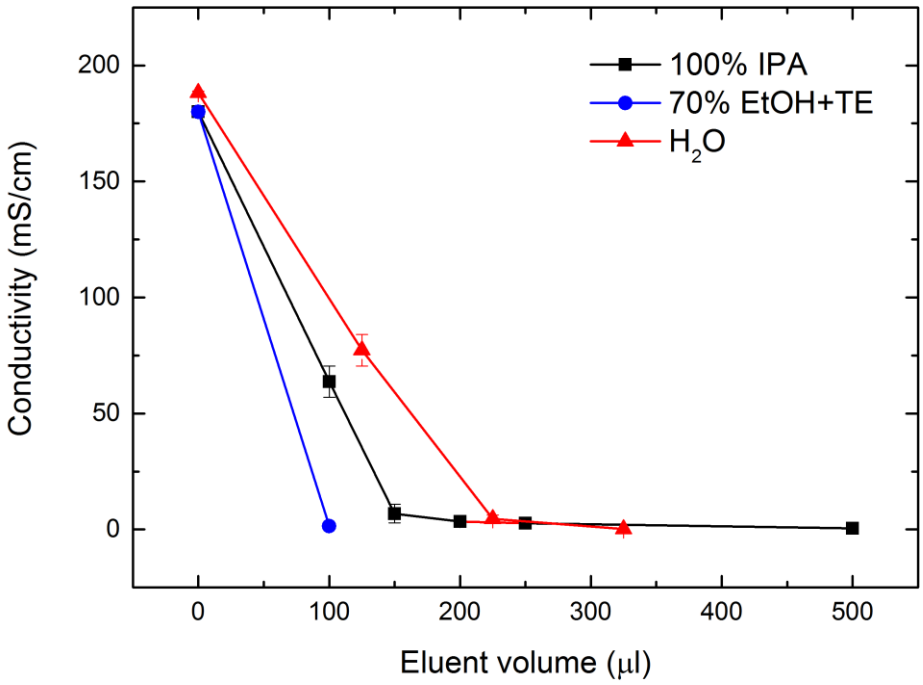

Figure 3.9. Eluent conductivity before, during, and after the wash step using two different wash buffers: 2-Propanol; and 70%Ethanol+TE. DEPC-treated H_2O was used as a control, simulating a scenario in which no wash buffer is used. Sample conductivity was reduced below 2 mS/cm after only 100 µl wash using 70%Ethanol+TE.

Of the buffers used, ethanol was found to be more efficient in reducing eluent conductivity while minimising nucleic acid loss during the wash step. Buffer alcohol content was also investigated by varying the volume of ethanol from 30-100% ($^{v}/_{v}$) in TE buffer solution, the ideal ethanol content was found at 70% ($^{v}/_{v}$). Using 70% ($^{v}/_{v}$) ethanol in TE wash buffer, sample conductivity was reduced below the target conductivity of 2 mS/cm in just 100 µl. This target conductivity corresponds to a pre-concentration time of five minutes with an increase in conductivity above this level yielding an exponential increase in pre-concentration time. In contrast, 100% IPA wash buffer and the DEPC-treated water control sample were less efficient, only achieving the target conductivity after 250 µl and 300 µl respectively. Furthermore, as water acts as an eluting agent, most of the nucleic acids are eluted in the first 100 µl to 150 µl before reaching the desired buffer conductivity.

The impact of wash buffer volume on RNA retention was examined using gel electrophoresis. *E. coli* cells were lysed and pre-treated on the SPE column using two

different volumes of IPA wash buffer, 250 µl (Figure 3.10, lanes 3-6) and 500 µl (Figure 3.10, lanes 7-9).

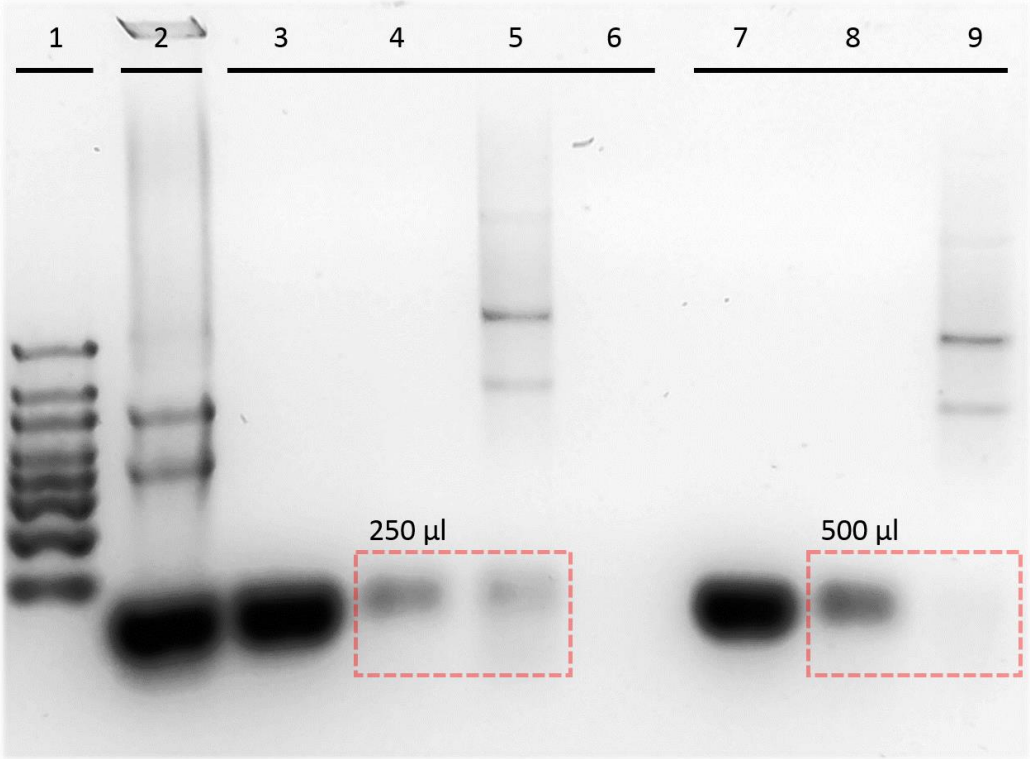

Figure 3.10. Wash buffer volume optimisation using two different volumes of IPA wash solution. Lanes (L-R): (1) Ribo ruler 6000-200bp; (2) control sample; sample 1 (lanes 3-6): (3) aqueous phase loading buffer eluent; (4) 250 µl wash buffer eluent; (5) elution 1; (6) elution 2; sample 2 (lanes 7-9): (7) aqueous phase loading buffer eluent; (8) 500 µl wash buffer eluent; (9) elution 1. All samples are E. coli RNA.

Results demonstrate that longer 16S and 5S RNA molecules stay bound to the column throughout the wash process for both volumes while smaller RNA fragments and lysis buffer remnants elute during the wash steps as indicated by a difference in the bottom bands (Figure 3.10, dotted lines) with the bottom band effectively washed through in the second sample (lane 9). The persistence of the longer RNA strands can be attributed to the enhanced binding potential when using the alcohol wash.

Column capacity with column length, particle size, and packing density impacting the total nucleic acid retention. Column design parameters were fixed throughout testing

while cell number was varied to determine column saturation. Table 3.2 outlines the column and stationary phase parameters that were fixed throughout testing.

Table 3.2. Solid phase extraction column and stationary phase parameters.

Parameter	**Value**	**Unit(s)**
Column diameter	2	mm
Column length	30	mm
Weir diameter	150	µm
Particle diameter	40-63	µm
Pore size	60	Å
Total weight of silica	43	mg
Packing flow rate	20-30	µl/min

To demonstrate the nucleic acid binding capacity of the column, RNA loss was measured as a percentage of the total RNA in the solution at three cell concentrations; results are shown in Figure 3.11.

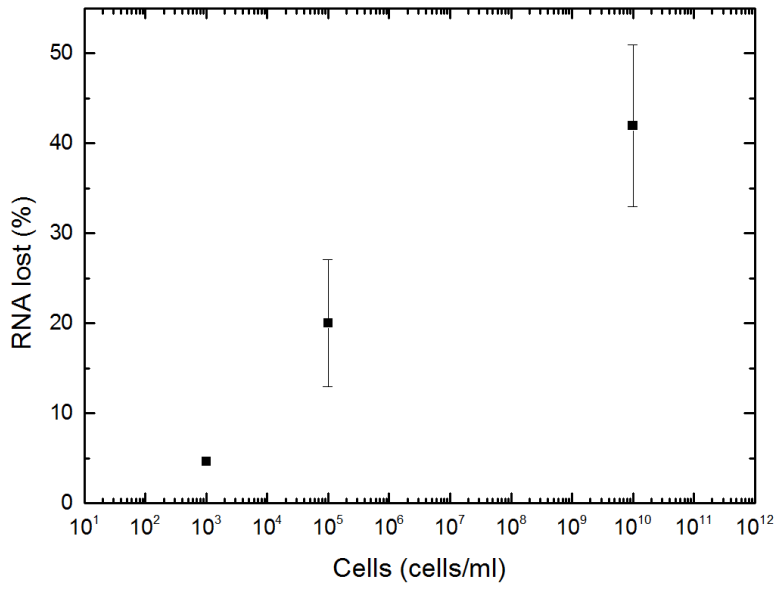

Figure 3.11. Graph of percentage RNA washed through during the column loading stage versus total *Brucella neotomae* cells loaded. A higher percentage of RNA is lost for larger cell numbers due to column saturation.

The graph demonstrates a stationary phase RNA saturation point for cell culture volumes above 10^3 cells/ml. Larger sample volumes necessitate a SPE column with greater surface area for RNA attachment. This can be achieved by increasing the column volume or improving the packing density by using a porous monolithic material.

3.4 Conclusions

A novel approach to stationary phase integration using a 3D printed column-weir was developed and tested for pretreatment of nucleic acid samples from a variety of cell types including *E. coli*, *Brucella neotomae*, and Dengue virus. Key limitations of the 3D printing method, namely resolution in the vertical direction, have been overcome by orienting the main weir feature to benefit from the higher resolution in the horizontal direction. In addition, a new protocol was developed enabling field-based pre-treatment and detection of nucleic acids for disease diagnosis. Results show efficient purification of nucleic acid molecules from the lysed cell solution. Effect of wash buffer volume and composition on conductivity of the purified sample buffer was examined and optimised based on the requirements of the electrochemical IEM detection method. Integration of pretreatment and sensing elements together in a closed system is necessary for on-site diagnostics where common laboratory equipment is not available.

Chapter 4

Microfluidic chip fabrication via Mask Projection micro-Stereolithography: An evaluation

4.1 Introduction

Mask Projection micro-Stereolithography (MPμSL) is a rapid prototyping technique capable of producing solid parts with micron-scale resolution from a vat of photocurable liquid polymer resin. Although the physical mechanism remains the same, the process differs from traditional laser-galvanometer based stereolithography in its use of a UV projector which cures each layer instantaneously. In this chapter, MPμSL is investigated as a new, cost-effective, fabrication technique for the production of milli- and micro-fluidic channels in the bulk polymer substrate in a single step. This rapid prototyping technique is uniquely suited to the production of internal channels due to the nature of the liquid polymer resin, which can be washed away after processing, and its ability to produce small overhanging structures without the need for support material. This is extremely beneficial when applied to the fabrication of microfluidic channels, enabling the production of completely encapsulated channels in a single step without the need to bond a secondary substrate, thus reducing the risk of delamination at high pressures. Despite these advantages, fabrication of milli- and micro-fluidic channels remains a challenge due to the resin overcuring effect; this effect is characterised with respect to channel build orientation. Overcuring has a greater effect on channels oriented horizontally with respect to the build platform due to the "back-side effect" which occurs when the photopolymer material inside the channel is exposed to UV light during fabrication of the channel enclosing layers.

Integration of threaded high-pressure fluidic fittings during the build process was also achieved and burst pressure was measured. Pressures up to 100 bar were observed before failure of the fitting through two observable modes, ferrule slip and thread leakage. Plasma treatment of the cured polymer material demonstrated the ability to tune the polymer surface charge for microfluidic applications.

4.2 Materials and methods

4.2.1 Chip design and fabrication

Three microfluidic chip design parameters (Table 4.1) were chosen including channel diameter/width, channel shape, and build orientation, to assess the effect of overcure on microchannel fabrication. The design parameters used in this study were based on the MPμSL 3D printing technique and a number of studies evaluating similar techniques for the production of microfluidic channels[7,8,102,117,147].

Table 4.1. Experimental design space.

Parameter	**Levels**	**N**
Shape	Square Circle	2
Dimension (μm)	500 750 1000	3
Build orientation	$A_{(0°,0°,0°)}$ $B_{(0°,0°,90°)}$ $C_{(90°,0°,0°)}$ $D_{(90°,0°,90°)}$ $E_{(0°,90°,0°)}$ $F_{(0°,90°,90°)}$	6
Repetitions	1, 2, 3	3
	Total	108

A set of experiments were designed around these parameters and four chip designs were created using SolidWorks™ 2013 3D modelling software, an example of the chip design is shown in Figure 4.1. Each chip was designed with three channels of the same shape and size spaced evenly apart to test channel repeatability.

Euler's angles were used to analyse the relationship between channel build orientation and overcure. Each part was built in six orientations (Figure 4.2) and the corresponding channel dimensions were measured using a VHX-2000 Digital Microscope (Keyence, Osaka, Japan) at the channel entrance.

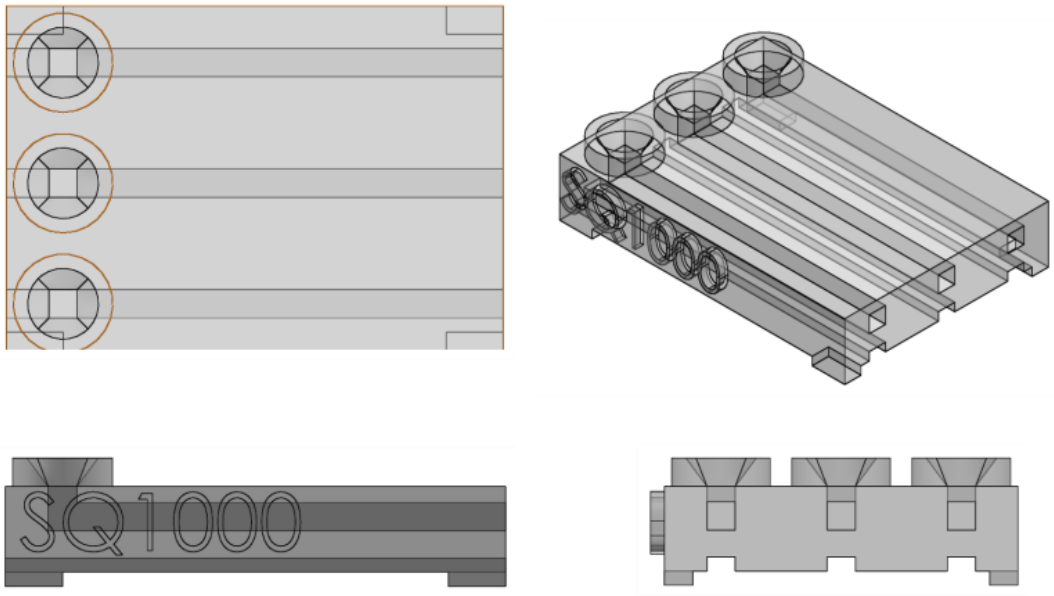

Figure 4.1: Microfluidic chip design for characterisation of MiiCraft HR 3D printer.

A MiiCraft DLP 3D printer (Young Optics, Taiwan) was used to fabricate microfluidic devices in MiiCraft Cream acrylic polymer material at a slice thickness of 25 µm. Characterisation of the MiiCraft DLP printer was performed previously by Shallan et al.[8] (Figure 2.17). They report on the fabrication of square fluidic channels with a minimum width and height of 250 µm. In this study, it was found that long channels (>15 mm) with dimensions below 500 µm became blocked with resin material and could not be cleared, therefore only channel dimensions of 750 and 1000 µm are analysed in the results presented.

Analysis and characterisation of the overcuring effect was carried out using a similar DLP 3D printer (Pico+27, Asiga, Anaheim Hills, CA, USA) using an acrylate-based polymer material (Freeprint mould clear, DETAX GmbH, Germany). This printer was also used to fabricate microfluidic channels with integrated fittings for burst pressure testing using the same material.

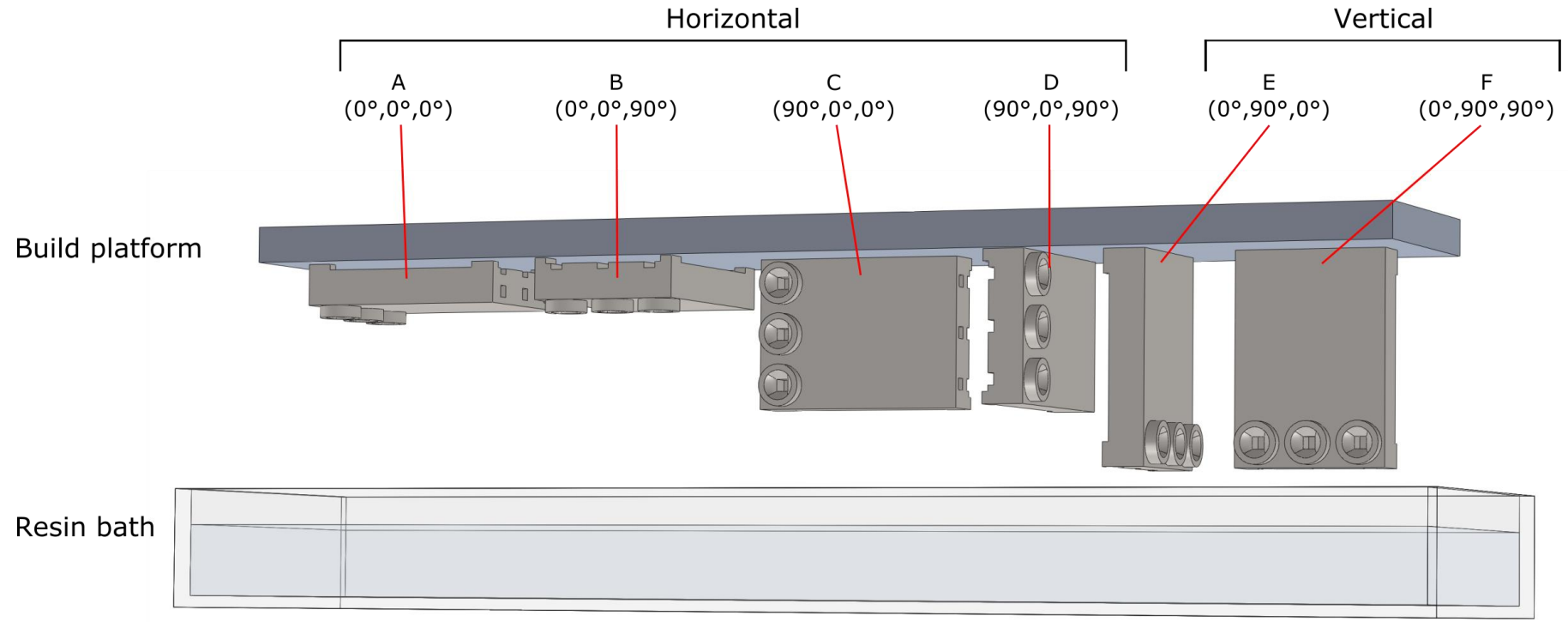

Figure 4.2: Six orientations (A-F) based on Euler's angles. Building in six orientations enabled characterisation of the internal fluidic channels and print resolution along each plane in X, Y and Z. Orientations A-D contain channels oriented horizontally (parallel to the build platform) while orientations E and F contain channels built vertically (normal to the build platform).

4.2.2 3D printed microfluidic fittings

Female 10-32 Upchurch microfluidic fittings were designed using SolidWorks™ 2013 3D modelling software, a 3D CAD rendering is presented in Figure 4.3.

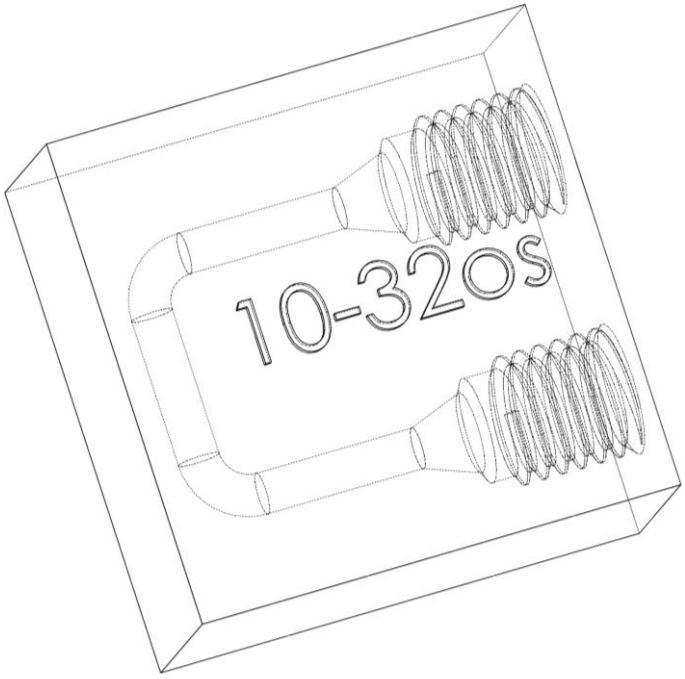

Figure 4.3. CAD model of microfluidic chip with female threaded 10-32 ferrule fittings for burst pressure testing. One end of the chip was blocked using a blank 10-32 fitting during testing.

Before testing, the microfluidic channel was primed with de-ionised water and one end was blocked using a blank Upchurch 10-32 PEEK fitting (Sigma Aldrich, Ireland). The inlet was connected to a HPLC pump (Smartline 100, Knauer GmbH, Germany) using a 10-32 Upchurch ferrule fitting and 1/16" O.D. PEEK tubing (Sigma Aldrich). 3D printed fittings were tested at a flow rate of 1 ml/min.

4.3 Results and discussion

4.3.1 Dimensional analysis

Fabrication of square and circular channels <750 μm in diameter and side length respectively proved extremely difficult due to channel blockage during printing and removal of the viscous semi-cured gel-like polymer after printing. As a result, only 750 μm and 1000 μm channels are presented in the following section.

One-way analysis of variance (ANOVA) was carried out to investigate the significance of build orientation on channel output dimension. The Bonferroni post-test was performed to analyse dimensional variance between the build orientations and the Dunnett post-test was performed to analyse variance between the build orientation and the input channel dimension. Using the Bonferroni post-test analysis, orientations A and B were found to be significantly different from all other orientations, including each other for width and height measurements. The Dunnett test shows that the measured values are significantly different to the input value. For all sets of values, there exists a significant difference between the sets of mean values measured ($0.0001 \ll p < 0.095$) and between the mean values and the input value ($0.0001 \ll p < 0.095$).

Of the six build orientations analysed, orientations E and F are the only channel measurements to show correlation with the input values for all shapes and input dimensions. This can be seen in Figure 4.4, with mean values for orientations E and F falling closest to the input value. In addition, there is no statistical difference between orientations E and F and the input channel dimensions, according to the Dunnett post-test. This can be seen in the optical microscope images in Figure 4.5, and in Appendix A

Horizontal channels are prone to blockage as the UV curing light penetrates through the cured layers into the microfluidic channels while the enclosing (bottom) layers are being built. This concept is illustrated in Figure 2.22, showing the pronounced effect of overcuring on channels oriented horizontally. This has previously been dubbed the "back-side effect"[8,13] and results in increased surface roughness on unsupported channels and overhangs due to the uneven intensity profile of each pixel and the inhomogeneity of the base resin. The back-side effect does not occur in vertical orientations E and F as channels are fully supported and there are no overhanging

features. Overcuring is visible around the edges of the channels but to a lesser extent. This can be attributed to constructive interference between individual DMD pixels[123].

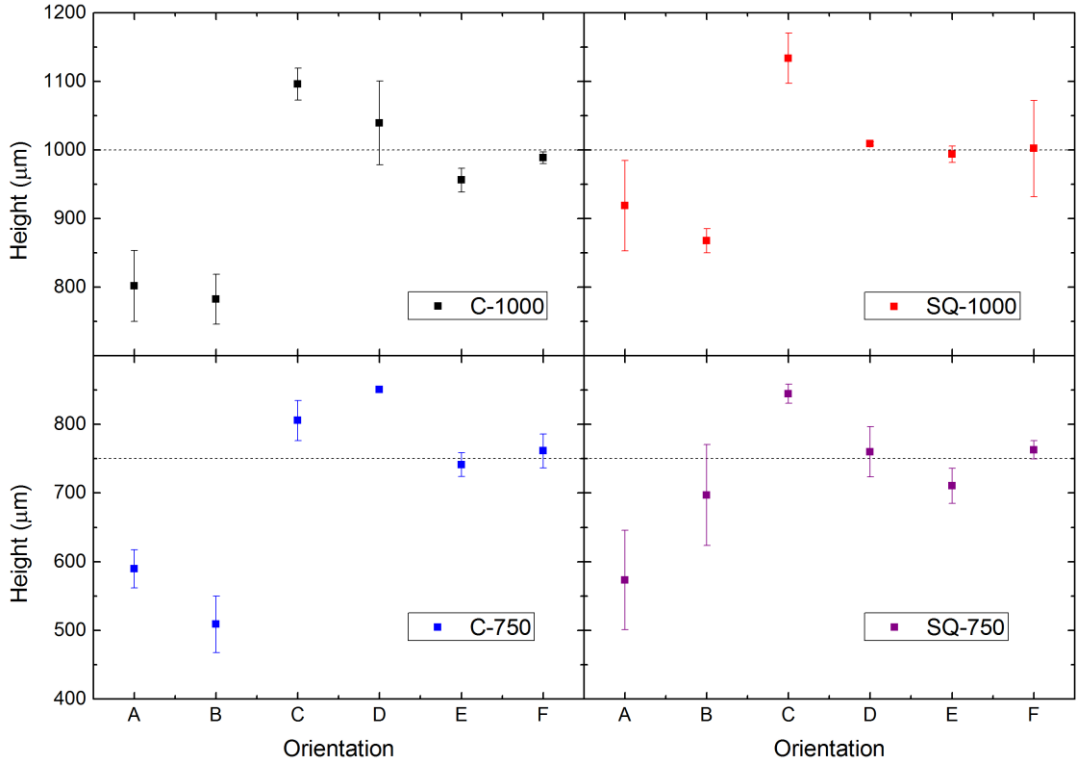

Figure 4.4: Mean height (diameter) of circular and square channels at each orientation A-F. Vertical channel orientations E and F consistently show close correlation with the input dimension. All dimensions were measured at the channel outlet. Error bars show 80% confidence interval (CI) ($n = 3$).

.

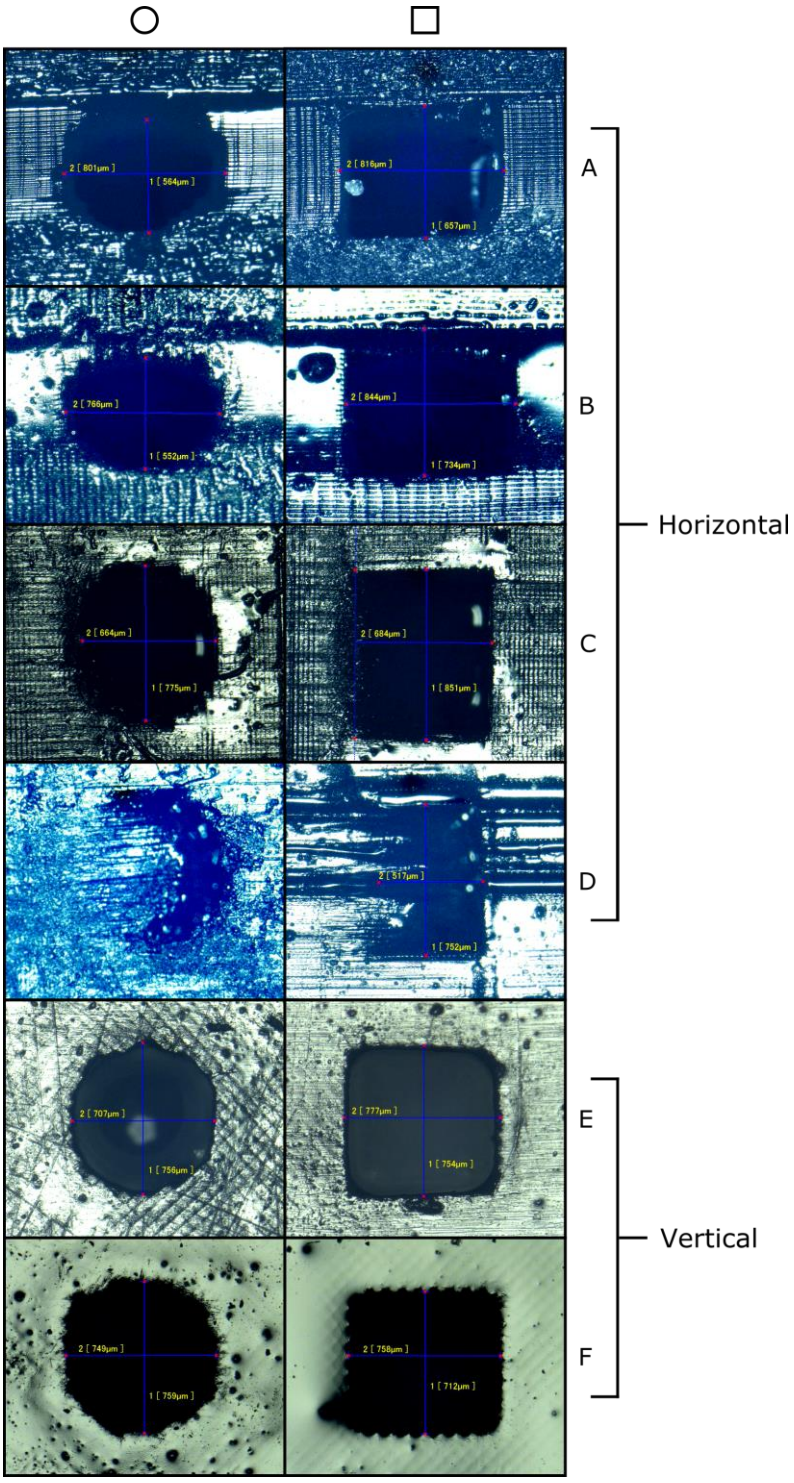

Figure 4.5. Circular and square cross-section microfluidic channels printed via MPμSL. Input channel dimension for circular and square channels was 750 μm diameter and side length respectively. Horizontal orientations A-D are poorly defined showing in a higher variance in channel dimension with most prints resulting in blocked channels. Vertical orientations E and F are well defined showing less variation in channel dimension and greater agreement with the input channel dimensions.

4.3.2 Characterisation of the overcuring effect

The effect of the number of enclosing layers on the level of overcuring was studied for two sets of microfluidic channels fabricated at slice thickness levels of 25 μm and 75 μm respectively. Square channels (600 × 600 μm) with enclosing layers $1 \leq \lambda \leq 10$ were fabricated using a DLP 3D printer (Pico +27, Asiga, CA, USA) using Freeprint mould material (DETAX GmbH, Germany). Level of overcuring was calculated as the difference between the input channel height and the resulting 3D printed channel height; results are shown in Figure 4.6.

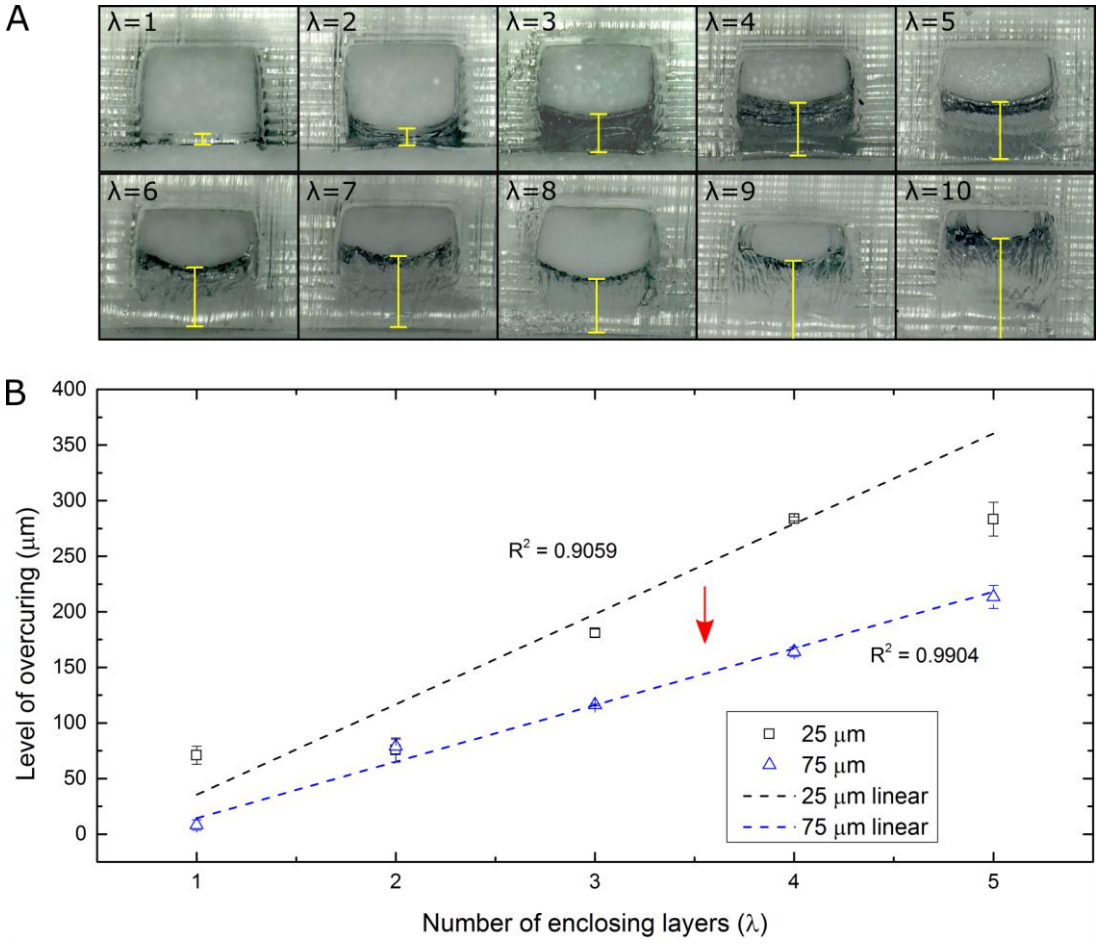

Figure 4.6. Increasing the number of enclosing layers results in a greater degree of overcuring. (A) Raw images of 3D printed microchannels with enclosing layers $1 \leq \lambda \leq 10$. (B) Level of overcuring (μm) as a function of the number of enclosing layers (λ) for 25 μm and 75 μm slice thicknesses with layer exposure times of 0.9 s and 1.4 s respectively. Error bars are standard deviation ($N \geq 3$).

As expected, an increase in the number of channel enclosing layers results in an increase in the level of overcuring for both 25 μm and 75 μm slice thicknesses. However, the degree of overcuring is also strongly influenced by the slice layer thickness; decreasing as slice thickness is increased from 25 μm to 75 μm.

Overcuring occurs due to excess exposure to the UV curing light during the MPμSL process and occurs to a greater extent in transparent resin materials that contain fewer light-blocking dyes or pigments. Improvements in polymer science allowing increased accuracy in control of cure depth may be able to mitigate for this. Gong et al.[12] studied the effect of resin material absorbance on the formation of microfluidic channels and voids using the MPμSL technique and were able to define the minimum flow channel height as ~3.5-5.5 h_a (where h_a is the characteristic optical penetration depth of the resin) and minimum channel width as four pixels in the build plane. Reduction of resin cure depth can be achieved using a combination of UV filters oxybenzone (commonly found in sunscreen) and TiO_2 as demonstrated by Mott et al.[148], however mechanical properties of the resulting polymer material were poor. Reduction of overcuring can be achieved using these strategies but requires an in-depth knowledge of the physical characteristics of the polymer resin.

4.3.3 Burst pressure test

3D printing offers many advantages over conventional microfluidic fabrication methods; one of the main advantages is the ability to fabricate standard microfluidic fittings in place on chip without the need for additional bonding. The ability to 3D print threaded fittings, while difficult, is extremely beneficial and opens up a range of modular applications by enabling interconnectivity between chips and to peripherals. The benefits of this modularity have been cited widely in the literature, with many researchers publishing on the topics of "modular microfluidics" and "chip-to-world interfaces"[149–155].

The most common threaded connections are Upchurch 6-32 and 10-32 fittings (IDEX Health & Science) and are used to interface with PEEK tubing using a ferrule that locks tight around the tubing when screwed in place. Figure 4.7 (inset) shows a 6-32 PEEK Upchurch fitting secured in place in a 3D printed block. Burst pressure testing was performed on a similar 10-32 Upchurch fitting with results displayed in Figure 4.7.

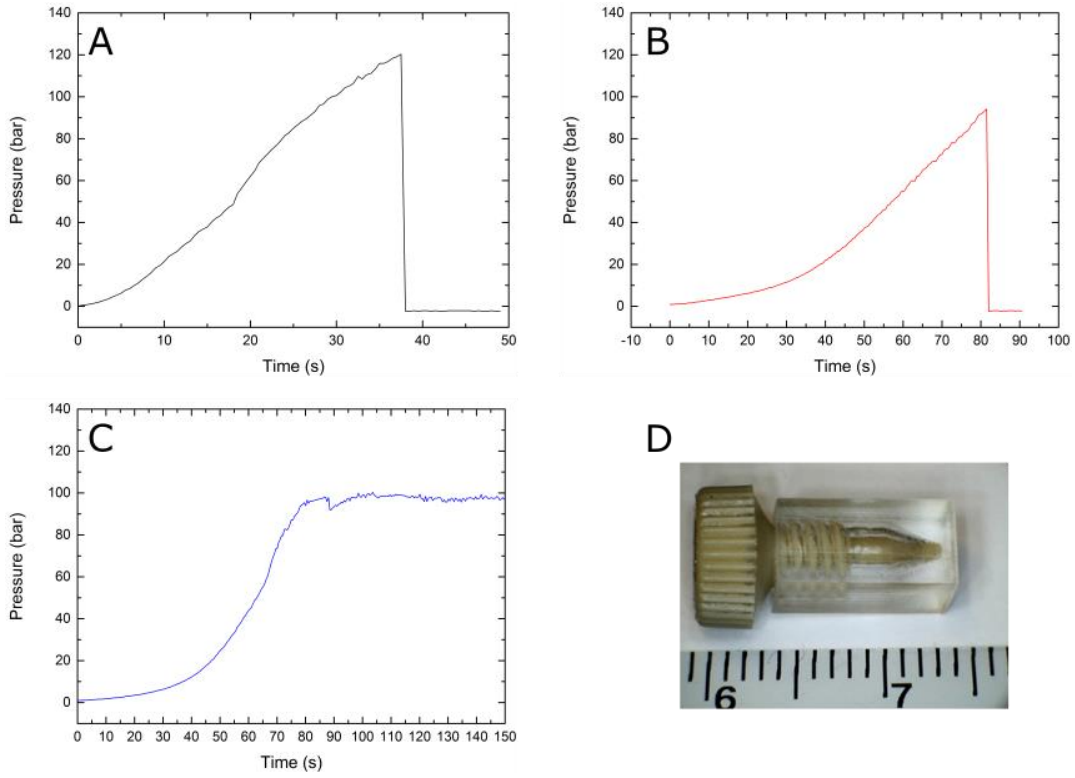

Figure 4.7: Failure modes for Upchurch 10-32 threaded microfluidic fittings. (A) Fast failure of the microfluidic fitting at ~120 bar due to ferrule slip after the initial test. (B) Fast failure at ~100 bar during the second trial. (C) Failure due to thread leakage at ~100 bar after repeated usage. (D) An example of a 3D printed Upchurch 6-32 fitting.

Two failure modes were observed during testing including ferrule slip and thread leakage. Ferrule slip is a fast failure mode caused by insufficient holding pressure at the interface between the ferrule and the PEEK tubing. Increased resistance to ferrule slip may be obtained by altering the ferrule angle. Thread leakage was only observed after repeated insertions of the fitting ($n > 3$) due to wear of the 3D printed thread. Maximum pressure obtained over the course of the experiment was 120 bar (12 MPa) for a single use fitting. Repeated testing resulted in failure of the threaded connections at ~100 bar.

4.3.4 Plasma treatment

The ability to modify the substrate material surface energy is often beneficial for microfluidic applications. Figure 4.8 shows the contact angle (CA) of the cured acrylic photopolymer resin (PlasClear, Asiga, CA, USA) before and after treatment in oxygen plasma.

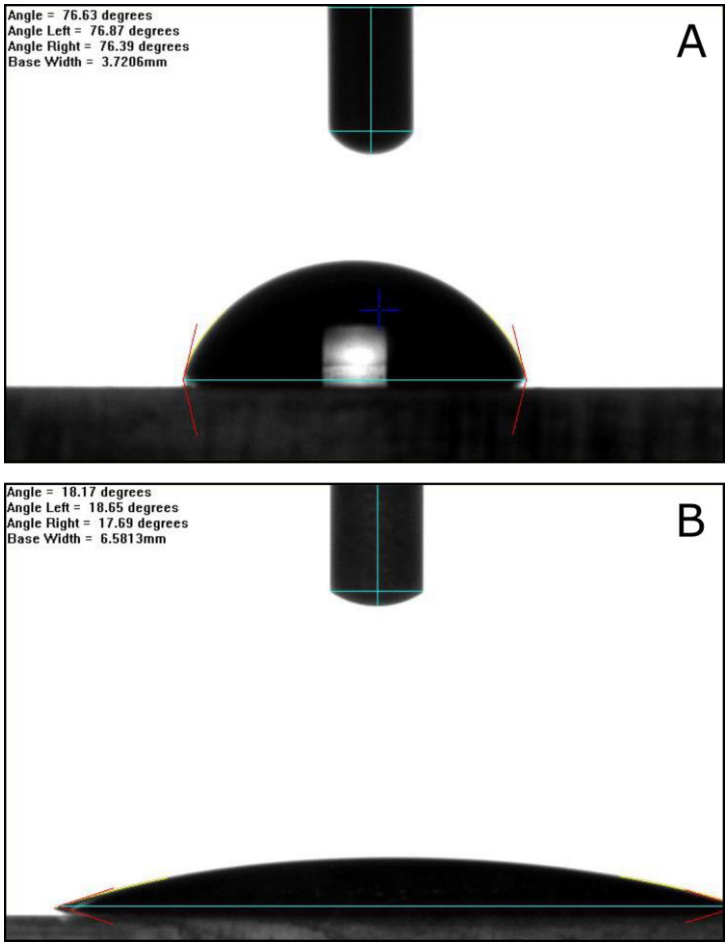

Figure 4.8. Contact angle (CA) of 3D printed PlasClear material. (A) Before plasma treatment, CA = 77°; (B) After O_2 plasma treatment for 5 minutes, CA = 18°.

After treatment for five minutes the substrate surface energy increases with CA changing from 77° to 18°. This increased wettability is advantageous, supporting electroosmotic pumping and facilitating priming of microfluidic channels when filling with liquids with high surface energies (particularly aqueous solutions) which is often difficult[34]. Depending on the polarity of the analyte, channel hydrophobicity can be tuned to prevent adsorption of chemical components to the channel walls which can reduce band broadening in chromatographic applications[156].

4.4 Conclusions

3D printing has recently gained popularity among researchers in the field of microfluidics. Stereolithographic fabrication methods have gained traction due to their ability to produce internal features at smaller scales than other AM methods and without the need for support structures. Here, a variation on stereolithography, MPμSL was investigated as a method to produce microfluidic channels and features. Results presented show that feature size depends on several key parameters including material, channel orientation, layer height, channel shape, and curing time. Circular channels below 750 μm were fabricated repeatably in heterogeneous polymer material demonstrating the ability of the process to produce internal voids without support material. Penetration depth of the resin material was found to be a key parameter influencing the resolution, minimum void size, and the level of overcuring present.

High pressure threaded microfluidic fittings were designed and printed using the MPμSL process in a single step. Female threaded holes exhibited two failure modes under high pressure flow; ferrule slip and thread leakage. Maximum backpressure reached before failure was 12 MPa; this may be improved upon by increasing ferrule angle to provide a tighter interface between the fitting and tubing.

Finally, plasma treatment of the acrylic photopolymer demonstrates the ability to modify surface charge and increase wettability of the material supporting electroosmotic pumping and facilitating priming of microfluidic channels when filling with liquids with high surface energies.

Chapter 5

A new design algorithm for mitigation of the overcuring effect in Mask Projection micro-Stereolithography

5.1 Introduction

A significant obstacle in fabrication of internal voids via MPμSL is the effect of overcuring. This results in poor resolution and blockage of microfluidic channels during fabrication limiting the minimum size of a microfluidic channel (see Figure 2.22, Figure 4.5 and Figure 4.6).

One way to avoid this phenomenon is to increase the absorbance of the resin material to impede penetration of the curing light through the polymer material. This results in a reduction in the material characteristic penetration depth h_a. This approach was taken by Gong et al.[12] who succeeded in creating a high-resolution photopolymer resin enabling the production of smaller channels. They developed a model, based on the exposure threshold model for the MPμSL process using the model as a basis for the optimum absorption characteristics of the photopolymer resin material. Exploring the effect of material characteristics: resin characteristic penetration depth (h_a), and critical time (T_c) on the level of overcure, they also demonstrate the effect of build parameters including layer slice thickness and number of channel enclosing layers. Slice thickness shows an inverse relationship with the level of overcure, with smaller slice thickness levels corresponding to greater levels of overcure: while an increase in the number of enclosing layers showed a positive relationship with the level of overcure. Results show that the typical minimum microchannel height depends largely on the resin parameter h_a, with minimum achievable height for a given photopolymer resin in the range ~$3.5 – 5.5\ h_a$. In a separate study, Choi et al.[13] use the same approach to increase the resolution of a photopolymer material using the light absorber Tinuvin 327. The light absorber was found to reduce the characteristic penetration depth providing increased control over the cure depth when printing and providing higher

depth resolution (see Figure 2.23). However, a side effect of doping the photopolymer resin is the need for increased layer exposure time leading to a reduction in print speed of the MPμSL process.

Building on their previous research, Gong et al.[123] further demonstrate the ability to fabricate high resolution microfluidic channels using custom-built high-resolution MPμSL hardware. By matching the 3D printer light source spectrum to the absorption spectrum of their bespoke photopolymer resin they achieved higher depth-resolution than was previously possible. This enabled the production of microfluidic channels with 18 × 20 μm cross-section using the MPμSL technique. This printer-resin combination demonstrates a combined approach to solving the problem of overcuring. These are the two most common approaches taken in the improvement of MPμSL resolution; i.e. (1) altering the base resin material characteristics, and (2) improving the MPμSL printing technique.

A third approach was taken by Limaye and Rosen[137,138] who developed a mathematical model to predict and avoid the so-called print-through error that results in the vertical dimension of an MPSL build when multiple layers are stacked, they called their method the "Compensation Zone Approach". Using this approach, the MPμSL process is modelled and problem areas where overcuring is present are identified. Like Gong et al.[12,123] they use the exposure threshold model in their calculations. A defined volume of material (the compensation zone) is then subtracted from underneath the CAD model to compensate for the predicted increase in dimension that would occur due to overcure. This model could, in theory, eliminate print-through errors completely, resulting in part geometries that closely correspond to the input model geometry. However, this approach only applies to print through errors on the exterior of the designed part. As of yet, no effort has been made to mitigate for the overcuring effect in internal voids such as microfluidic channels.

The approach discussed in this chapter is similar although compensation is performed throughout the entire part, not just simply at the final layer. In addition, this new approach is suitable for both internal and external features, where previously only external feature dimension was considered.

5.2 Theory

In this section, a simple model for the optical dose delivered to a photopolymer resin during the exposure of a single layer is introduced. Characteristic material parameters, concepts and mathematical notation are presented. The mathematical model presented here is expanded further when scaling the model up to two and three dimensions in section 5.3.3. For further detail on the derivation of this model refer to books by Jacobs[134,157], and Gibson et al.[118] and papers by Gong et al.[12,123], Choi et al.[13], Limaye et al.[137], Zissi et al.[136] and Vitale and Cabral[158].

Model assumptions:

1. Exposure is additive for each layer
2. Interference between DMD pixels is negligible
3. Threshold model of resin cure is valid
4. The resin molecules underneath the part being cured are stationary
5. The cleaning process can completely remove the surrounding uncured resin

5.3 Mathematical model

The MPSL process can be modelled using the absorption coefficient α (μm^{-1}) of the photopolymerisable resin to predict how deep the incident curing light will travel into the resin and thus predict the thickness of the final cured layer. The basis for the mathematical model is the Beer-Lambert law[157] which states that the absorbance of a material sample is directly proportional to its thickness and the concentration of the attenuating species in it. This concept is demonstrated in Figure 5.1.

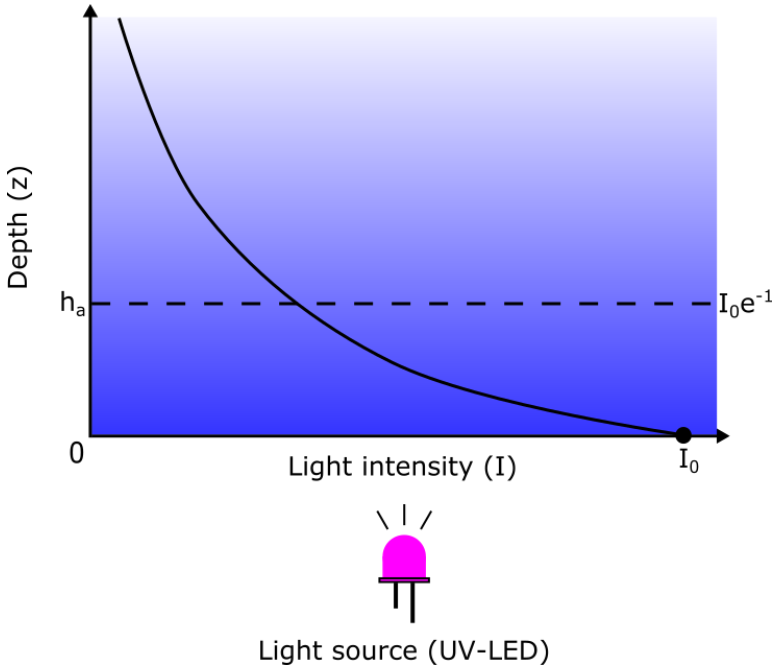

Figure 5.1. Illustration of Beer's law as applied in the process model with definition of the characteristic penetration depth h_a. Adapted from Gong et al.[12].

This model operates in the half-space $z \geq 0$, $I \geq 0$ where light is incident from the direction of $z < 0$ and propagates in the $+z$ direction. The first concept of interest in this model is irradiance (I) which is the radiant power of the light source per unit area in W.cm^{-2}. In the case of the Asiga 3D printer the radiant power is distributed evenly over the area exposed to the UV-LED by the DMD. The optical irradiance at the interface between the build tray and the resin at $z = 0$, is I_0. This incident light, I_0, is attenuated by the liquid photopolymer, with absorption coefficient α (cm^{-1}), as it passes through the material.

The irradiance at any point in the resin depth $z \geq I(z)$ is related to the irradiance at the surface by the Beer-Lambert law where the characteristic penetration depth is defined as $h_a = 1/\alpha$:

$$I(z) = I_0 e^{-\alpha z} = I_0 e^{-z/h_a} \tag{5.1}$$

This equation serves to highlight the meaning of the characteristic penetration depth, h_a. By setting $z = h_a$ it is understood that the irradiance at a depth of h_a is roughly 37 % ($e^{-1} = 0.36788$) of the irradiance at the surface. Thus, h_a is the resin depth at which the irradiance has been attenuated such that it is 37 % of the irradiance at the surface. In addition, since the Beer-Lambert Law holds, h_a is a material property of the resin and can be measured.

The corresponding dose, $D(z,t)$, in units of J.cm^{-2} for an exposure time of t is

$$D(z,t) = tI(z) = tI_0 e^{-z/h_a} \tag{5.2}$$

From this equation the critical dose, D_c, is defined as the dose at which polymerisation occurs and has proceeded to the 'gel point' threshold of the photopolymer material as shown in Figure 5.2 where 'X' represents the threshold. It is at this point that the polymer can be considered solid or nearly solid.

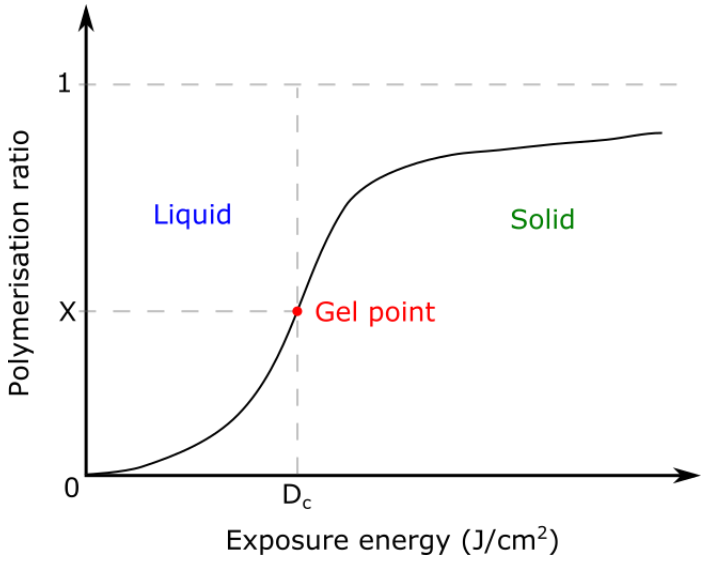

Figure 5.2. Gel point of a photopolymer. 'X' represents the threshold ratio at which the polymer can be considered solid. Adapted from Zissi et al.[136].

The value of D_c is a material property of the photopolymer resin and is specific to the interaction between the photopolymer resin and the curing source spectrum. The critical dose at a distance $z = z_p$ is given by

$$T_c = D_c / I_0 \tag{5.3}$$

Using this definition and solving equation (5.2) the polymerisation depth z_p can be expressed as

$$z_p = h_a \ln\left(\frac{t_p}{T_c}\right) \tag{5.4}$$

or, in unitless parameters, $\zeta = z/h_a$ and $\tau = t/T_c$,

$$\zeta_p = \ln \tau_p \tag{5.5}$$

From this equation, it is understood that when $\tau_p = 1$, $z_p = \zeta_p = 0$, regardless of h_a. Thus, when the exposure time reaches the critical point T_c the resin at $z = 0$ receives just enough dose to reach the gel point and become solidified, whereas the resin above this point at $z > 0$ remains liquid. Hence, when $\tau_p \geq 1$, the resin at $z = 0$ receives a dose that is τ_p times larger than the critical dose, T_c (as $t_p = \tau_p T_c$). For example, if $\tau_p = 5$ then $\zeta_p = \ln 5 = 1.6$ such that $z_p = 1.6 h_a$ and at $z = 0$ the resin receives five times the critical dose.

From equation (5.2) and (5.3) the normalised dose, $\Omega(z, t)$, can be expressed as

$$\Omega(z, t) = \frac{D(z, t)}{D_c} = \frac{t}{T_c} e^{-z/h_a} \tag{5.6}$$

or in unitless form

$$\Omega(\zeta, \tau) = \tau e^{-\zeta} \tag{5.7}$$

Similarly, when $\Omega \gtrsim 1$, the resin receives enough dose to be solidified and when $\zeta = 0$ the normalised dose is equal to τ. These relationships are plotted in Figure 5.3[12]. The variation of polymerisation depth, z_p, with normalised layer exposure time τ_p is plotted in Figure 5.3 (A). This graph is similar to the concept of the resin working curve presented in section 2.4.2.

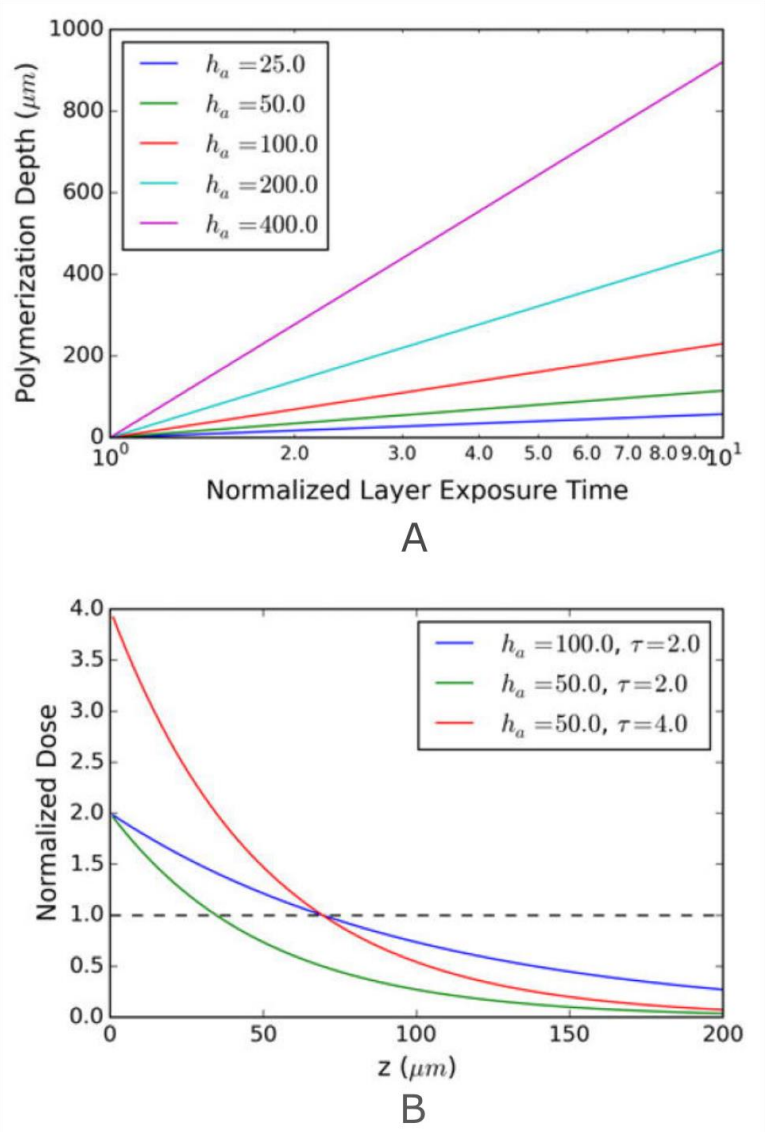

Figure 5.3. (A) Polymerisation depth, z_p, as a function of the normalised layer exposure time τ_p, equation (5.4) for different levels of resin characteristic penetration depth, h_a. (B) Normalised dose, Ω, as a function of depth, z, for different values of h_a and the normalised exposure time, τ.[12]

Figure 5.3 (B) shows the normalised dose Ω as a function of depth, z for different values of h_a and τ. The polymerisation point where $\Omega = 1$ is shown here by the dotted line. It is noted that smaller values of h_a require longer exposure times, and as a result the inhomogeneity of the layer increases. Conversely, larger h_a values require shorter exposure times and as a result the material beyond the polymerisation depth receives a larger dose than for smaller values of h_a. This is the fundamental trade-off in minimising microfluidic channel height in a 3D printed microfluidic device.

Table 5.1. Resin curing model parameters.

Parameter	**Symbol**	**Unit(s)**
Absorption coefficient	α	μm^{-1}
Characteristic resin penetration depth	h_a	μm
Curing time	t	s
Depth	z	μm
Polymerisation depth	z_p	μm
Polymerisation time at depth z_p	t_p	s
Optical irradiance	I	$W.cm^{-2}$
Optical irradiance at the interface	I_0	$W.cm^{-2}$
Dose	D	$J.cm^{-2}$
Critical dose	D_c	$J.cm^{-2}$
Critical time	T_c	s

Table 5.2. Resin curing model unitless parameters.

Parameter	**Symbol**	**Equation**
Normalised depth	ζ	z/h_a
Normalised polymerisation depth	ζ_p	z_p/h_a
Normalised time	τ	t/T_c
Normalised polymerisation time	τ_p	t_p/T_c
Normalised dose	Ω	D/D_c

5.3.1 Internal void formation – Theory

A schematic of the layer-by-layer fabrication of a simple square microfluidic channel is presented in Figure 5.4. The Asiga Pico+27 uses the inverted mask projection SL configuration with projection optics located beneath the transparent build tray, thus the part is built upside-down on the build platform. When the flow channel is formed in Figure 5.4 (C) the flow channel region is masked, leaving the resin in that region in the unpolymerized liquid state. This resin becomes trapped inside the part when the enclosing layers Figure 5.4 (D) are polymerised. Some of the irradiance used to polymerise the enclosing layers (layers 5 and 6) bleeds into the flow channel as the enclosing layer does not absorb all the incident light. This continues as each subsequent layer is exposed and causes the polymerisation of the resin inside the flow channel if the sum of the received doses reaches/surpasses the polymerisation threshold; thus, causing solidification and blockage of the channel. To mitigate for this, the flow channel z-dimension must be made taller so that the final channel size corresponds to the desired input. This is a key constraint that is critical to the design algorithm presented in section 5.3.4.

In the following section a mathematical model, previously developed by Gong et al.[12] for total optical dose in a multi-layered part, is described in detail. This model is the basis for the 2D and 3D models developed in section 5.3.4.

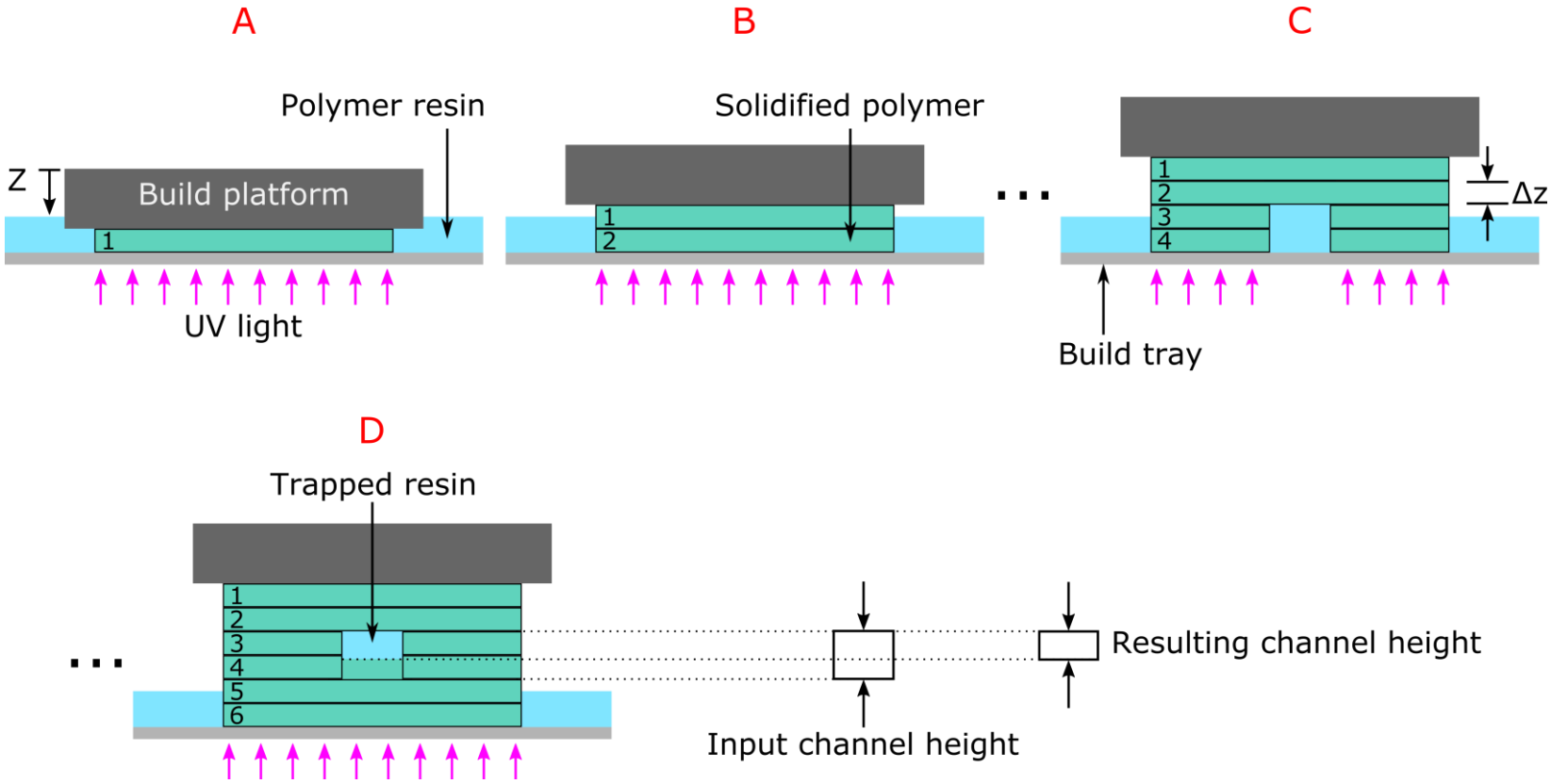

Figure 5.4. Fabrication of a part with an embedded channel via MPμSL. (A) UV light is projected through the build tray during the first step causing solidification of layer 1, this process is repeated for layer 2 in (B). The fabrication of layers 3 and 5 is not shown in the graphic. During fabrication of layer 4 in (C) the UV light is masked by the DMD at the location of the embedded channel. (D) Shows the fabrication of layer 6. The resulting channel height is smaller than the designed input channel height due to overcuring.

5.3.2 Total optical dose for a multi-layered part

In the design space of the model $z = 0$ at the interface of the part being printed and the build platform (Figure 5.4) and the layer thickness is defined by z_l (Δz). The layer number is given by n, where $n \in [0, N-1]$, and N is the total number of layers in the final part. Thus, the optical irradiance received at depth z during the exposure of layer n is given by

$$I_n(z) = I_0 e^{-[(n+1)z_l - z]/h_a} \tag{5.8}$$

where the numerator in the exponential term is the position of the top of the n^{th} layer, $(n+1)z_l$, minus the depth z at which we wish to calculate the irradiance. The optical dose $D_n(z,t)$, for a layer exposure time t_l and the corresponding normalised dose are given by the equations

$$D_n(z, t_l) = t_l I_n(z) = t_l I_0 e^{-[(n+1)z_l - z]/h_a} \tag{5.9}$$

$$\Omega_n(z, t_l) = \frac{t_l}{T_c} e^{-[(n+1)z_l - z]/h_a} = \tau_l e^{-[(n+1) - z/z_l]\zeta_l} \tag{5.10}$$

where the layer thickness is normalised by dividing the layer thickness z_l by the resin characteristic penetration depth h_a (i.e. $\zeta_l = z_l/h_a$). Normalising the depth z by the layer thickness z_l gives a new unitless parameter $\gamma = z/z_l$. Thus, the normalised dose can be rewritten as

$$\Omega_n(\gamma, \tau_l) = \tau_l e^{-[(n+1) - \gamma]\zeta_l} \tag{5.11}$$

where the current depth z must be less than or equal to the top of the current layer, $(n+1)z_l$ (any value of z greater than the top of the current build layer hasn't been fabricated yet). This is defined by the following condition

$$\begin{aligned} &(n+1) - \gamma \geq 0 \\ &\Rightarrow \gamma \leq n+1 \end{aligned} \tag{5.12}$$

therefore

$$\Omega_n(\gamma, \tau_l) = \begin{cases} \tau_l e^{-[(n+1)-\gamma]\zeta_l}, & \text{if } \gamma \leq n+1 \\ 0, & \text{otherwise} \end{cases} \tag{5.13}$$

in other words, the dose received during the exposure of layer n only influences layer n and the previous layers built before it, but not the subsequent layers.

The normalised dose for a layer n at the back ($\gamma = n$) and front ($\gamma = n + 1$) is given by equations (5.14) and (5.15) respectively.

$$\Omega_{back} = \tau_l e^{-\zeta_l} \tag{5.14}$$

$$\Omega_{front} = \tau_l = \Omega_{back} e^{\zeta_l} \tag{5.15}$$

The main condition for the success of a 3D print is that the dose (Ω) received by the layer exceeds the polymerisation threshold of the resin at the back of the layer enabling the layer to adhere to the previous layer. This requirement can be stated in terms of the normalised dose, $\Omega_{back} \geq 1$. The minimum dose required for layer adhesion is given by equation (5.16) and the corresponding minimum dose at the front of the layer is given by equation (5.17) below.

$$\Omega_{back} = 1 \tag{5.16}$$

$$\Omega_{front} = e^{\zeta_l} \tag{5.17}$$

Finally, if we assume exposure is additive for each layer (assumption 1), then the total dose over the entire 3D printed part is given by the sum of the individual layer doses

$$\Omega(\gamma, \tau_l) = \sum_{n=0}^{N-1} \Omega_n(\gamma, \tau_l) \tag{5.18}$$

where Ω_n is given by equation (5.6).

Table 5.3. Multi-layered part - experimental parameters.

Parameter	**Symbol**	**Unit(s)**
Build layer thickness	z_l	μm
Layer number	n	-
Optical irradiance received at depth z during exposure of layer n	$I_n(z)$	W.cm^{-2}
Optical dose received at depth z during exposure of layer n	D_n	J.cm^{-2}
Total number of layers	N	-
Layer exposure time	t_l	s

Table 5.4. Multilayered part - unitless parameters.

Parameter	**Symbol**	**Equation**
Normalised layer thickness	ζ_l	z_l/h_a
Normalised dose received at depth z during exposure of layer n	Ω_n	D_n/D_c
Normalised depth	γ	z/z_l
Normalised layer exposure time	τ_l	t_l/T_c

To demonstrate the nature of equation (5.18), consider the graph of the normalised dose plotted as a function of depth in Figure 5.5. The graph shows the typical polymerisation dose received for a solid block of material consisting of five layers, with layer thickness $z_l = 10$ μm. Parameters are set for the ideal case where the dose received at the back of the layer is just enough for complete polymerisation, such that $\Omega_{back} = 1.0$. The normalised layer thickness ζ_l is set at 0.69 to yield a normalised layer exposure time τ_l of 2.0.

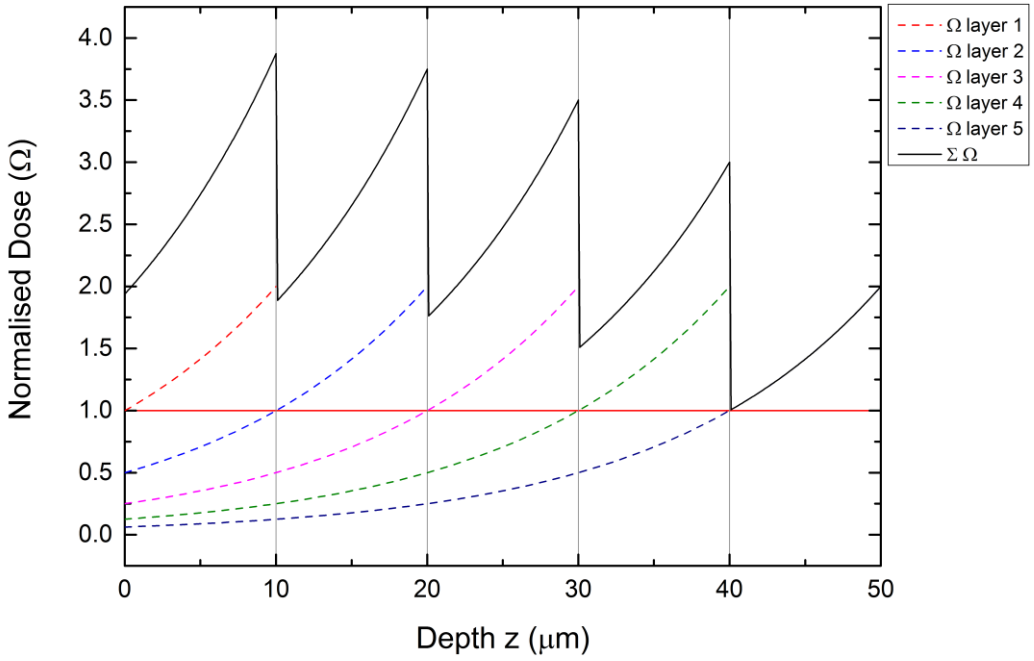

Figure 5.5. Normalised dose (Ω) plotted as a function of depth (z) for a solid polymer block of material consisting of five layers. Individual layer doses for layers 1-5 are shown by the dotted lines. Total polymerisation dose received by the part throughout the build is shown as a solid black line. Vertical grid lines spaced at intervals of 10 μm represent the interface between consecutive layers. $\Omega = 1.0$ is represented by a horizontal red line.

The total energy dose received by the initial photopolymer layer depends on the total number of layers in the part. In fact, because exposure is additive (assumption 1), the total energy dose received by the initial photopolymer layer will be a summation of the energy doses used to fabricate the subsequent layers. This can be seen in Figure 5.5 where the total dose received by layer 1 is noticeably larger than the dose received by layer 5. For example, the total normalised dose at the back of layer 1 is 1.9, whereas the total dose received at the front of layer 1 is 3.9. In comparison, the total dose received at the back and front of layer 5 is 1.0 and 2.0 respectively. This variation in polymerisation dose between the front and back of each layer likely results in a build-up of internal stresses throughout the 3D printed part due to differences in material phase between partly- and fully-polymerised regions[12].

5.3.3 Modelling of an embedded channel

In Figure 5.5 we considered the case of a completely solid part in which every layer receives an exposure. Let us now consider the case where an internal void is present in the 3D printed part. In such a situation, the layer is not exposed at that point in the build. To model this, a new parameter, δ_n, is introduced for each layer *n* such that

$$\delta_n = \begin{cases} 0, & \text{if } n \text{ is in a flow channel} \\ 1, & \text{otherwise} \end{cases} \tag{5.19}$$

The new equation for total normalised dose with an internal void is given by equation (5.20)

$$\Omega(\gamma, \tau_l) = \sum_{n=0}^{N-1} \delta_n \Omega_n \tag{5.20}$$

To illustrate the effect of adding an internal void into the build consider Figure 5.6 which shows a graph of the total normalised dose (Ω) plotted against depth (z) for a 15-layer part with an internal void inserted in layers 6 – 8. The variation of the binary parameter δ_n with layer is shown in green.

δ_n can be considered the ideal polymerisation dose where $\delta_n = 1$ represents material that has received just enough dose to initiate polymerisation and $\delta_n = 0$ represents material that has received no dose. However, this is not an ideal scenario and the polymer trapped inside layers 6 – 8 receives some curing dose during the formation of the enclosing layers 9 – 15. This is enough to partially block the channel such that the input channel dimension differs significantly from the output channel dimension, in this case by 10 μm (33%) or one whole layer. In fact, the dose received by layers 6 and 7 is a significant fraction of the dose required for complete polymerisation ($\Omega = 1.0$).

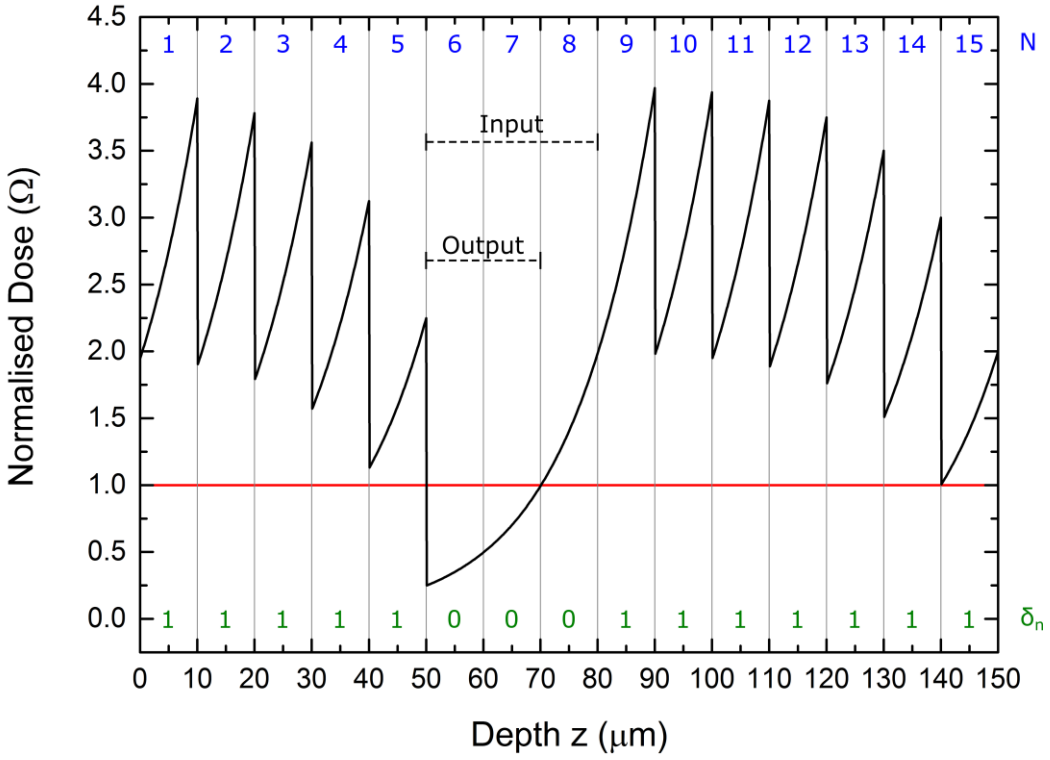

Figure 5.6. Normalised dose (Ω) plotted as a function of depth (z) for a part with an embedded channel with layer thickness z_l = 10 μm, and total number of layers $N = 15$. Total polymerisation dose received by the part throughout the build is shown as a solid black line. Vertical grid lines spaced at intervals of 10 μm represent the interface between consecutive layers. Minimum dose to reach the polymerisation threshold, $\Omega = 1.0$, is represented by a horizontal red line. The variation of the parameter δ_n is represented in green text.

5.3.4 3D model

Equation (5.20) can be expanded to two and three dimensions by evaluating at each x and y coordinate in the design space. In the case of the MPμSL technique, the x and y coordinates correspond to DMD pixels in the build plane. Thus equation (5.20) is evaluated at each x and y pixel coordinate throughout the entire z depth of the part from the first layer ($n = 0$) to the final layer ($n = N - 1$). Values are stored in a 3D array representing the total build extents. A 2D cross-section of the 3D normalised dose array for a simulated 3D printed part with an embedded channel is shown in Figure 5.7.

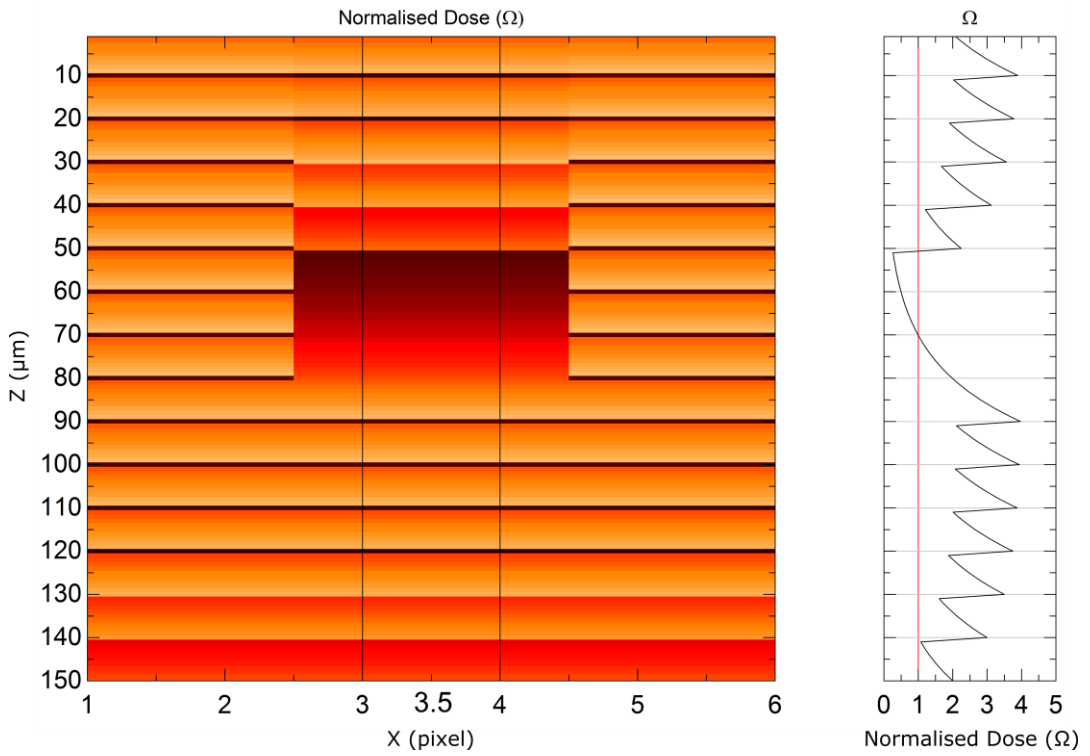

Figure 5.7. A 2D cross section of the normalised dose (Ω) matrix for a simulated part with an embedded channel with 1D intensity outset. Slice thickness $z_l = 10$ μm, and total number of layers $N = 15$. The embedded channel is located at layers 6, 7 and 8.

The simulated 3D array of Ω values can be simplified by defining a set polymerisation threshold; defined by $\Omega > 1$ in the current work. From this condition, it is possible to divide the 3D dose array into solidified and unsolidified parts represented by binary ones and zeros. This concept is illustrated in Figure 5.8 (B) which shows the simulated result from Figure 5.7 represented in binary format. The difference between the designed input array (Figure 5.8 (A)) and the simulated result (Figure 5.8 (B)) is calculated using a Boolean XOR operation.

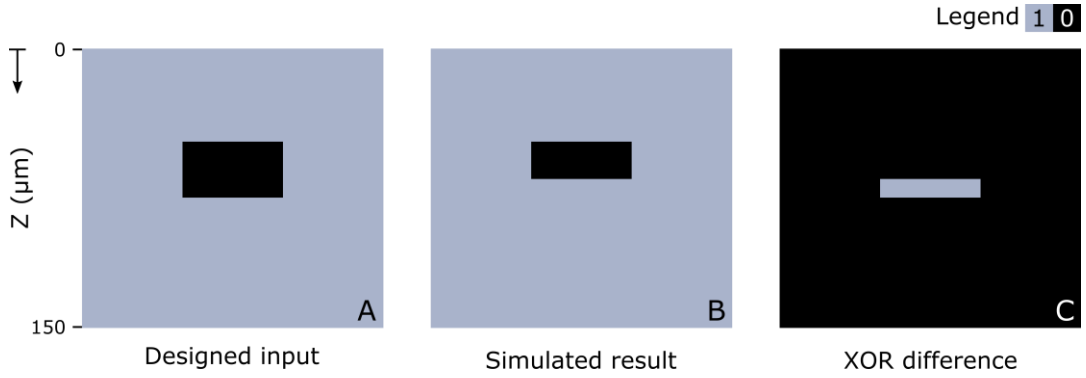

Figure 5.8. Binary array representation of the (A) the designed input, (B) the simulated result, and (C) the difference between (A) and (B) calculated using a Boolean XOR operation. The black arrow shows the build direction.

5.4 Predictive design algorithm

Using the designed input channel dimension as the end condition, an iterative design algorithm is developed based on the mathematical model in the previous section. Equation (5.20) forms the basis of the predictive model which is evaluated at each step in the algorithm to predict the output channel height. An iterative approach is then taken to converge toward a solution for input channel height that will result in the desired output with the overcuring effect taken into consideration. Implementation of the predictive design algorithm is realised using LabVIEW™ 2016 64-bit (National Instruments, TX, USA).

5.4.1 CAD design and slicing

A 3D model of the embedded channel is designed using SolidWorks™ 2016 (Dassault Systèmes SolidWorks Corp., MA, USA) and output as a STL file. This model is then imported into Composer software (Asiga, CA, USA) for orientation on the build platform and slicing based on the slice thickness settings of the Asiga 3D printer (10 – 150 µm). After the model has been processed and sent to the 3D printer the individual slice files can be downloaded from the 3D printer web interface as a ".zip" folder containing a stack of binary (black and white) image files in Portable Network Graphics (PNG) format. An example of a binary slice file is shown in Figure 5.9.

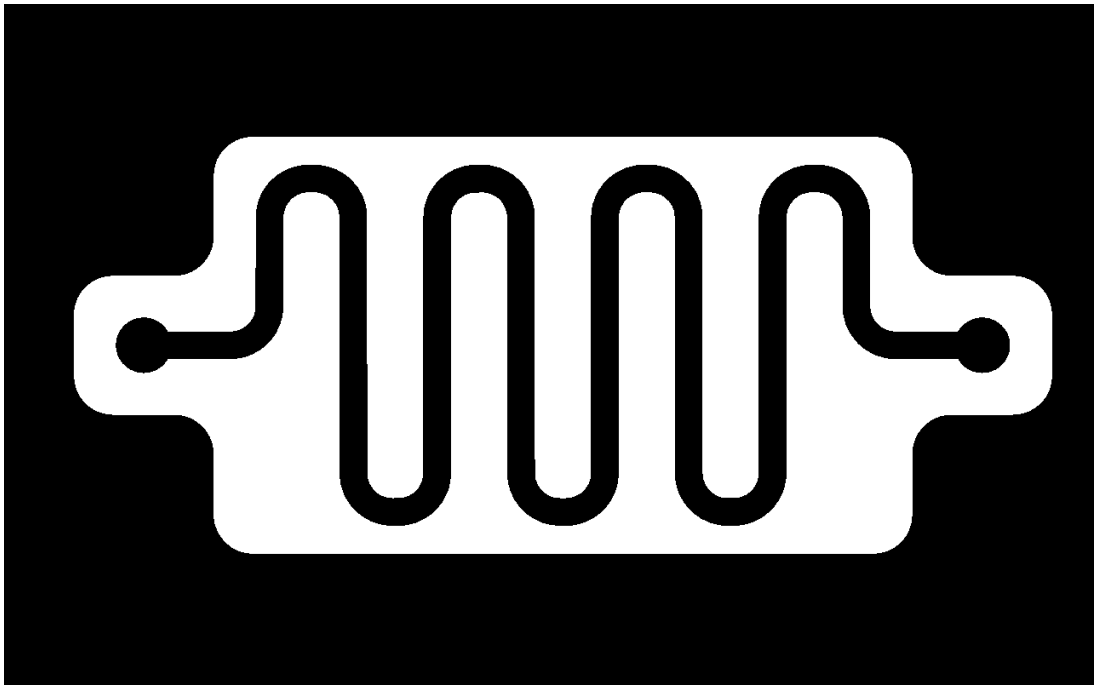

Figure 5.9. Example of a binary slice file downloaded from the Asiga 3D printer web interface. Slice files are sent in sequence to the DMD projector which masks or reflects the UV curing light based on the binary image pattern.

5.4.2 Generation of δ array

The PNG image stack downloaded from the Asiga printer web interface is then converted into a binary 3D voxel array with *x* and *y* array dimensions corresponding to the number of pixels in each PNG slice image (1280 × 800 pixels respectively). The Z array dimension varies based on the slice thickness and overall size of the designed part. This 3D voxel array becomes the initial set of values for the parameter δ in equation (5.20) such that individual values of δ can be queried using the array index (i.e. $\delta_{1,2,3}$ returns the δ value at the point $x = 1, y = 2, z = 3$ in the array).

Due to the large size of the voxel array it is necessary to split the array into subsections containing regions of interest (ROI) to reduce simulation time. ROIs are extracted from the array before execution of the code.

5.4.3 Implementation of the predictive design algorithm

The design algorithm is implemented using an iterative approach. First, the ideal solution θ_{ideal} is defined based on the input voxel array, δ_{in}.

$$\theta_{ideal} = \delta_{in} \tag{5.21}$$

Equation (5.20) is calculated for each *x* and *y* voxel in the array summing the dose received over the entire *z*-direction during the fabrication of each layer from $n = 0$ to $N - 1$. This results in a 3D voxel array of single-precision floating point numeric values for Ω, the normalised dose. This array, Ω_{sim}, represents the simulated dose received by each voxel during the build. A polymerisation threshold is applied to the simulated dose array based on the assumption that values of $\Omega_{sim} > 1.0$ represent a fully polymerised material, and values of $\Omega_{sim} < 1.0$ represent unpolymerized liquid resin (assumption 3).

A 3D Boolean array, θ_{real}, is generated from this threshold, with values of 1 representing fully solid material and values of zero representing unsolidified material.

$$\theta_{real} = \begin{cases} 0, & \text{unsolidified} \\ 1, & \text{solidified} \end{cases} \tag{5.22}$$

This simulated voxel array (the numerical solution) becomes the basis for calculation of the modified input voxel array δ_{mod}. First, the difference between the numerical solution and the ideal solution is calculated.

$$\phi = \theta_{real} - \theta_{ideal} \tag{5.23}$$

Subtraction of the two numeric Boolean arrays (0, 1) results in the 3D difference array, ϕ. Note that the subtraction function is set to 'saturate' resulting in the following three scenarios;

a) $1 - 1 = 0$
b) $1 - 0 = 1$
c) $0 - 1 = 0$

(a) and (b) are the standard mathematical protocol, however (c) represents the case of saturation which is essential to convergence of the model. Figure 5.10 shows a 2D cross sectional image in the *x*/z plane of the three arrays for the two cases.

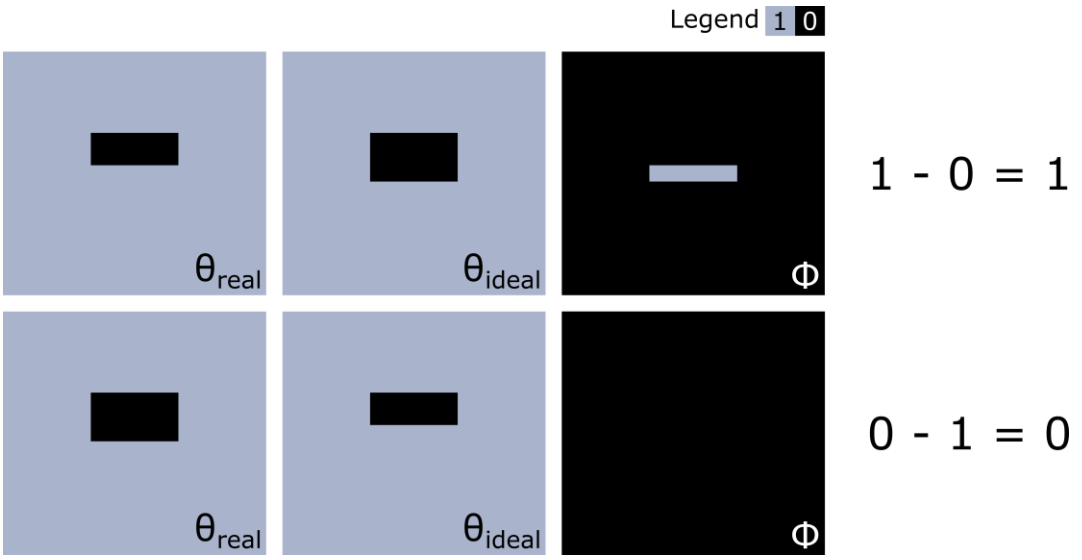

Figure 5.10. A 2D cross section (in the *x*/z plane) of three voxel arrays θ_{real}, θ_{ideal}, and ϕ illustrating the case of arithmetic saturation which is essential to convergence of the 3D model.

To converge on a solution where the simulated output θ_{real} is close to the ideal input, the input channel must be made larger in the *z*-direction. The increase in channel size in the *z*-direction is a function of the material characteristics h_a, and T_c, and the number of enclosing layers λ. To widen the input channel the difference array, ϕ, is shifted by one pixel in the *z*-direction to yield $\phi_{\downarrow}$, and then subtracted from the input array, θ_{ideal}, to calculate the new modified input voxel array δ_{mod}.

$$\delta_{mod} = \theta_{ideal} - \phi_{\downarrow} \tag{5.24}$$

Subtraction of these two Boolean arrays is performed using the saturation mode mentioned previously.

New values for Ω_{sim} and θ_{real} are calculated based on δ_{mod} using equation (5.20) and the process is repeated. In the current work, an end condition for the algorithm was chosen based on an upper iteration limit i_{max}. Table 5.5 shows a summary of the terms used in the algorithm. A schematic of the predictive algorithm is shown in Figure 5.11.

Table 5.5. Design algorithm inputs.

Parameter	**Symbol**	**Unit(s)**
Input voxel array	δ_{in}	-
Modified voxel array	δ_{mod}	-
Simulated normalised dose array	Ω_{sim}	-
Ideal solution	θ_{ideal}	-
Numerical solution	θ_{real}	-
Difference between ideal and numerical solutions	ϕ	-
Shifted difference array	$\phi_{\downarrow}$	-
Pixel depth	p_x	µm
Pixel width	p_y	µm
Layer thickness	z_l	µm
Layer exposure time	t_l	s
Polymerisation threshold	Ω	-
Maximum number of iterations	i_{max}	-
Voxel z-shift	Z_{shift}	-
Relative error limit	E_{rel}	%

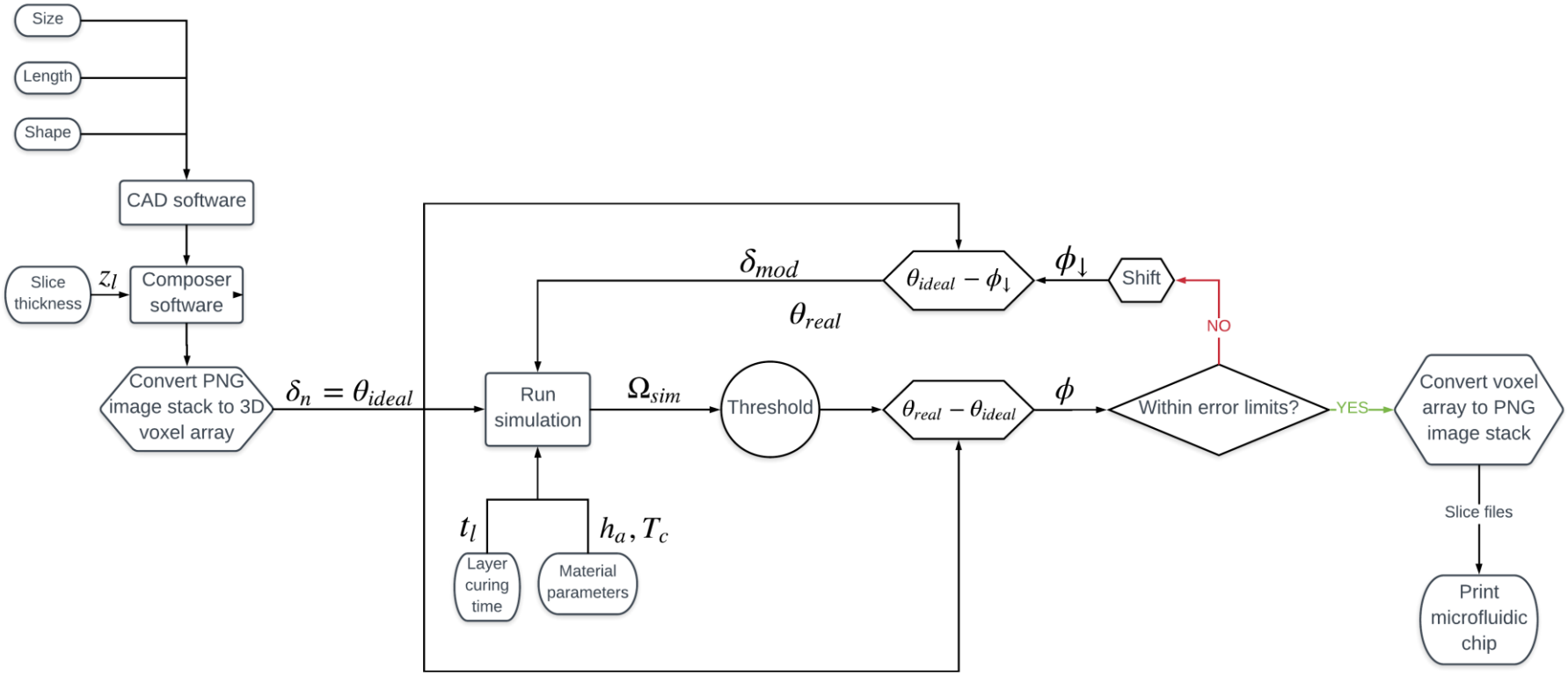

Figure 5.11. Flow chart of the design algorithm for mitigation of the overcuring effect in MPμSL.

5.5 Results and Discussion

Validation of the current model was carried out using a model of a circular microfluidic channel 540 µm diameter with three levels of enclosing layers $\lambda = 50, 25 \text{ and } 10$ and at a slice thickness $z_l = 25$ µm. The number of enclosing layers, λ, is measured from the bottom of the microfluidic channel to the bottom of the part; for a circular channel, a second parameter, λ_c, is defined as the distance from the middle of the microfluidic channel to the bottom of the part. This concept is outlined in Figure 5.12 showing paired values for both λ and λ_c.

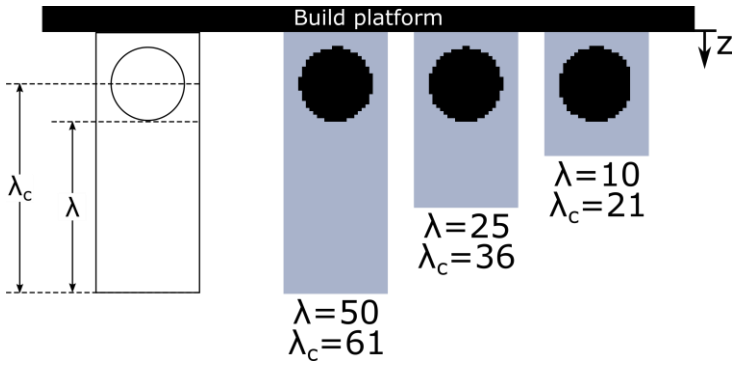

Figure 5.12. The model parameters λ and λ_c, number of enclosing layers. λ is measured from the bottom of the channel, while λ_c is measured from the middle of the channel.

Model inputs h_a and T_c were chosen based on a photopolymer material, Formlabs Clear, with values of 246.274 µm and 0.9482 s respectively. Further information on determination of photopolymer material properties is given in section 6.2.4.

The evolution of the binary arrays δ_{mod}, θ_{real}, ϕ, and $\phi_{\downarrow}$ in the application of the design algorithm toward the production of the circular microfluidic channel is shown in Figure 5.13, Figure 5.14, and Figure 5.15 for $\lambda = 50, 25, \text{and } 10$ layers respectively. It should be noted that i_{max} was set to $N = 50$ iterations for each model, however only iterations up until convergence of the model are displayed. For iterations $n > 25, 22 \text{ and } 14$ respectively the model has fully converged ($\phi = 0$) and there is no change in any of the output arrays.

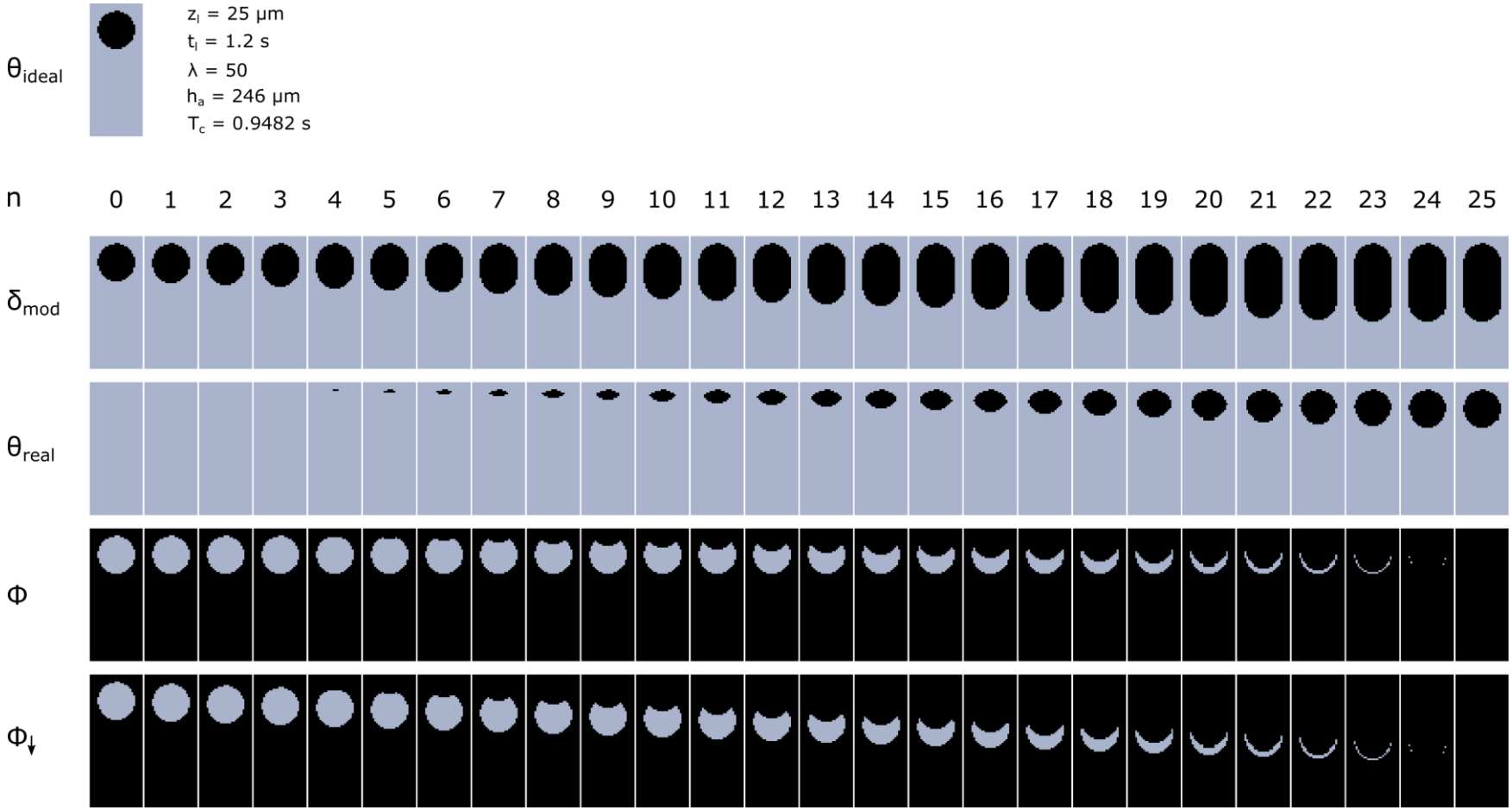

Figure 5.13. Evolution of the binary arrays δ_{mod}, θ_{real}, ϕ, and $\phi_{\downarrow}$ in the application of the design algorithm toward the production of a circular microfluidic channel with number of enclosing layers $\lambda = 50$.

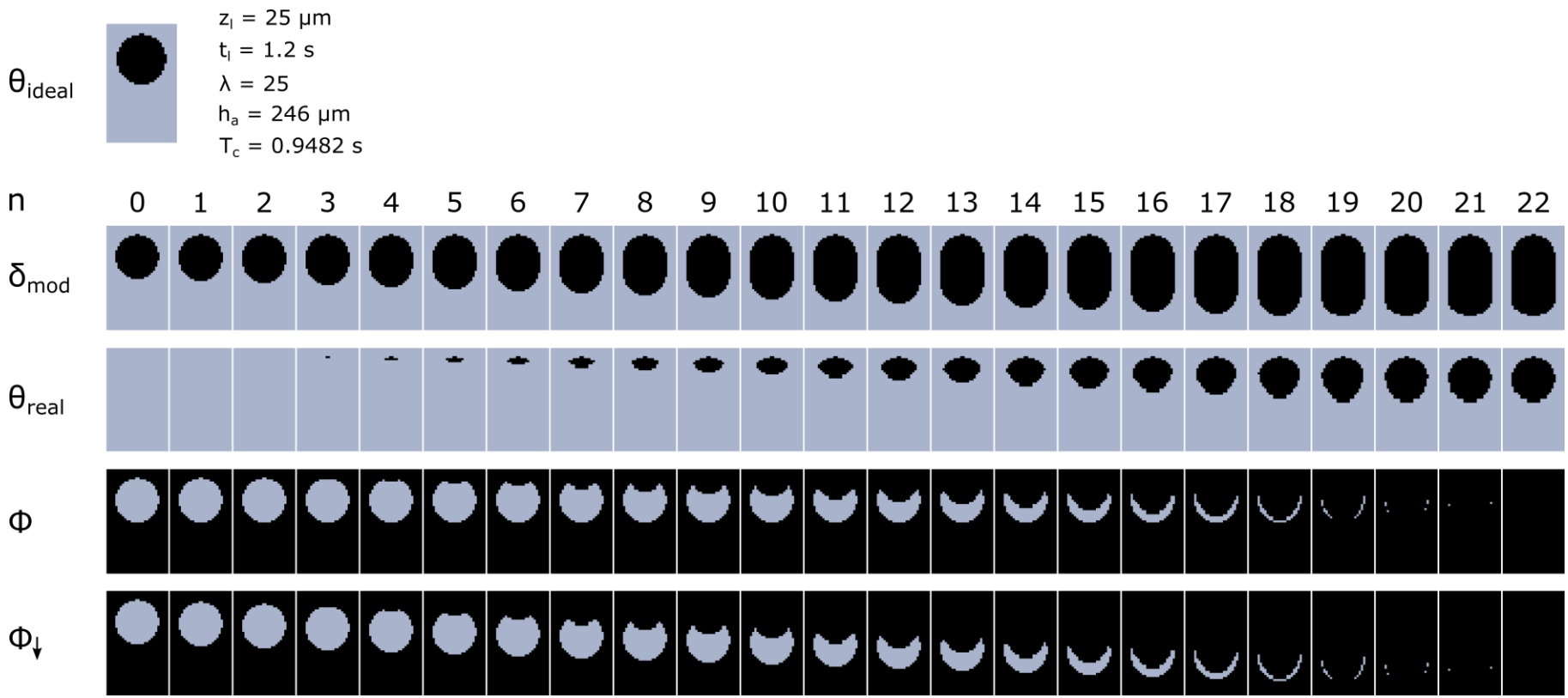

Figure 5.14. Evolution of the binary arrays δ_{mod}, θ_{real}, ϕ, and $\phi_{\downarrow}$ in the application of the design algorithm toward the production of a circular microfluidic channel with number of enclosing layers $\lambda = 25$.

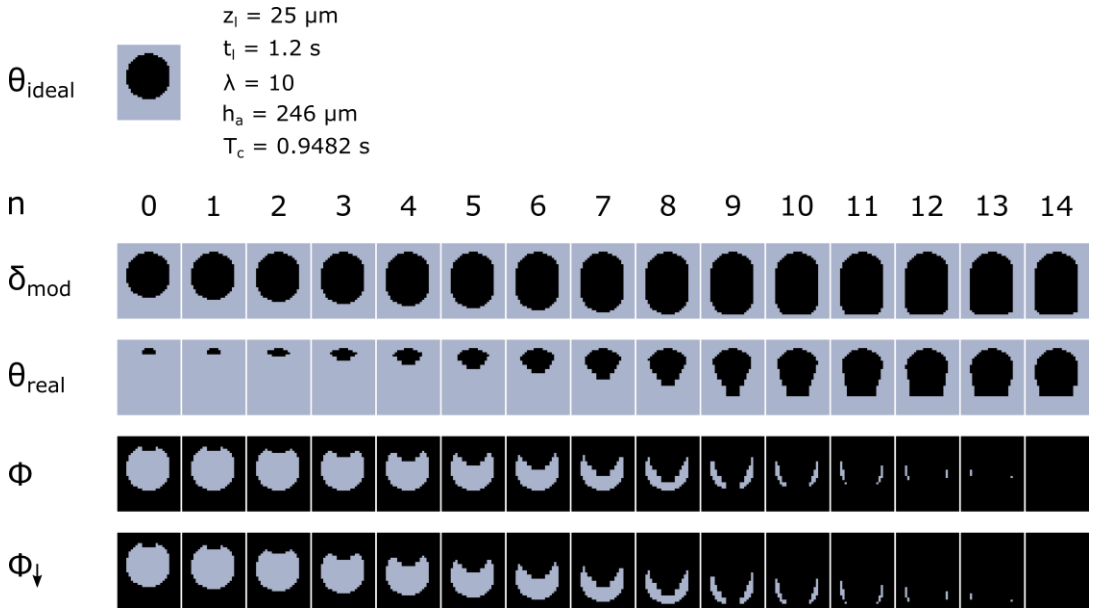

Figure 5.15. Evolution of the binary arrays δ_{mod}, θ_{real}, ϕ, and $\phi_{\downarrow}$ in the application of the design algorithm toward the production of a circular microfluidic channel with number of enclosing layers $\lambda = 10$.

Convergence of the theoretical model depends on the interrelationship between the material characteristics and experimental parameters. For successful mitigation of the overcuring effect using the current model, the total thickness of the enclosing layers (λz_l) above the void must be greater than the polymerisation thickness for a single layer,

$$\lambda z_l \geq z_p \tag{5.25}$$

where z_l is the layer slice thickness, and z_p is the resulting thickness of the polymerised layer given by equation (5.4) for layer exposure time, t_l, and material characteristics h_a and T_c. This is one of the main findings of this study as it suggests that channels smaller than the current limit of ~3.5-5.5h_a imposed by Gong et al.[12] are possible using this new technique.

Another important characteristic of the model is the effect of the number of enclosing layers on the ability to finely tune the channel shape. This means that a larger number of enclosing layers above the channel results in finer control over the resulting channel shape, as resin absorption increases exponentially with thickness. For materials with

large h_a it becomes increasingly difficult to mitigate for overcuring when dealing with a small number of enclosing layers. However, by increasing the number of enclosing layers mitigation can be achieved even for low resolution resins with large h_a. This can be seen when comparing Figure 5.13 for a channel with 50 enclosing layers ($\lambda = 50$) with Figure 5.15 for a channel with 10 enclosing layers ($\lambda = 10$).

In the case of $\lambda = 50$, the final simulated result (θ_{real} at $n = 25$) is a very close approximation to the ideal solution (θ_{ideal}) with circular channel walls at the top and bottom of the channel. On the other hand, in the case of $\lambda = 10$, the final simulated result (θ_{real} at $n = 14$) shows the bottom channel wall (the side closest to the light source) as completely flat.

Figure 5.16 shows a graph of total difference (in voxels) between the ideal solution (θ_{ideal}) and the real solution (θ_{real}) calculated using the XOR Boolean operator. This clearly illustrates that a higher number of enclosing layers results in greater control over output channel resolution with the final difference in voxel count between the ideal and real solutions approaching zero as λ increases. The final minimum voxel error for the three cases presented is shown in Table 5.6.

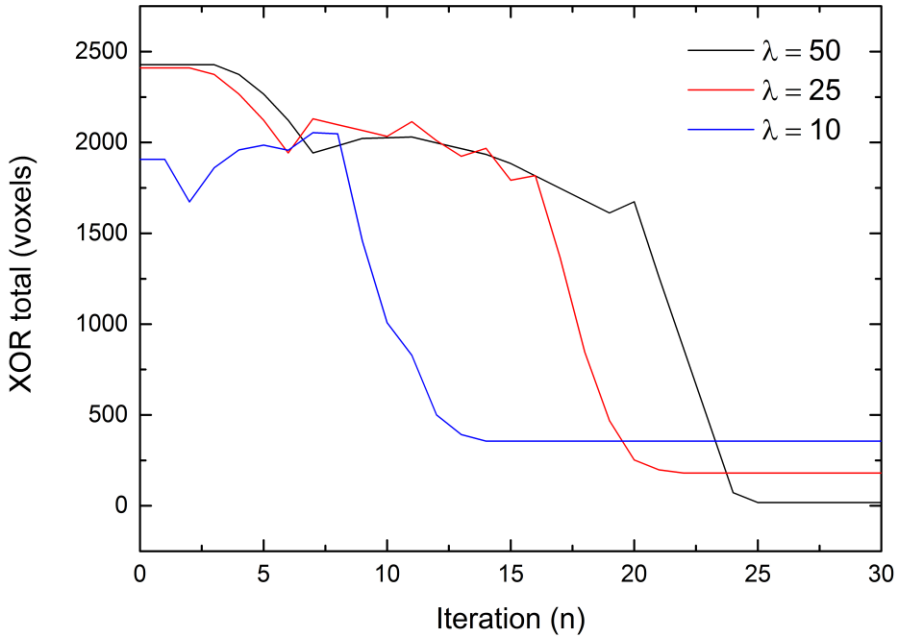

Figure 5.16. Convergence of the design model to an optimum solution. The graph shows the total difference in voxels between the ideal solution (θ_{ideal}) and the simulated result (θ_{real}) for the circular microfluidic channels presented in Figure 5.13, Figure 5.14 and Figure 5.15. The total difference between the ideal and real arrays converges for the three cases of $\lambda = 10, 25$ and 50 layers.

Table 5.6. Percentage relative error (E_{rel}) for the three cases presented in Figure 5.15, Figure 5.14, and Figure 5.13 for channels with enclosing layers $\lambda = 10, 25,$ and 50 respectively.

$\boldsymbol{\lambda}$	$\boldsymbol{\lambda_c}$	**Iterations to convergence** $(\boldsymbol{n = N - 1})$	$\boldsymbol{E_{rel}}$ **(%)**
10	**61**	14	14.66
25	**36**	22	7.47
50	**21**	25	0.94

As expected, relative error, E_{rel}, and number of enclosing layers (λ and λ_c) are inversely related. It is also worth noting that the number of iterations to convergence, n, is strongly dependant on the number of enclosing layers, with larger numbers of enclosing layers resulting in longer time to convergence but with lower final error.

5.6 Conclusions

The MPμSL 3D printing method is one of the best suited 3D printing methods for the production of microfluidic channels. However, the production of high resolution internal voids represents a major challenge due to the overcuring effect. Two main approaches to tackling the problem of SL overcure are presented in the literature. These include: altering base resin material characteristics to reduce cure depth by doping with a light absorber[12,13]; and improving MPμSL depth resolution via improvements in equipment[123].

A third approach has previously been investigated by Limaye and Rosen[137,138] toward improving resolution of the MPμSL technique by introducing a "compensation zone" that is computed via modelling and then subtracted from the CAD model prior to fabrication to compensate for the so called print-through errors. This model could, in theory, eliminate external print-through errors completely, resulting in part geometries that closely correspond to the input model geometry. However, this model only applies to external features and does not take into account the fabrication of internal voids.

In this chapter, a new design algorithm was developed for mitigation of the overcuring effect toward the production of high resolution microfluidic channels. This new algorithm is based on the threshold model for resin curing which is evaluated at each node in a 3D voxel array. Modification of the initial voxel array is then performed using an iterative design-and-test approach to reduce or eliminate overcure and improve geometric resolution throughout the part.

Convergence of the model depends on the number of enclosing layers (λ) above the void being greater than the polymerisation depth (z_p) for the given layer polymerisation time. Whereas previously an increase in the number of enclosing layers above a channel lead to an increase in the level of overcuring and a reduction in resolution, through the application of the new algorithm an increase in the number of enclosing layers leads to increased control over dimensional accuracy. Finally, the new model suggests that it is possible to produce internal channels smaller than the limit imposed by the photopolymer material characteristics h_a and T_c.

Chapter 6
Model verification

6.1 Introduction

In this chapter, the design algorithm developed in Chapter 5 is experimentally evaluated using a 3D printer based on the MPμSL VP technique (Pico +27, Asiga, CA, USA) using three commercially available photopolymer materials. Photopolymer material characteristics including resin characteristic penetration depth (h_a) and critical time (T_c) are evaluated for the three materials using the windowpane test. These characteristic material parameters form the basis of the predictive design model.

CAD software was used to design microfluidic channels with square and circular geometries at three settings for layer slice thickness (z_l). In addition, the number of enclosing layers (λ) used to encapsulate the microfluidic channels was varied between 10, 25, and 50 layers for both geometries. The 3D channel designs were oriented on the printer build platform using Asiga Composer printer software and sliced according to layer thickness (z_l). The resulting binary PNG image stacks were converted to 3D voxel arrays and input to the iterative design algorithm. Maximum number of iterations (i_{max}) for the design model was set based on results from initial channel simulations. Modified and unmodified voxel models were then sliced and fabricated at the corresponding settings and the resulting channel heights and shapes were compared.

Results demonstrate the capability of the new design algorithm to mitigate for the overcuring effect, providing increased channel resolution and repeatability of the technique. In addition, the minimum achievable resolution is no longer limited by the resin material characteristic penetration depth h_a. The current model sets a new minimum limit tied to the number of enclosing layers (λ), with an increase in the number of enclosing layers resulting in greater control over the final channel shape. This is a vast improvement on the previous technique whereby an increase in λ resulted in poor quality blocked channels.

6.2 Materials and methods

6.2.1 3D printer

A DLP 3D printer (Pico+27, Asiga, CA, USA) based on the MPμSL VP technique was used to fabricate microfluidic devices with defined channel height and shape. The Asiga Pico+27 operates at a wavelength of 405 nm and has a reported resolution of 27 μm in the build plane in *x* and *y* directions and a variable vertical *z*-resolution of 10 – 150 μm. *X*-*Y* resolution is based on the size of a single micromirror in the DMD micromirror array thus representing the base width and depth of a single voxel, with the variable slice thickness in the *z*-direction representing the voxel height. The DMD is a Texas Instruments DLP 4500 module (Austin, TX, USA), with a 912×1140 micromirror array arranged in a diamond pixel orientation[12]. In order to ensure alignment with DMD pixels, all test parts are rotated 45° on the build plane as shown in Figure 6.1.

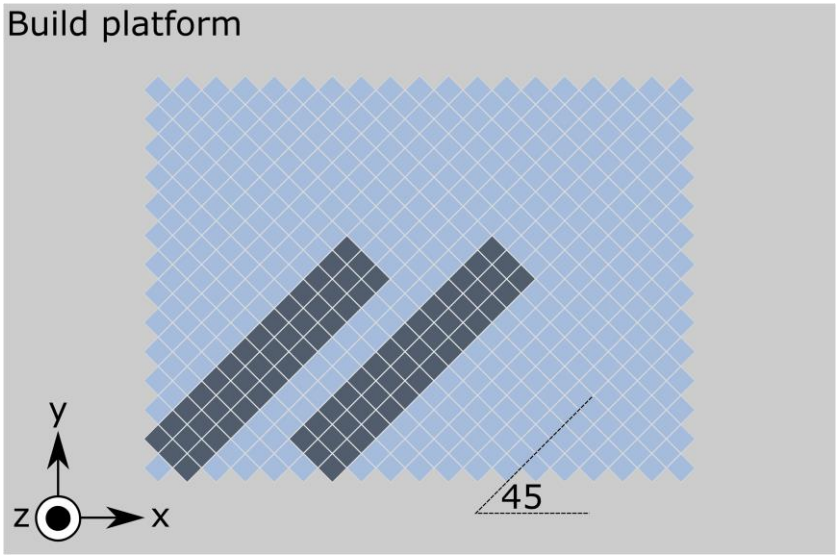

Figure 6.1. The orientation of the Asiga Pico+27 DMD pixels with respect to the X axis, adapted from Gong et al.[12].

DMD pixel alignment was experimentally verified by curing single ($1 \times 1\ mm^2$) layers of photopolymer material at angles (0 - 90°) on to a glass slide and imaging using a VHX 2000 (Keyence, Osaka, Japan) and a Contour GT white light interferometer (Bruker, MA, USA), results are shown in Figure 6.2.

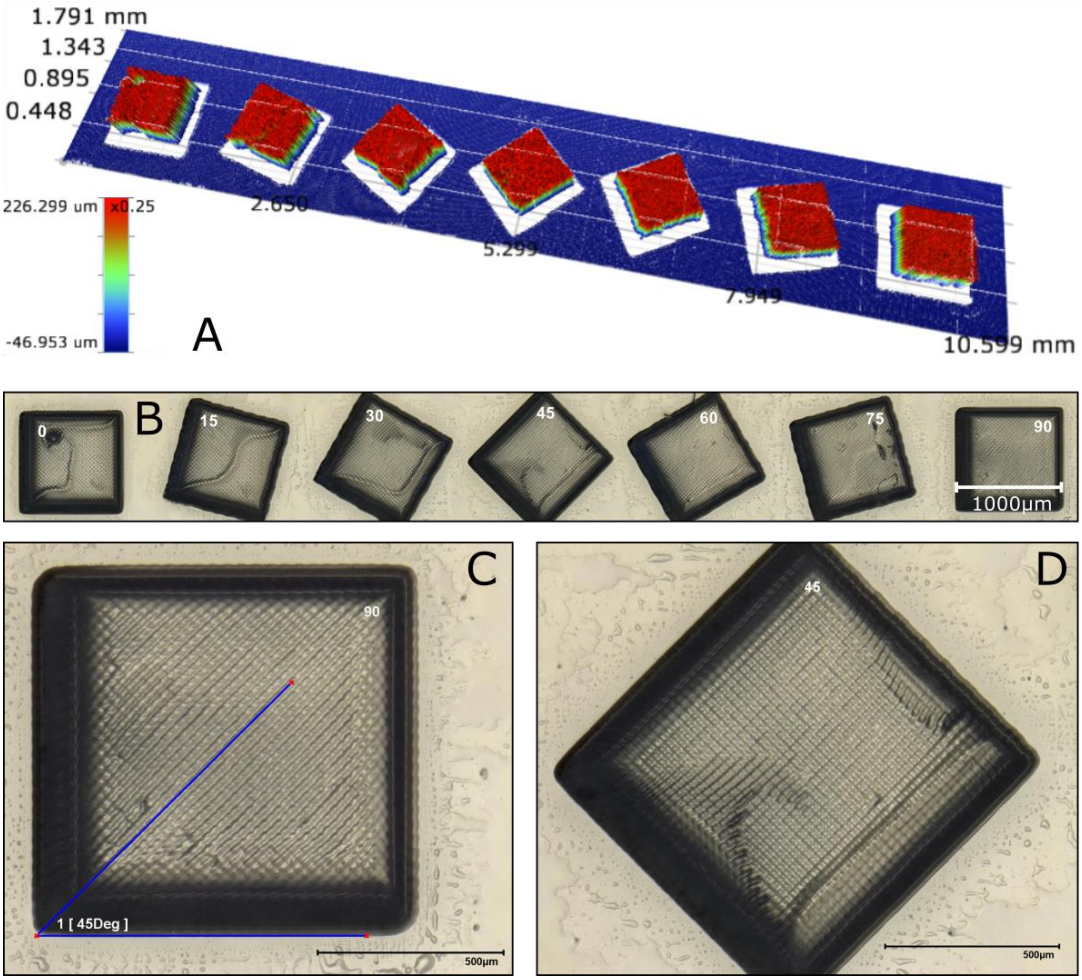

Figure 6.2. Characterisation of DMD pixel angle on the Asiga Pico+27 3D printer. Image (A) is a 3D profile of the part used for angle characterisation, (B) shows a 2D microscope image of the same part with angles superimposed. Image (C) shows a single layer of material (1 x 1 mm) with edges aligned with X and Y axes of the build platform, lines of DMD pixels are clearly visible and are oriented at 45° w.r.t the bottom edge of the part. In image (D) the edges of the material are oriented at 45° w.r.t the X and Y axes. Image (A) was taken using a Brucker Contour GT white light interferometer while images (B-D) were taken using a Keyence VHX 2000 digital microscope.

6.2.2 Materials

PlasClear (Asiga, Anaheim Hills, CA, USA), Formlabs Clear resin (Formlabs Inc., Somerville, MA, USA), and Freeprint Mould Clear 405 nm (DETAX GmbH, Germany) photopolymer resins were used for microchannel production via the MPμSL technique. PlasClear v 2.0, is an inexpensive photopolymer resin produced by Asiga for their range of MPμSL 3D printers. Similarly, Formlabs Clear is a low viscosity inexpensive 3D printing resin produced by Formlabs for their range of SL 3D printers. Such low viscosity SL resins are compatible with the MPμSL technique which requires a lower viscosity working material to aid in resin replenishment during the build process. Freeprint mould clear is a high-end, biocompatible (class IIa) photopolymer resin used for audiology and dental applications including ear moulds and dental surgical guides. It has the lowest viscosity of the three resins at 622 cP (mPa.s). Resin viscosities for common commercially available photopolymer resins are shown in Table 6.1 below.

Table 6.1. Common photopolymer resin viscosities, adapted from ref.[159] and Appendix B.

Resin	**Viscosity (cP) at 20°C**
Spot GP	63
MadeSolid Firecast	65
Makerjuice G+	79
25-75 Exo10-TPGDA	81
PR48 IC	165
Makerjuice SF	206
DWS DC500	275
Full Spectrum Laser Iron oxide – low viscosity	276
PR48	286
Form Castable	335
MadeSolid Black	336
MadeSolid Vortex	361
DWS DC550	378
DETAX Freeprint Mould*	**622**
Full Spectrum Laser Blue Casting	658
Full Spectrum Laser Casting Red	690
Form Black	876
FormLabs Clear**	**800-900**
Asiga Pink	1082
Asiga PlasClear	**1262**
Full Spectrum Laser Blue Red oxide	1573

*viscosity for Freeprint Mould was measured at 23°C

**viscosity for FormLabs Clear was measured at 25°C[160]

6.2.3 Resin optical absorbance

Before characterisation, the photopolymer resin was mixed into a solution of IPA in ratios from 1:2 to 1:10000. A ratio of 1:100 resin to IPA (1% $^{v}/_{v}$) was found to give optimum peak resolution for the current setup. Liquid resin was decanted into 1.5 ml 10 mm path length UV cuvettes (Brandtech Scientific Inc., Essex, UK) and resin absorbance measurements were made using a Biochrom Libra S22 UV-Vis spectrometer (Biochrom Ltd., Cambridge, UK). No photopolymerisation of the resin material was observed before or after measurement. The Asiga 3D printer UV LED spectrum was measured using an Ocean Optics Maya spectrometer with fibre optic connection (Ocean Optics, FL, USA). Equation (6.1) was applied to give the normalised source spectrum with respect to light

$$\text{Normalised source spectrum} = \log_{10}\left(\frac{I}{I_0}\right) \tag{6.1}$$

where I is the source LED intensity and I_0 is the ambient light intensity measured while the LED is powered off. Results are shown in Figure 6.3.

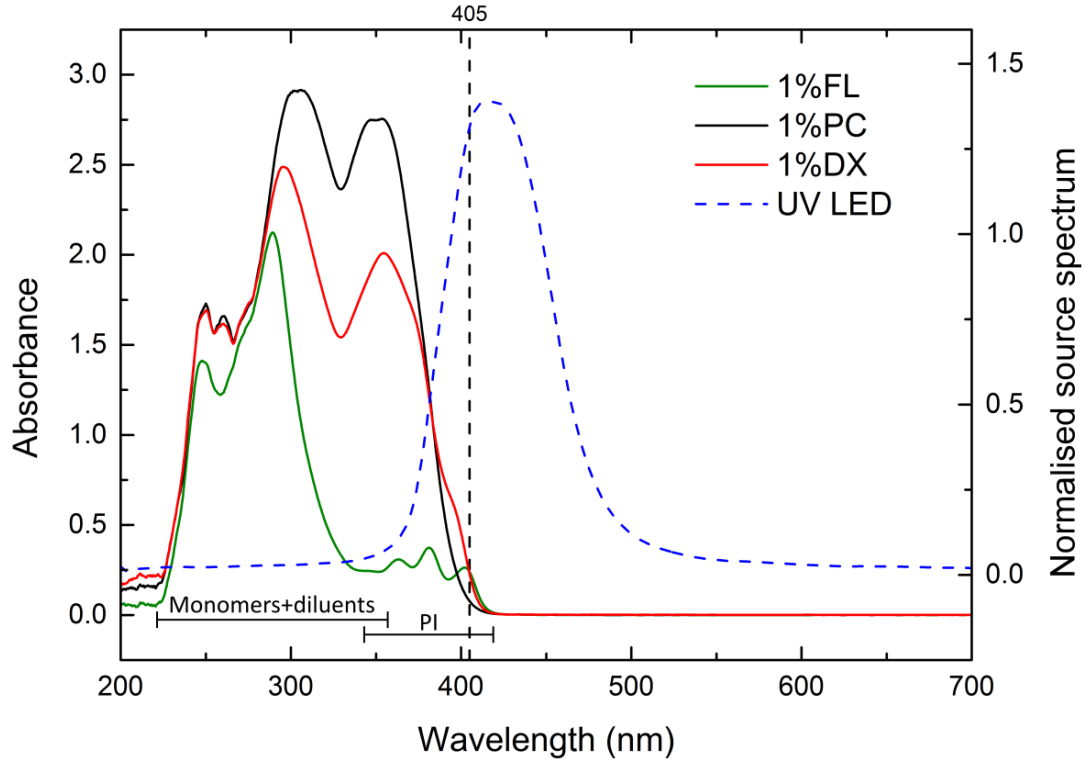

Figure 6.3. Resin optical absorbance for three resins, Formlabs Clear (FL), Asiga PlasClear v2 (PC), and DETAX Freeprint Mould (DX) with an overlay of the Asiga 3D printer UV LED spectrum. Peak ranges for monomers and reactive diluents, and photoinitiator (PI) resin components are outlined in the graph.

The Asiga UV-LED has a Full Width Half Maximum (FWHM) of 68 nm and a peak value of 422 nm. This overlaps the absorption spectrum of the photoinitiator at the tail end of the resin spectra as outlined in the graph, which is the basic requirement for photopolymerisation.

6.2.4 Measurement of experimental constants

Polymerisation thickness as a function of optical dose was measured using the setup in Figure 6.4, which consists of a custom quartz slide holder through which UV light from the 3D printer optics was projected. The Asiga Pico +27 was temporarily modified to accommodate the experiment; the build platform and resin tray were removed and the slider was disabled. A layer of resin ~1mm thick was applied to the glass slide and exposed to a series of rectangular patterns with different exposure times ranging from 0.7 to 20 seconds. After exposure, the slide was rinsed in IPA to remove unpolymerised resin and the thickness of the polymerised regions was measured using

a Brucker Contour GT white light interferometer (Brucker, Massachusetts, USA). Results are shown in Figure 6.5, and Figure 6.6.

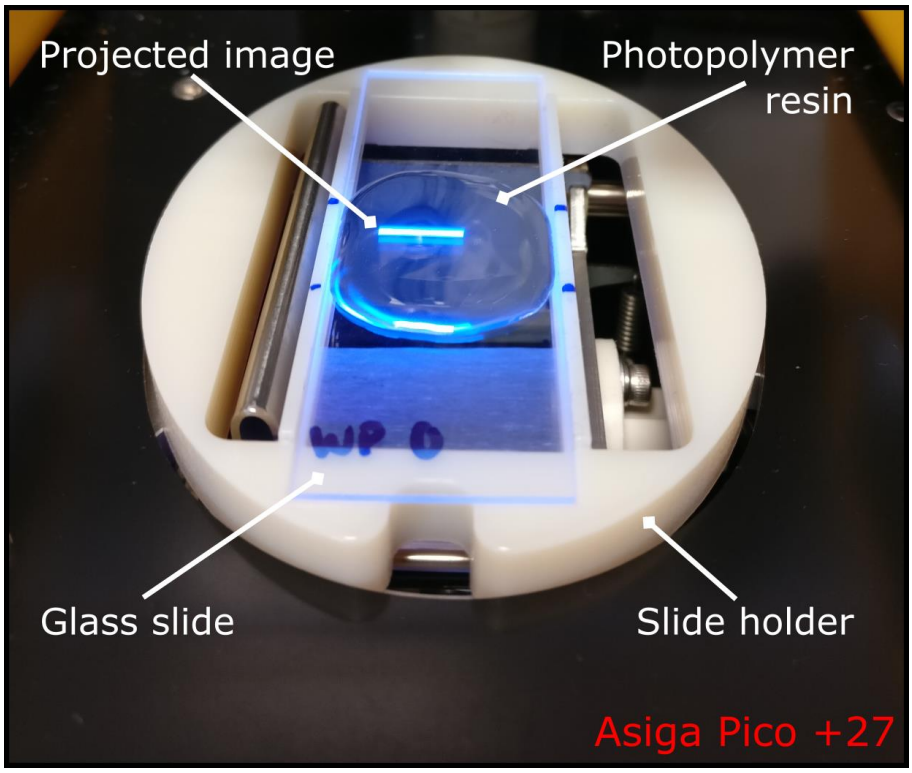

Figure 6.4. Generation of the photopolymer working curve using the Asiga Pico +27 3D printer. The slide holder holds the quartz slide in place while UV light is projected into the resin volume for a defined exposure time setting. Exposure time is increased after each experiment to produce a set of polymer membranes with increasing thickness.

Figure 6.5 shows a 3D height profile of a glass slide with 1x1 mm polymer membranes with each membrane corresponding to a specific exposure time. Membrane thicknesses were averaged over each membrane region using the 'multiple region' option in the Brucker Vision 64 software to calculate error bars and results were plotted to obtain a working curve for each resin material. The working curve for Formlabs Clear resin is shown in Figure 6.6.

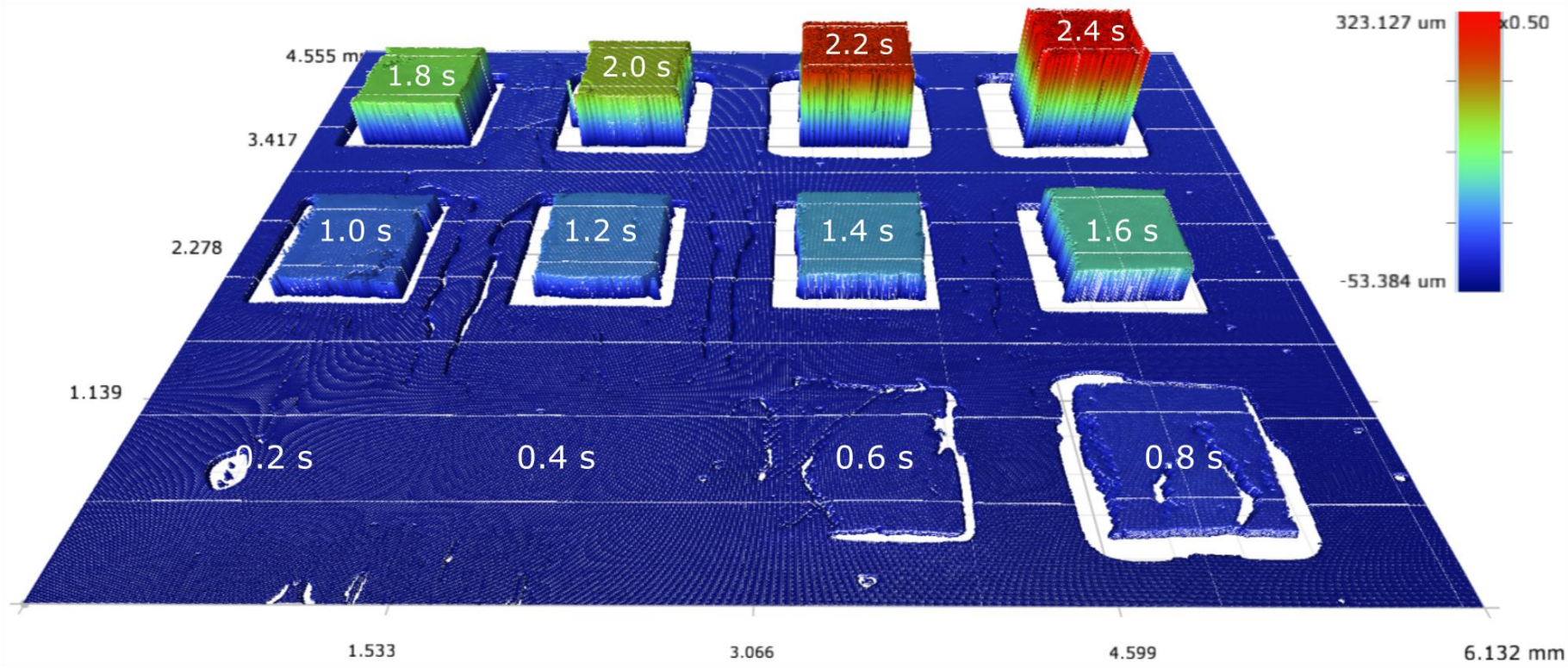

Figure 6.5. Measurement of photopolymer material constants h_a and T_c using the windowpane method. Liquid photopolymer was exposed to squares of UV light (1 mm x 1 mm) for increasing curing time periods. This image shows exposure times from 0.2 to 2.4 s for Formlabs Clear photopolymer resin. Membrane thickness was averaged over the entire membrane area using the 'multiple region' measurement option in the Brucker Vision 64 software to choose the ROI.

Figure 6.6 shows the working curve results for Formlabs Clear resin. As expected, an increase in exposure time leads to a corresponding increase in membrane thickness such that a logarithmic relationship is observed as shown on the semi-log plot of exposure time versus cure depth. The material constants h_a and T_c were determined via a least squares linear curve fit of equation (6.2) to the curve of the natural logarithm of the cure depth versus exposure time for the 405 nm UV-LED source at a constant intensity of 25 mW/cm^2. The characteristic penetration depth, h_a, is the slope of the fitted line whereas resin critical time, T_c, is the line's intercept with the x-axis as outlined in Figure 6.6.

$$z_p = h_a \ln \frac{t_p}{T_c} \tag{6.2}$$

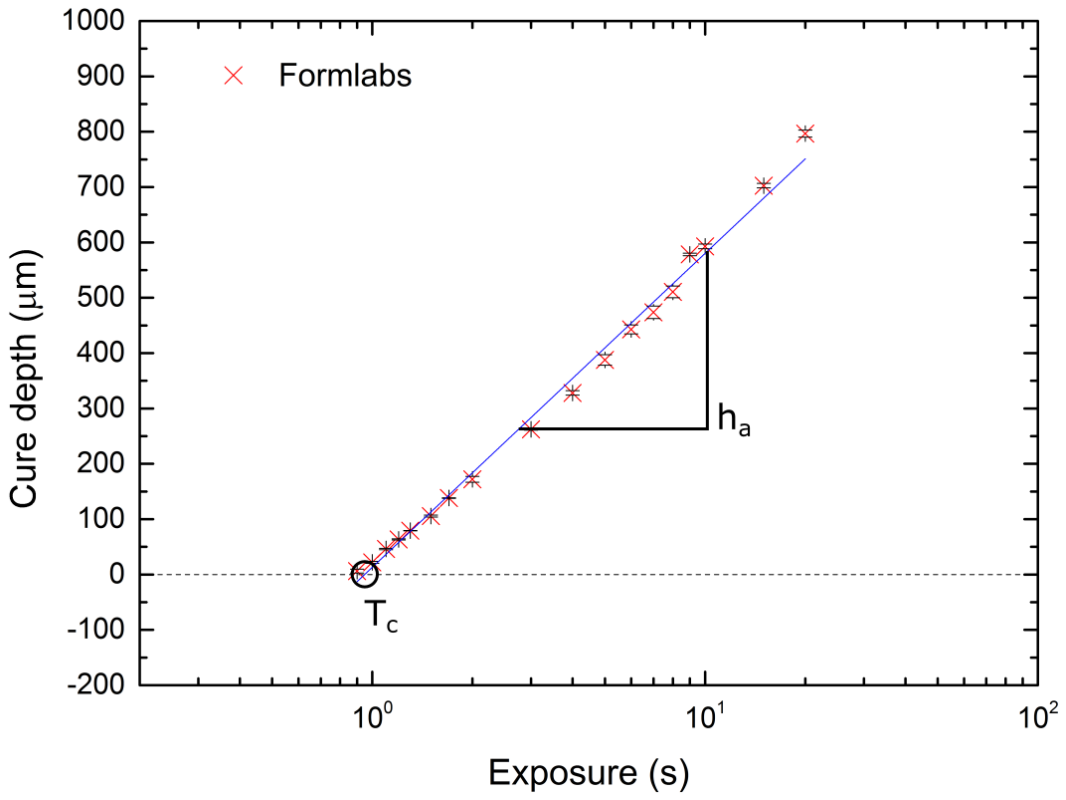

Figure 6.6. Working curve of cure depth vs. exposure time for Formlabs Clear photopolymer resin and Asiga 405 nm 25 mW/cm^2 UV-LED. Resin parameters h_a and T_c were calculated using a linear curve fit of equation (6.2) to the data. Error bars are standard deviation of membrane thickness over the entire ROI.

Figure 6.7 shows a semilog plot of the combined working curves of the three materials studied showing the relationship between slope and *x*-intercept. Corresponding resin material characteristics h_a and T_c outlined in Table 6.2. Individual working curves for each resin with a linear curve fit of equation (6.2) can be seen in Figure 6.8, Figure 6.9 and Figure 6.10.

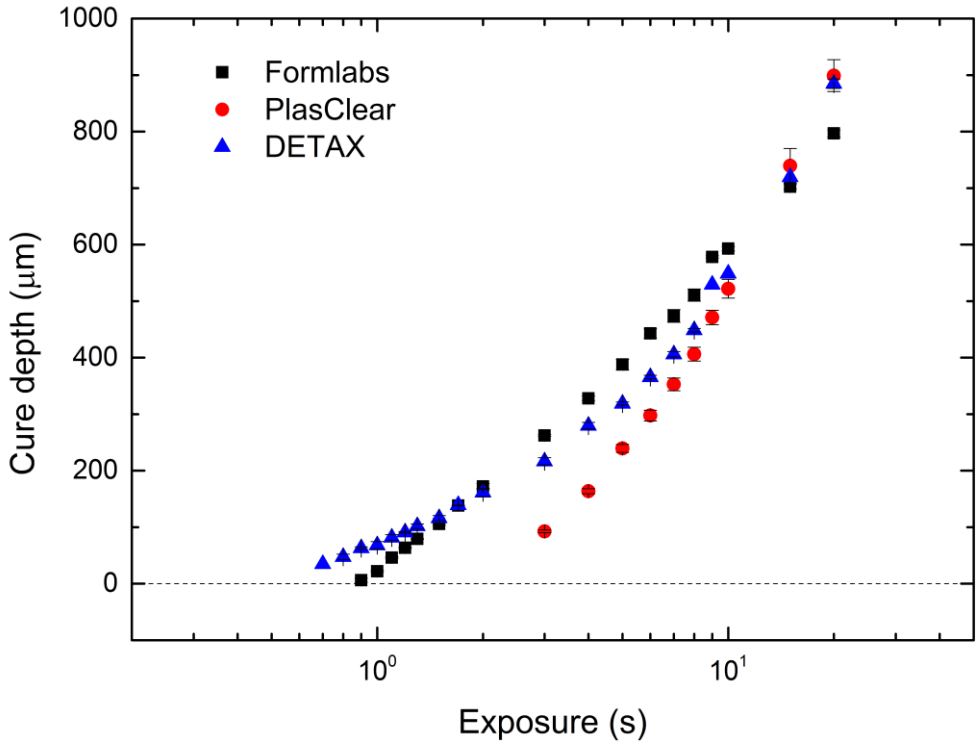

Figure 6.7. Exposure time working curve (cure depth vs exposure time) for three photopolymer materials; Formlabs Clear, Asiga PlasClear v2, and DETAX Freeprint Mould.

Table 6.2. Experimental constants h_a and T_c calculated from resin working curves.

Photopolymer resin	**Penetration depth, h_a (µm)**	**Critial time, T_c (s)**
DETAX Freeprint Mould	222.6225	0.80138
Formlabs Clear	246.27422	0.9482
Asiga PlasClear v2	338.36426	2.33124

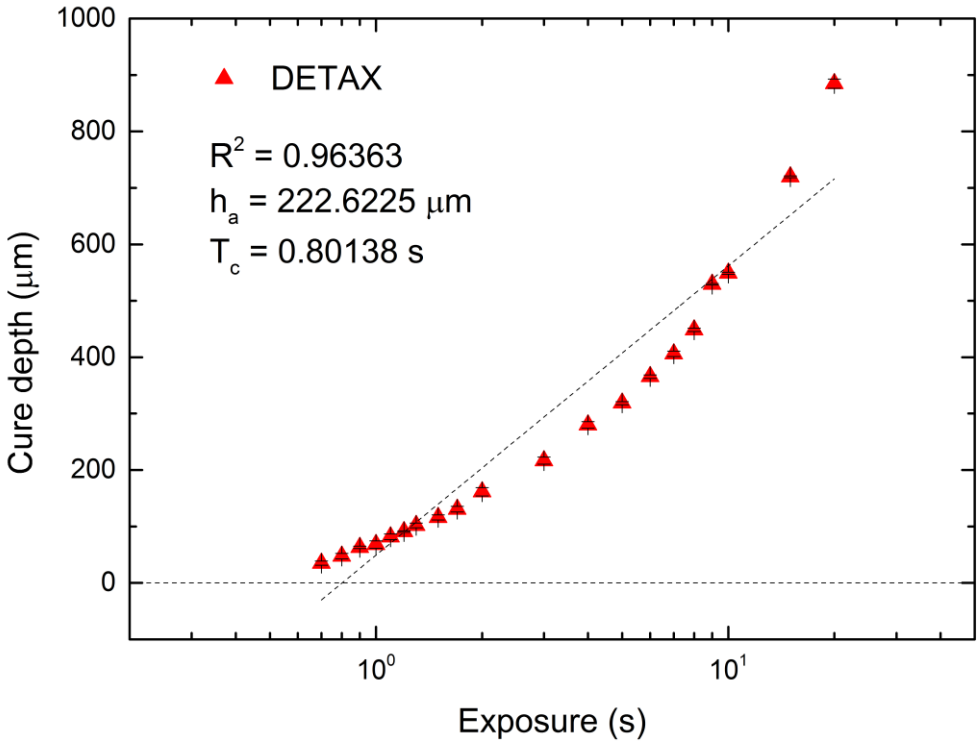

Figure 6.8. Exposure time working curve for DETAX Freeprint Mould, plotted with a least squares linear curve fit to equation (6.2).

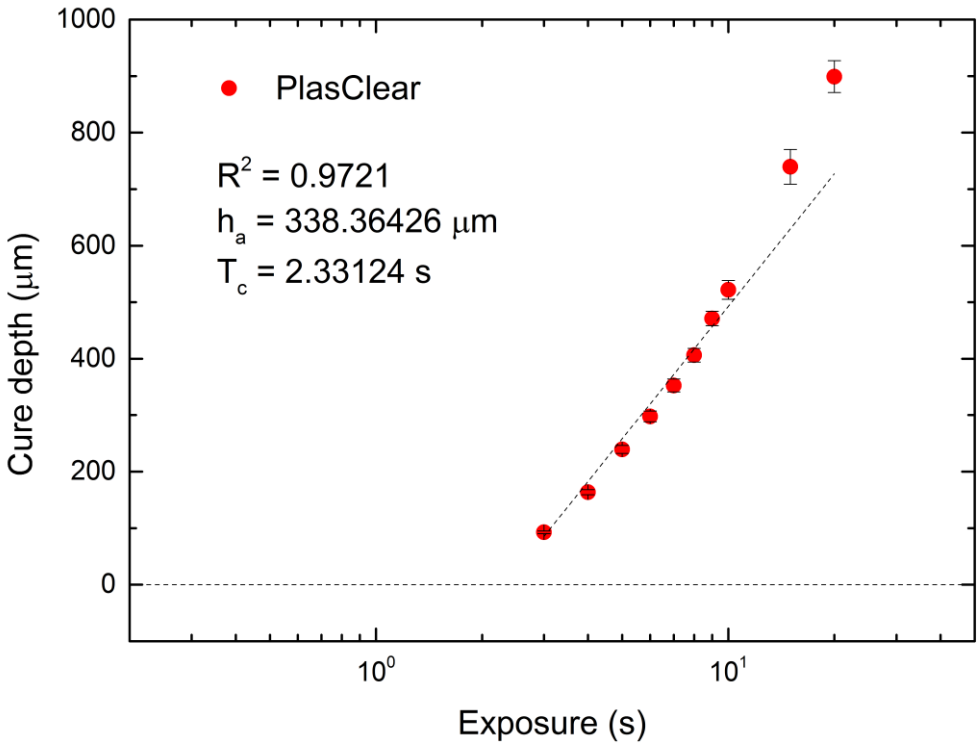

Figure 6.9. Exposure time working curve for Asiga PlasClear v2, plotted with a least squares linear curve fit to equation (6.2).

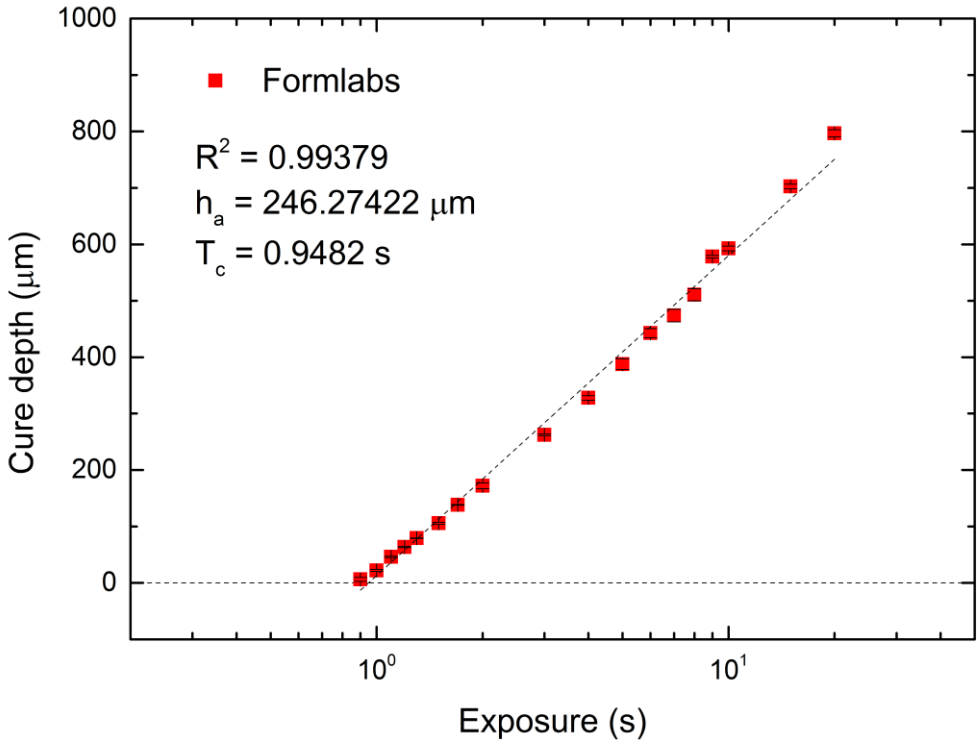

Figure 6.10. Exposure time working curve for Formlabs Clear, plotted with a least squares linear curve fit to equation (6.2).

6.2.5 Experimental validation of exposure times

To calculate optimum exposure time for each material and layer thickness the exposure time was initially set such that the normalised dose at the back of the layer $\Omega_{back} = 1$ (equation (5.16)). This is the dose at which the polymerisation threshold has just been reached. From this relationship, the layer exposure time t_l can be calculated by rearranging equation (5.14) to give equation (6.3) for minimum layer exposure time.

$$t_l = T_c e^{z_l/h_a} \tag{6.3}$$

Layer exposure time t_l was then increased by 0.1s until the exposure time setting resulted in a successful print. This procedure was repeated for all three materials. Exposure settings for all three materials and corresponding layer thicknesses are outlined in Table 6.3.

Table 6.3. Experimental parameters; layer thickness (z_l), normalised layer thickness (ζ_l), and exposure time (t_l) for three photopolymer materials: DETAX Freeprint mould (DX), Formlabs Clear (FL), and PlasClear v2.0 (PC).

	DX			**FL**			**PC**		
$\boldsymbol{z_l}$ **(µm)**	10	25	50	10	25	50	10	25	50
$\boldsymbol{\zeta_l}$	0.04	0.11	0.22	0.04	0.1	0.2	0.03	0.07	0.15
$\boldsymbol{t_l}$ **(s)**	1.1	1.2	1.3	1.1	1.2	1.3	2.7	2.9	3.1

6.2.6 Experimental design

Experiments were designed to assess the capability of the predictive design model to mitigate for the level of overcuring and improve resolution and repeatability of the MPµSL technique. To this effect, microfluidic channels were designed in two shapes and with a varying number of enclosing layers ($\lambda = 10, 25, 50$), and slice thickness settings ($z_l = 10, 25, 50$). Three commercially available photopolymer materials with different material characteristics (h_a and T_c) were chosen. The input channel dimension for both square and circular channels was kept constant. Unmodified and modified CAD models were both printed in the same build to alleviate differences between photopolymer material batches and all designs were replicated three times to gauge repeatability. The experimental design space is shown in Table 6.4.

Table 6.4. Experimental design space

Parameter	**Levels**	**Unit(s)**	**N**
Channel shape	Square, Circle	-	2
Enclosing layers (λ)	10, 25, 50	-	3
Slice thickness (z_l)	10, 25, 50	µm	3
Material	DX, FL, PC	-	3
Channel dimension	540	µm	1
Model	Unmodified, Modified	-	2
Repetitions	1, 2, 3	-	3
		Total	324

6.2.7 CAD models

Three CAD designs were developed to test the mathematical model based on the experimental design outlined in Table 6.4. Individual models were designed to correspond to the 3D printer slice thickness values $z_l = 10$, 25 and 50 μm respectively. In each design, the total thickness of the enclosing layers above the channel varies based on the input slice thickness as shown in Table 6.5.

Table 6.5. Total thickness of the enclosing layers ($z_l \times \lambda$) (μm) above the microfluidic channels.

Layer thickness (z_l, μm)	**Total thickness of enclosing layers (μm)**		
	$\boldsymbol{\lambda = 10}$	$\boldsymbol{\lambda = 25}$	$\boldsymbol{\lambda = 50}$
10	100	250	500
25	250	625	1250
50	500	1250	2500

A 3D isometric view of the CAD designs is shown in Figure 6.11. All models were designed using SolidWorks 2016 CAD software (Dassault Systèmes SolidWorks Corp., MA, USA).

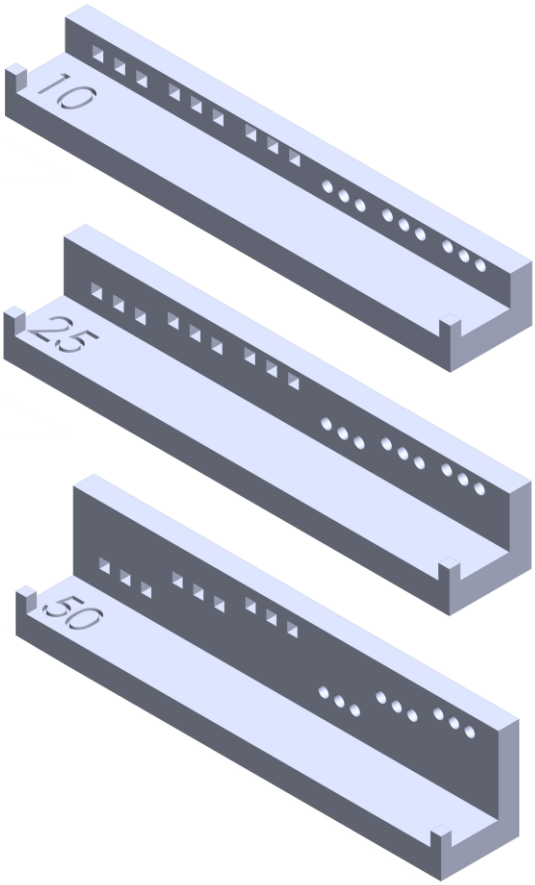

Figure 6.11. Isometric view of the CAD designs used for validation of the predictive model. Each model corresponds to a slice thickness value, z_l = 10, 25, and 50 μm respectively.

Models contain both square and circular channels at three depths within the part corresponding to three levels of enclosing layers ($\lambda = 10,\ 25,$ and 50 layers). The CAD model design characteristics are outlined in detail in Figure 6.12. In addition, each channel is replicated (n=3) within the part to ensure repeatability of results. Replicates were designed to be printed in a single run to minimise time-based curing variability between polymer batches.

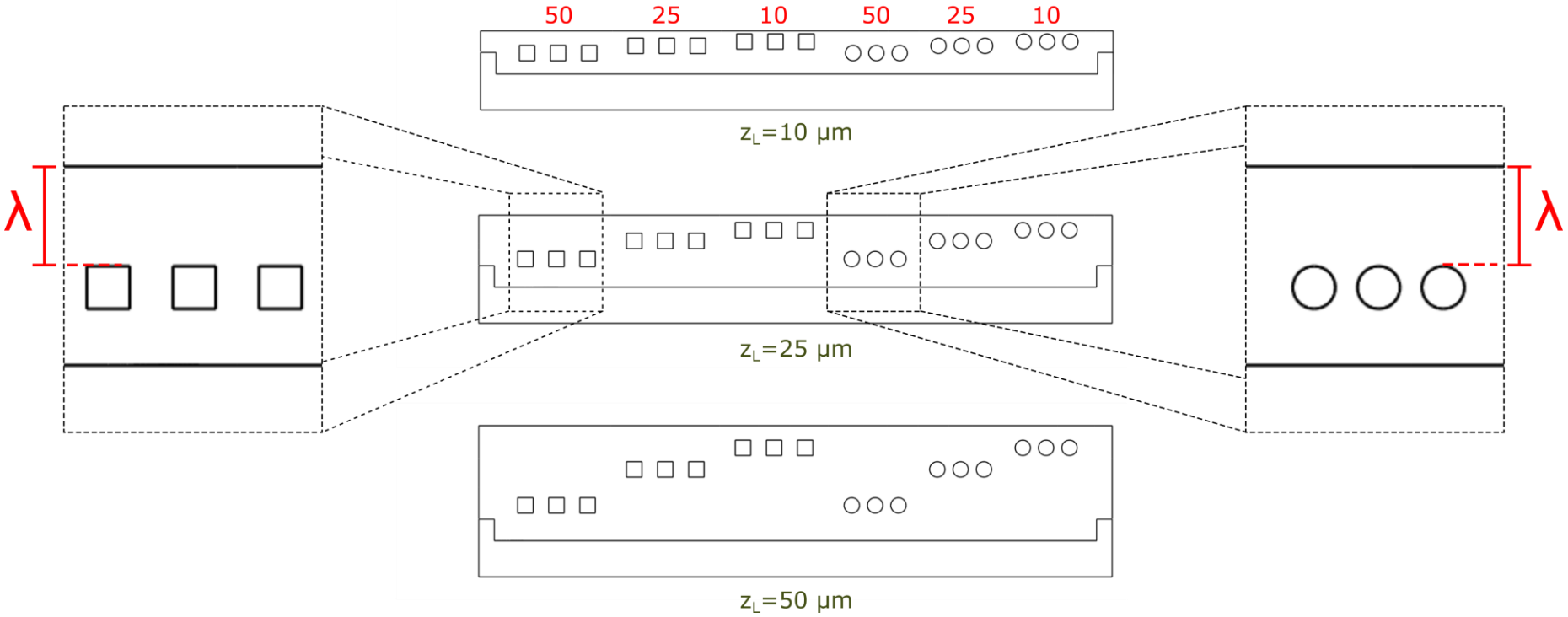

Figure 6.12. Front elevation view of the CAD designs used for validation of the predictive model. Experimental design parameters are coloured, number of enclosing layers (λ) in red, and layer thickness (z_l) in green. The number of enclosing layers (λ) is counted from the top of the channel for both square and circular channels as outlined by the magnified sections of the image.

After design, the CAD models were exported in the 'stereolithography' (STL) file format and imported to Asiga Composer software (Asiga, Anaheim Hills, CA, USA) for placement on the build platform. Models were sliced at three slice thickness intervals (z_l) of 10, 25 and 50 μm respectively corresponding to the experimental design parameters in Table 6.4. Exposure time (t_l) for the three materials was set based on the results from section 6.2.5 (see Table 6.3). Raw and modified models were placed in the same build to minimise time-based curing variability between polymer batches as shown in Figure 6.13.

The Asiga 3D printer DMD optical engine is oriented in a diamond pixel orientation as previously reported by Gong et al.[12] and verified in section 6.2.1. Thus, all parts are oriented at 45° on the build platform with respect to the x-axis as shown in Figure 6.13.

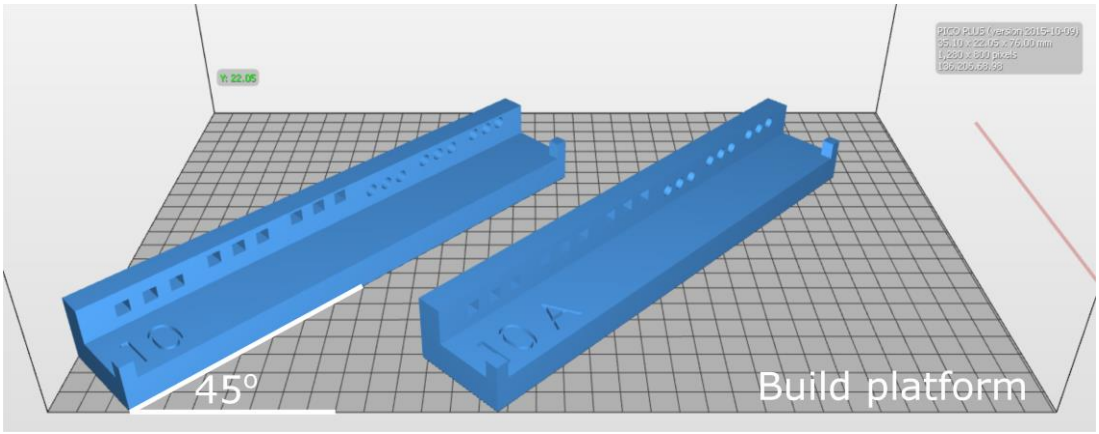

Figure 6.13. Image from Asiga Composer software showing the orientation of the CAD models on the build platform. Models are oriented at 45° w.r.t the x-axis to align with the 3D printer DMD pixel orientation.

6.2.8 Predictive model

After slicing, the sliced image stacks were downloaded from the Asiga printer web interface and converted into 3D voxel arrays using a custom script developed for this purpose using LabVIEW™ 2016 software (National Instruments, TX, USA). The 3D voxel arrays were then run through the bespoke algorithm developed for this study and reported in Chapter 5 to predict and mitigate for the effects of overcuring. When complete, the modified voxel array was re-sliced and converted back into a binary PNG image stack for upload to the 3D printer.

Maximum number of iterations (i_{max}) for the design model was set based on the number of enclosing layers (λ), such that:

$$i_{max} \leq \lambda \tag{6.4}$$

Values for i_{max} corresponding to each material and model are shown in Table 6.6.

Table 6.6. Maximum iterations ($i_{max} \leq \lambda$) for each microfluidic channel model categorised by material: DETAX Freeprint mould (DX), Formlabs Clear (FL), and PlasClear (PC).

Slice thickness (z_l)	**Enclosing layers (λ)**	**Maximum iterations (i_{max})**		
		DX	**FL**	**PC**
10	**10**	8	8	8
	25	23	23	14
	50	44	44	47
25	**10**	8	8	9
	25	17	17	21
	50	22	22	34
50	**10**	6	6	9
	25	8	8	15
	50	8	8	16

6.2.9 Printing and part development

Prior to 3D printing, the build platform and slider mechanism were calibrated, and the polymer materials were remixed and subsequently degassed under vacuum for ~30-45 minutes. Immediately after fabrication, unsolidified photopolymer resin was flushed from the 3D printed flow channels. Briefly, the part is removed from the build platform, rinsed with IPA, and sonicated in a bath of IPA for ~5 minutes (Branson 3510 sonicator, Branson Ultrasonics, CT, USA). The part is then removed, and the micro-canals are aspirated using a vacuum aspirator (Bel-Art™ SP Scienceware, NJ, USA). It is important to thoroughly aspirate the photopolymer residue from the micro-channels as polymerisation may continue after fabrication from exposure to ambient UV-light.

6.3 Results and discussion

6.3.1 Modified versus unmodified builds

An overview of the results comparing modified and unmodified channels is shown in Figure 6.14, Figure 6.15, and Figure 6.16 for three materials, DETAX Freeprint mould, Formlabs Clear, and Asiga PlasClear v2.0, respectively. Additional results are shown in Appendix C.

Fabrication of microchannels via the standard method is extremely ineffective often resulting in blocked channels, as evidenced by the results for the unmodified model 'A' in Figure 6.14, Figure 6.15, and Figure 6.16 below. In fact, using the standard method yields fully formed channels in less than 7% of the cases studied. In comparison, upon application of the new design algorithm for mitigation of the overcuring effect, most of the microchannels are unblocked and fully formed resulting in a success rate of 98%.

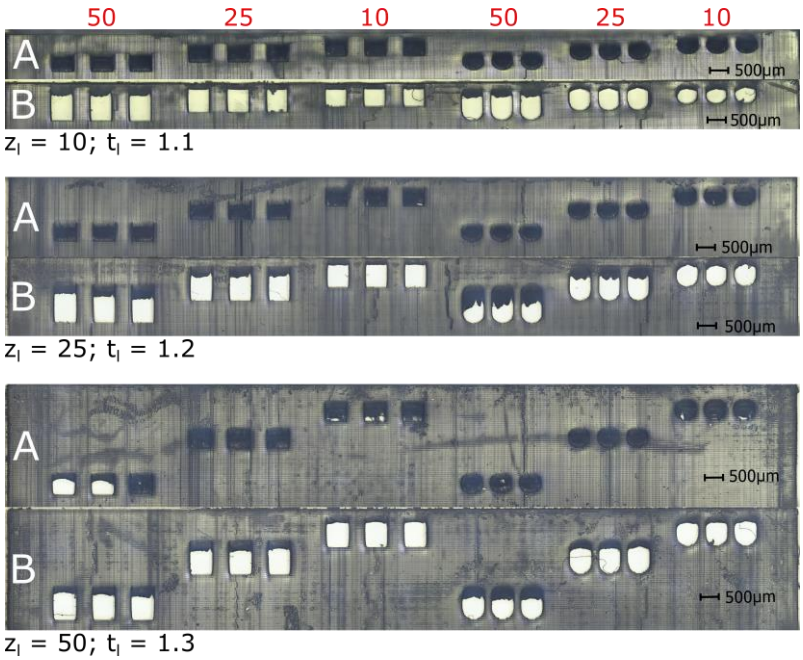

Figure 6.14. Comparison of the unmodified (A) and modified (B) parts produced via the MPµSL technique using DETAX Freeprint Mould photopolymer resin for three paired layer thickness (z_l) and layer exposure time (t_l) settings.

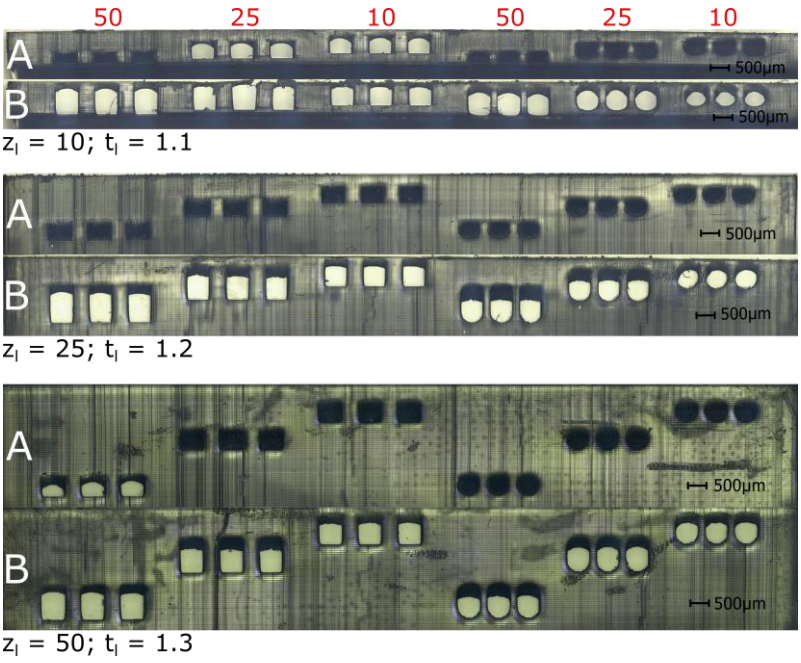

Figure 6.15. Comparison of the unmodified (A) and modified (B) parts produced via the MPµSL technique using Formlabs Clear photopolymer resin for three paired layer thickness (z_l) and layer exposure time (t_l) settings.

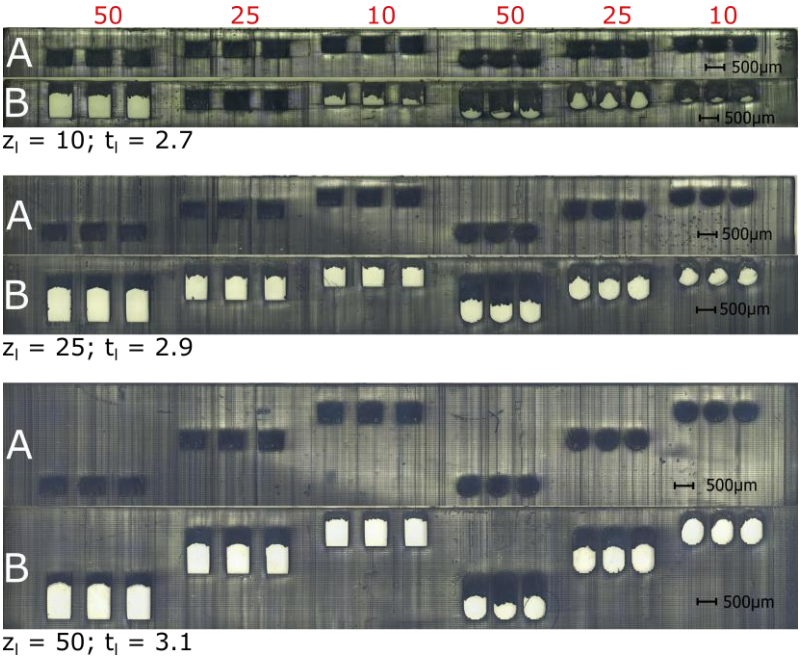

Figure 6.16. Comparison of the unmodified (A) and modified (B) parts produced via the MPµSL technique using Asiga PlasClear v2.0 photopolymer resin for three paired layer thickness (z_l) and layer exposure time (t_l) settings.

6.3.2 Channel height prediction

Predicted channel height from the final output of the numerical model is compared to the experimentally derived values for square and circular models for the three materials in Figure 6.17 to Figure 6.22 inclusive. As expected, there is a large variation in channel height throughout the results for both predicted and measured values due to variation in the experimental parameters λ, and z_l. For square channels, the difference between the predicted channel height and the experimental value was found to be an average of 204 μm with a 95% CI of $\pm 28\,\mu$m. For circular channels, the difference between the predicted channel height and the experimental values was found to be 124 μm with a 95% CI of $\pm 26\,\mu$m, with both the measured channel height and the predicted channel height varying based on the number of enclosing layers, slice thickness, and material characteristics. These differences represent a deviation of $38 \pm 5\%$ and $23 \pm 5\%$ from the input value of 540 μm for square and circular channels respectively. This is to be expected as the prediction error of the exposure threshold model currently used in industry is up to 50%[161].

In all results, the numerical model overpredicts the level of overcuring and thus overcompensates, producing channels that are larger than the desired input dimension. However, despite these inaccuracies, the numerical model results follow the trend of the data closely. To illustrate this, the predicted channel heights from the numerical model are shifted by the average difference, 204 μm and 124 μm, for square and circular channels in Figure 6.23 and Figure 6.24 respectively.

Variation in the level of overcure between the predicted and the measured result is likely due to limitations imposed on the model by the initial assumptions made in Chapter 5.

Model assumptions include:

1. Exposure is additive for each layer
2. Interference between DMD pixels is negligible
3. Threshold model of resin cure is valid
4. The resin molecules underneath the part being cured are stationary
5. The cleaning process can completely remove the surrounding uncured resin

To account for this variation between predicted and measured results in the current model, the threshold value for polymerisation (normalised dose, $\Omega = 1.0$) used in simulation can be tuned to provide more accurate simulation results.

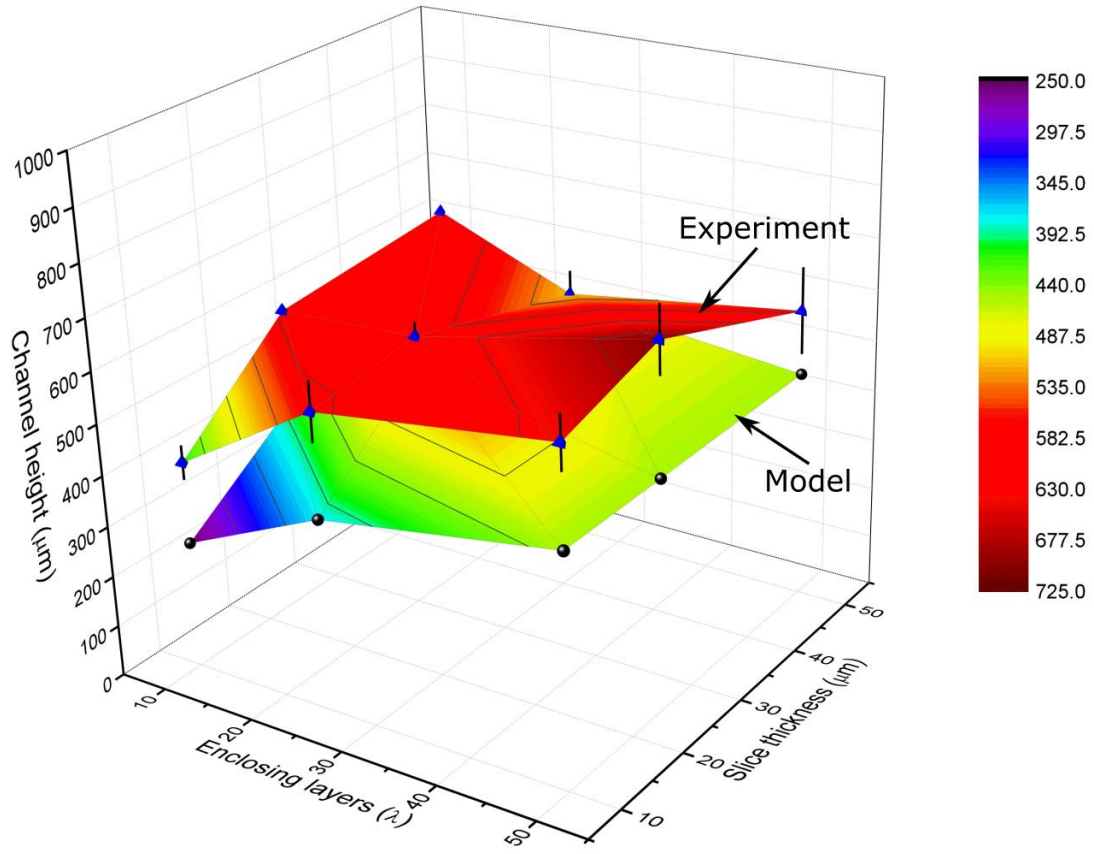

Figure 6.17. Variation of channel height (µm) with number of enclosing layers (λ) and slice thickness (z_l) (µm) for circular channels fabricated using DETAX Freeprint Mould Clear photopolymer material. The numerical model follows the trend of the experimental data closely. Error bars represent a 95% CI.

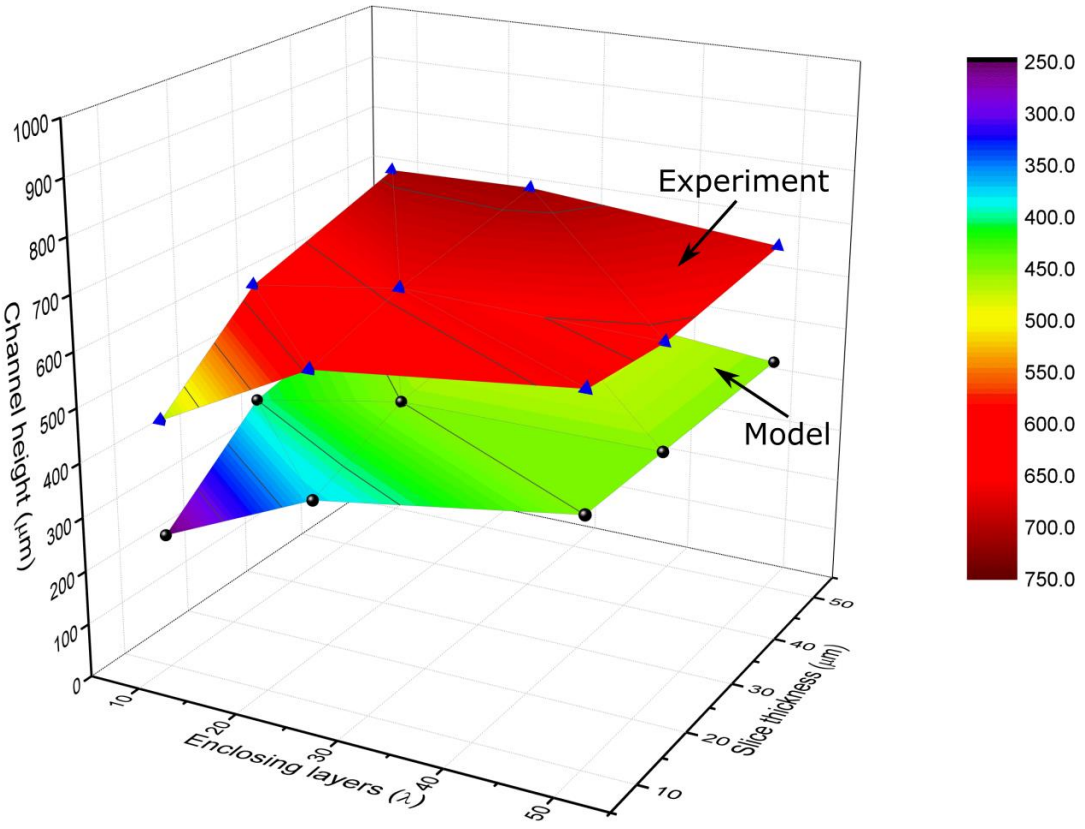

Figure 6.18. Variation of channel height (µm) with number of enclosing layers (λ) and slice thickness (z_l) (µm) for square channels fabricated using DETAX Freeprint Mould Clear photopolymer material. The numerical model follows the trend of the experimental data closely. Error bars represent a 95% CI.

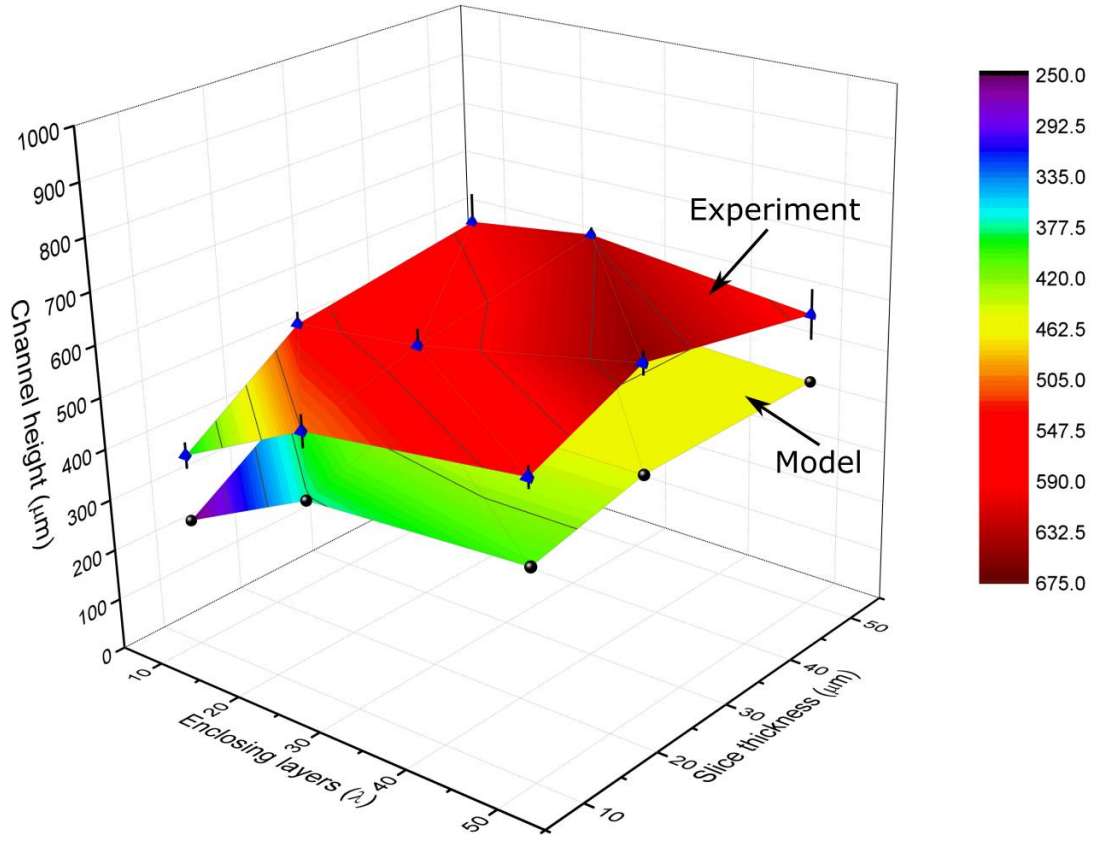

Figure 6.19. Variation of channel height (µm) with number of enclosing layers (λ) and slice thickness (z_l) (µm) for circular channels fabricated using Formlabs Clear photopolymer material. The numerical model follows the trend of the experimental data closely. Error bars represent a 95% CI.

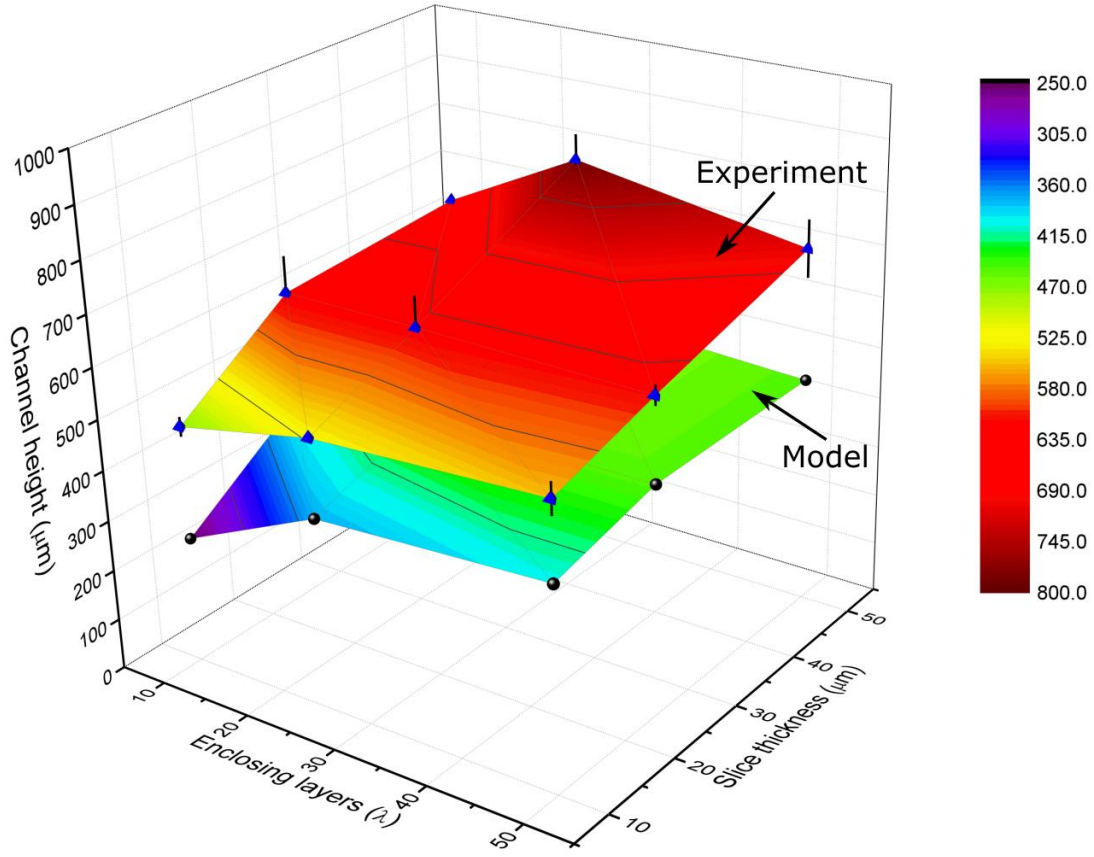

Figure 6.20. Variation of channel height (µm) with number of enclosing layers (λ) and slice thickness (z_l) (µm) for square channels fabricated using Formlabs Clear photopolymer material. The numerical model follows the trend of the experimental data closely. Error bars represent a 95% CI.

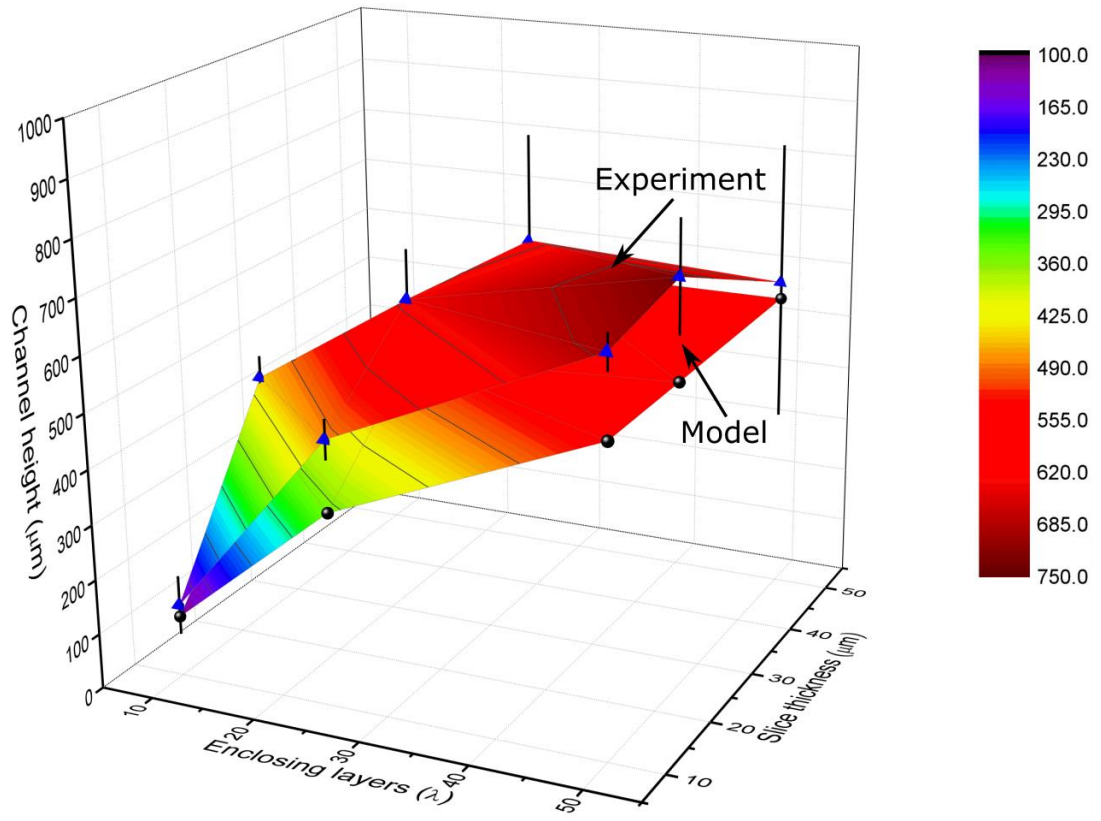

Figure 6.21. Variation of channel height (µm) with number of enclosing layers (λ) and slice thickness (z_l) (µm) for circular channels fabricated using Asiga PlasClear v2 photopolymer material. The numerical model follows the trend of the experimental data closely. Error bars represent a 95% CI.

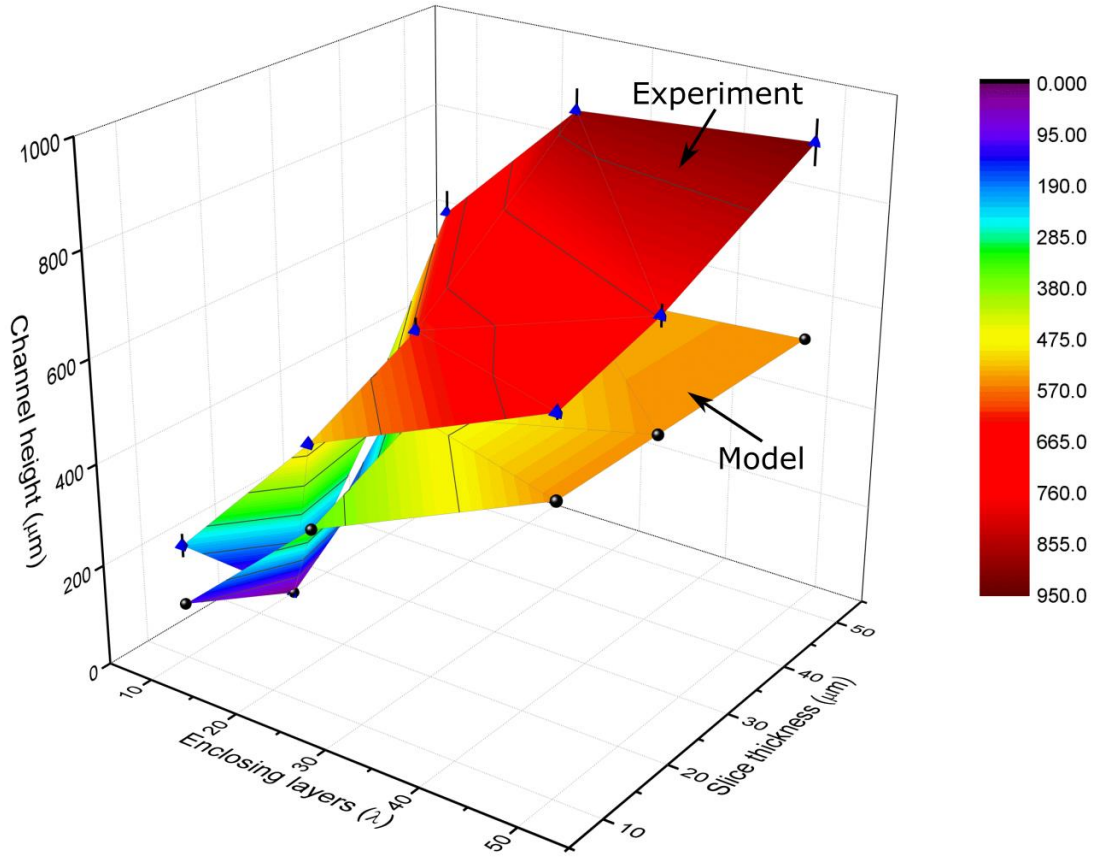

Figure 6.22. Variation of channel height (µm) with number of enclosing layers (λ) and slice thickness (z_l) (µm) for square channels fabricated using Asiga PlasClear v2 photopolymer material. The numerical model follows the trend of the experimental data closely. Error bars represent a 95% CI.

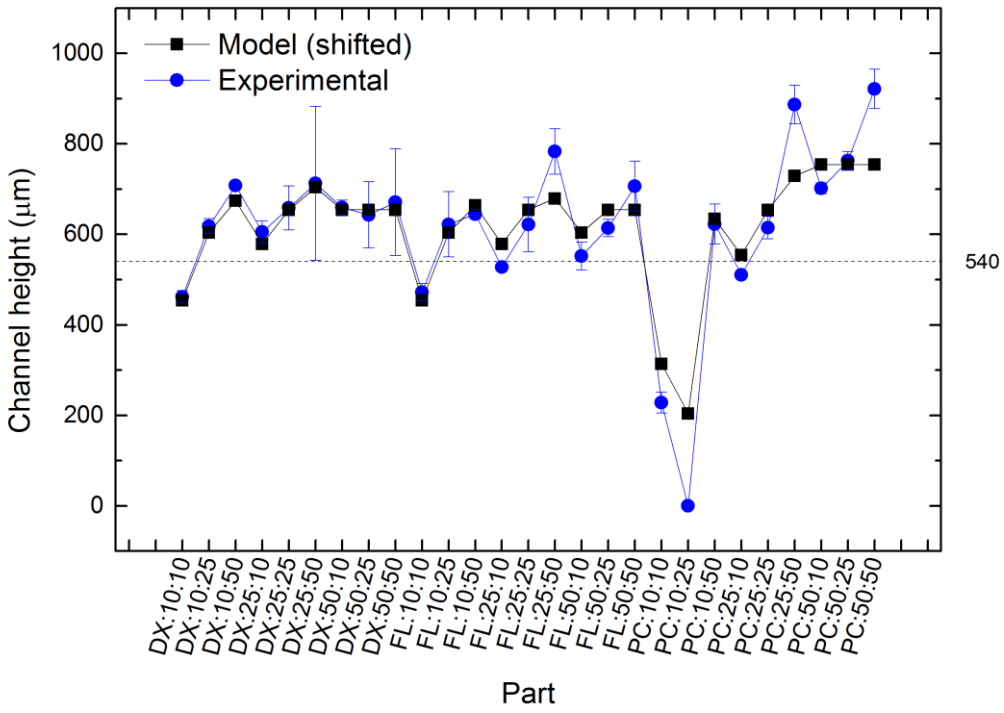

Figure 6.23. Validation of the numerical model for square channels, showing modelled and experimental channel heights (y) versus experiment (x). The results from the numerical model are shifted by the average difference (204 μm) to demonstrate agreement with the general trend of the experimental data. X-axis labels are in the format (Material):(Slice thickness (z_l)):(Number of enclosing layers (λ)). Error bars represent a 95% CI.

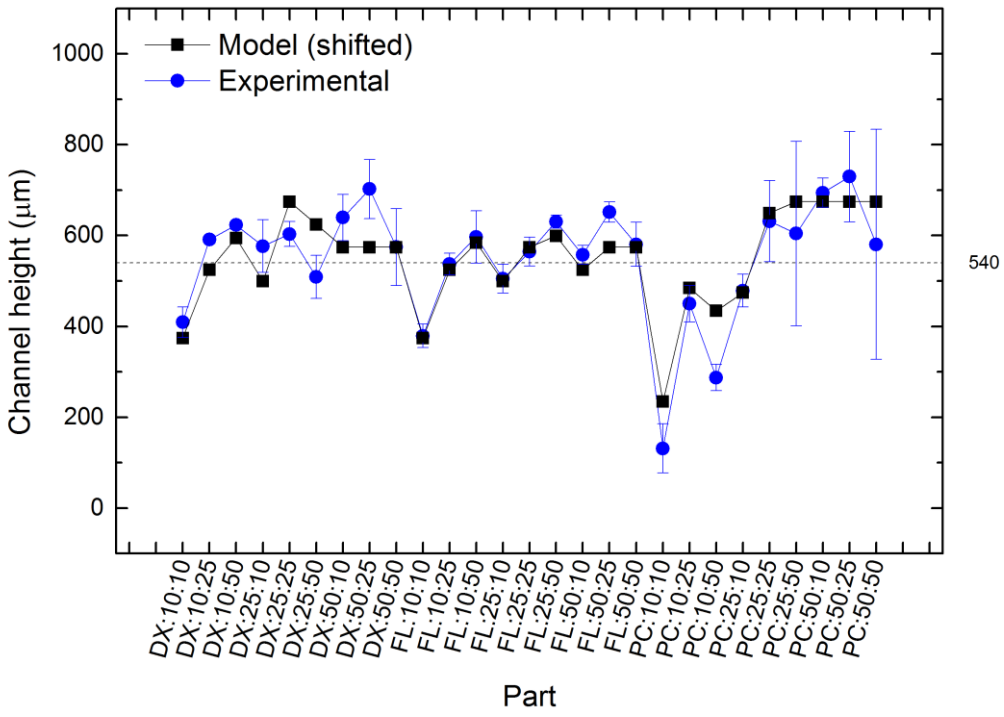

Figure 6.24. Validation of the numerical model for circular channels, showing modelled and experimental channel heights (y) versus experiment (x). The results from the numerical model are shifted by the average difference (124 μm) to demonstrate agreement with the general trend of the experimental data. X-axis labels are in the format (Material):(Slice thickness (z_l)):(Number of enclosing layers (λ)). Error bars represent a 95% CI.

6.4 Conclusions

A new design algorithm, discussed in Chapter 5, for mitigating the overcuring effect in MPμSL was experimentally validated using three photopolymer materials. Using the model developed in this work, it is possible to alter the 3D voxel array to mitigate for the effects of overcuring inherent in SL 3D printing processes. This presents a new approach to solving this problem while building on previous research which focused mainly on improvements in 3D printer hardware[10,14] and resin chemistry[12,13].

Microfluidic models were designed using standard CAD software and the design algorithm was applied to the resulting 3D voxel arrays to mitigate for the effects of overcure. Comparison of the raw input designs and the mitigated designs shows the strength in this approach in improving the success rate of the MPμSL fabrication technique for microfluidic channel formation. Results show an improvement in the success rate from 7% to 98% using the new method.

Overcompensation of the new design model resulted in channel heights larger than the input dimension of $38 \pm 5\%$ and $23 \pm 5\%$ for square and circular channel dimensions respectively. Despite this, the predicted channel height closely follows the trend of the measured results suggesting that the threshold value for polymerisation ($\Omega = 1.0$) used in simulation should be increased to provide more accurate simulation results.

Although previous results reported in the literature[12] suggest that the minimum channel height for a particular resin is $\sim 3.5 - 5.5 h_a$, it has been shown here that smaller channel heights can be achieved by mitigating for the effects of overcuring in the design before fabrication. In the current work, this resolution limit has been reduced to $\sim 1.3 - 2.9 h_a$. However, minimum resolution is no longer limited by the resin material characteristic penetration depth h_a. The current model sets a new minimum limit tied to the number of enclosing layers (λ), with an increase in the number of enclosing layers resulting in greater control over the final channel shape.

This new approach enables fabrication of microfluidic channels in a wider range of materials, removing the need for bespoke high-resolution doped materials for internal void fabrication thus enabling faster build times and allowing the designer to use cheaper alternative materials.

Chapter 7
Conclusions

7.1 Conclusions

Microfluidic device fabrication has, since the early 90's, remained largely unchanged. Conventional fabrication techniques are time-and-labour intensive, and often require access to clean-room facilities. Furthermore, these techniques are difficult to automate and are predominantly restricted to planar fabrication, limiting designs to two dimensions. In view of these limitations, 3D printing has attracted attention as an alternative fabrication technique providing automated, assembly-free 3D fabrication.

3D printing minimises the barriers to manufacturing, enabling engineers and scientists to create custom microfluidic devices for a wide range of applications at a fraction of the cost. Despite this, fabrication of microfluidic channels via 3D printing is challenging for many reasons including: support material removal, print resolution, chemical compatibility of materials, and high cost of equipment. Of the currently available 3D printing techniques, MPμSL is uniquely positioned to address these problems, however, it is not without its own limitations. Addressing these limitations forms the basis for the current research.

The objectives of this research included:

— To investigate MPμSL for fabrication of internal microfluidic channels in a bulk substrate material in a single step.
— To develop a rapid prototyping technique for common laboratory-based microfluidic applications.
— To address the limitations in the direct production of internal microfluidic channels via the MPμSL 3D printing method.

The following represent the main conclusions from the current work:

— The MPμSL technique is capable of producing microfluidic channels in a bulk material substrate in a single step and without the need for support structures. In addition, integration of high pressure threaded microfluidic fittings was demonstrated with a maximum achievable backpressure of 12 MPa. The main limitation of the technique, namely overcure, was identified and characterised. This results in poor resolution in the *z*-direction and causes blockage of microfluidic channels oriented horizontally with respect to the build platform.
— Integration of a laboratory-based SPE technique on to a 3D printed microfluidic chip with integrated weir and luer-lock fittings was demonstrated.
— A new approach to addressing the problem of overcure in MPμSL was developed. This approach is based on a new iterative design algorithm for prediction and mitigation of the overcuring effect for both internal and external features toward the production of high resolution internal microfluidic channels.
— Convergence of the new design model is based on the number of enclosing layers above the void being greater than the polymerisation depth for the given layer polymerisation time. Using the new model, it was shown that an increase in the number of enclosing layers above the channel results in a corresponding increase in resolution. This is a significant improvement on the technique where previously an increase in the number of enclosing layers resulted in channel blockage and poorer resolution.
— The new design algorithm was experimentally validated for microfluidic channel production in three materials demonstrating an improvement in reproducibility of microfluidic channels and improvements in resolution over previous work in the literature. A new minimum channel height based on the resin characteristic penetration depth and number of enclosing layers can now be achieved.
— Limitations imposed by overcuring of the resin material can be overcome through the application of the new design algorithm removing the need for bespoke high-resolution doped materials for internal void fabrication enabling faster build times and allowing the designer the freedom to use cheaper alternative materials.

7.2 Suggested future work

The following is recommended for further study:

- Application of the new technique to the fabrication of new microfluidic devices to characterise speed and cost compared with other AM and traditional fabrication techniques.
- Development of the current design algorithm to improve memory management to increase speed and enable analysis of larger microfluidic networks.
- Expansion of the current MPμSL simulation model to include additional terms for mass and heat transfer[162], and to account for the effects of the polychromatic light source[123].

Finally, the new design algorithm developed in the current work creates further possibilities toward the fabrication of high resolution microfluidic devices when combined with other approaches in the literature (i.e. increasing resin optical absorption[12,13], and improvements in 3D printer hardware[10,14,123]) suggesting that a new minimum microchannel height resolution is achievable. Further research is needed to fully characterise minimum channel height using this multifaceted approach.

References

1. O'Neill PF, Ben Azouz A, Vázquez M, Liu J, Marczak S, Slouka Z, Chang HC, Diamond D, Brabazon D. Advances in three-dimensional rapid prototyping of microfluidic devices for biological applications. *Biomicrofluidics* 2014; 8: 052112.
2. O'Neill P, Jolivet L, Kent NJ, Brabazon D. Physical integrity of 3D printed parts for use as embossing tools. *Adv Mater Process Technol* 2017; 0698: 1–10.
3. Kent NJ, Jolivet L, O'Neill P, Brabazon D. An evaluation of components manufactured from a range of materials, fabricated using PolyJet technology. *Adv Mater Process Technol* 2017; 0698: 1–12.
4. O'Neill PF, Kent N, Brabazon D. Mitigation and control of the overcuring effect in mask projection micro-stereolithography. In: *Proceedings of the 20th International ESAFORM Conference on Material Forming*. American Institute of Physics, 2017, p. 200012.
5. O'Neill P, Barrett A, Sullivan T, Regan F, Brabazon D. Rapid Prototyped Biomimetic Antifouling Surfaces for Marine Applications. *Mater Today Proc* 2016; 3: 527–532.
6. Waldbaur A, Rapp H, Länge K, Rapp BE. Let there be chip—towards rapid prototyping of microfluidic devices: one-step manufacturing processes. *Anal Methods* 2011; 3: 2681.
7. Au AK, Lee W, Folch A. Mail-order microfluidics: evaluation of stereolithography for the production of microfluidic devices. *Lab Chip* 2014; 14: 1294–301.
8. Shallan AI, Smejkal P, Corban M, Guijt RM, Breadmore MC. Cost-Effective Three-Dimensional Printing of Visibly Transparent Microchips within Minutes. *Anal Chem* 2014; 86: 3124–3130.
9. Bhattacharjee N, Urrios A, Kang S, Folch A. The upcoming 3D-printing revolution in microfluidics. *Lab Chip* 2016; 16: 1720–1742.
10. Tumbleston JR, Shirvanyants D, Ermoshkin N, Janusziewicz R, Johnson AR, Kelly D, Chen K, Pinschmidt R, Rolland JP, Ermoshkin A, Samulski ET, DeSimone JM. Continuous liquid interface production of 3D objects. *Science (80-)* 2015; 347: 1349–1352.
11. Yong C, Yuanrui L, Huachao M, Wei W. *3D printing with variable voxel sizes based on optical filter*. US 2017/0307902 A1, US: United States Patent and Trademark Office, 2017.
12. Gong H, Beauchamp M, Perry S, Woolley AT, Nordin GP. Optical approach to resin formulation for 3D printed microfluidics. *RSC Adv* 2015; 5: 106621–106632.
13. Choi J, Wicker RB, Cho S, Ha C, Lee S. Cure depth control for complex 3D microstructure fabrication in dynamic mask projection microstereolithography. *Rapid Prototyp J* 2009; 15: 59–70.

14. Janusziewicz R, Tumbleston JR, Quintanilla AL, Mecham SJ, DeSimone JM. Layerless fabrication with continuous liquid interface production. *Proc Natl Acad Sci* 2016; 113: 11703–11708.

15. Tabeling P. *Introduction to Microfluidics*. Paris: Oxford University Press, 2010.

16. Nge PN, Rogers CI, Woolley AT. Advances in Microfluidic Materials, Functions, Integration, and Applications. *Chem Rev* 2013; 113: 2550–2583.

17. Harrison DJ, Manz A, Fan Z, Ludi H, Widmer HM. Capilliary Electrophoresis and Sample Injection Systems Integrated on a Planar Glass Chip. *Anal Chem* 1992; 7: 249–255.

18. Lagally ET, Simpson PC, Mathies R a. Monolithic integrated microfluidic DNA amplification and capillary electrophoresis analysis system. *Sensors Actuators B Chem* 2000; 63: 138–146.

19. Wang Y, Chen H, He Q, Soper S a. A high-performance polycarbonate electrophoresis microchip with integrated three-electrode system for end-channel amperometric detection. *Electrophoresis* 2008; 29: 1881–1888.

20. Chou H, Unger MA, Stephen R. A Microfabricated Rotary Pump 1. 2001; 323–330.

21. Bruchet A, Taniga V, Descroix S, Malaquin L, Goutelard F, Mariet C. Centrifugal microfluidic platform for radiochemistry: Potentialities for the chemical analysis of nuclear spent fuels. *Talanta* 2013; 116: 488–494.

22. Nivedita N, Papautsky I. Continuous separation of blood cells in spiral microfluidic devices. *Biomicrofluidics* 2013; 7: 054101.

23. Verpoorte E. Microfluidic chips for clinical and forensic analysis. *Electrophoresis* 2002; 23: 677–712.

24. Dishinger JF, Kennedy RT. Serial immunoassays in parallel on a microfluidic chip for monitoring hormone secretion from living cells. *Anal Chem* 2007; 79: 947–54.

25. Dittrich PS, Manz A. Lab-on-a-chip: microfluidics in drug discovery. *Nat Rev Drug Discov* 2006; 5: 210–218.

26. Liu P, Mathies RA. Integrated microfluidic systems for high-performance genetic analysis. *Trends Biotechnol* 2009; 27: 572–581.

27. Kimura H, Yamamoto T, Sakai H, Sakai Y, Fujii T. An integrated microfluidic system for long-term perfusion culture and on-line monitoring of intestinal tissue models. *Lab Chip* 2008; 8: 741–746.

28. Huh D, Matthews BD, Mammoto A, Montoya-Zavala M, Hsin HY, Ingber DE. Reconstituting Organ-Level Lung Functions on a Chip. *Science (80-)* 2010; 328: 1662–1668.

29. Tsai M, Kita A, Leach J, Rounsevell R, Huang JN, Moake J, Ware RE, Fletcher DA, Lam WA. In vitro modeling of the microvascular occlusion and thrombosis that occur in hematologic diseases using microfluidic technology. *J Clin Invest* 2012; 122: 408–418.

30. Huh D, Hamilton G a, Ingber DE. From 3D cell culture to organs-on-chips. *Trends Cell Biol* 2011; 21: 745–754.

31. Manz A, Graber N, Widmer HM. Miniaturized total chemical analysis systems: A novel concept for chemical sensing. *Sensors Actuators B Chem* 1990; 1: 244–248.

32. Dance A. The making of a medical microchip. *Nature* 2017; 545: 511–514.

33. Xia Y, Whitesides GM. Soft Lithography. *Angew Chemie Int Ed* 1998; 37: 550–575.

34. Duffy DC, McDonald JC, Schueller OJA, Whitesides GM. Rapid Prototyping of Microfluidic Systems in Poly(dimethylsiloxane). *Anal Chem* 1998; 70: 4974–4984.

35. Whitesides GM. The origins and the future of microfluidics. *Nature* 2006; 442: 368–373.

36. Bartholomeusz DA, Boutté RW, Andrade JD. Xurography : Rapid Prototyping of Microstructures Using a Cutting Plotter. *J Microelectromechanical Syst* 2005; 14: 1364–1374.

37. Kinahan DJ, Kearney SM, Dimov N, Glynn MT, Ducrée J. Event-triggered logical flow control for comprehensive process integration of multi-step assays on centrifugal microfluidic platforms. *Lab Chip* 2014; 14: 2249–58.

38. Kinahan DJ, Kearney SM, Kilcawley NA, Early PL, Glynn MT, Ducr??e J. Density-gradient mediated band extraction of leukocytes from whole blood using centrifugo-pneumatic siphon valving on centrifugal microfluidic discs. *PLoS One* 2016; 11: 1–13.

39. Attia UM, Marson S, Alcock JR. Micro-injection moulding of polymer microfluidic devices. *Microfluid Nanofluidics* 2009; 7: 1–28.

40. Ogilvie IRG, Sieben VJ, Floquet CF a, Zmijan R, Mowlem MC, Morgan H. Reduction of surface roughness for optical quality microfluidic devices in PMMA and COC. *J Micromechanics Microengineering* 2010; 20: 065016.

41. Azouz A Ben, Murphy S, Karazi S, Vázquez M, Brabazon D. Fast Fabrication Process of Microfluidic Devices Based on Cyclic Olefin Copolymer. *Mater Manuf Process* 2014; 29: 93–99.

42. Mair D a, Geiger E, Pisano AP, Fréchet JMJ, Svec F. Injection molded microfluidic chips featuring integrated interconnects. *Lab Chip* 2006; 6: 1346–1354.

43. Yazdi AA, Popma A, Wong W, Nguyen T, Pan Y, Xu J. 3D printing: an emerging tool for novel microfluidics and lab-on-a-chip applications. *Microfluid Nanofluidics* 2016; 20: 50.

44. Ren K, Zhou J, Wu H. Materials for Microfluidic Chip Fabrication. *Acc Chem Res* 2013; 46: 2396–2406.

45. Martinez AW, Phillips ST, Whitesides GM, Carrilho E. Diagnostics for the Developing World: Microfluidic Paper-Based Analytical Devices. *Anal Chem* 2010; 82: 3–10.

46. Coltro WKT, de Jesus DP, da Silva JAF, do Lago CL, Carrilho E. Toner and paper-based fabrication techniques for microfluidic applications. *Electrophoresis* 2010; 31: 2487–2498.

47. Hu J, Wang S, Wang L, Li F, Pingguan-Murphy B, Lu TJ, Xu F. Advances in paper-based point-of-care diagnostics. *Biosens Bioelectron* 2014; 54: 585–597.

48. Akyazi T, Basabe-Desmonts L, Benito-Lopez F. Review on microfluidic paper-based analytical devices towards commercialisation. *Anal Chim Acta* 2018; 1001: 1–17.

49. Becker H, Gärtner C. Polymer microfabrication technologies for microfluidic systems. *Anal Bioanal Chem* 2008; 390: 89–111.

50. Campo a Del, Greiner C. SU-8: a photoresist for high-aspect-ratio and 3D submicron lithography. *J Micromechanics Microengineering* 2007; 17: R81–R95.

51. Mao H, Wu W, She D, Sun G, Lv P, Xu J. Microfluidic Surface-Enhanced Raman Scattering Sensors Based on Nanopillar Forests Realized by an Oxygen-Plasma-Stripping-of-Photoresist Technique. *Small* 2014; 10: 127–134.

52. Novo P, Prazeres DMF, Chu V, Conde JP. Microspot-based ELISA in microfluidics: chemiluminescence and colorimetry detection using integrated thin-film hydrogenated amorphous silicon photodiodes. *Lab Chip* 2011; 11: 4063–71.

53. Qin D, Xia Y, Whitesides GM. Soft lithography for micro- and nanoscale patterning. *Nat Protoc* 2010; 5: 491–502.

54. Whitesides GM, Ostuni E, Takayama S, Jiang X, Ingber DE. Soft Lithography in Biology and Biochemistry. *Annu Rev Biomed Eng* 2001; 3: 335–373.

55. Kricka LJ, Fortina P, Panaro NJ, Wilding P, Alonso-Amigo G, Becker H. Fabrication of plastic microchips by hot embossing. *Lab Chip* 2002; 2: 1.

56. Jaszewski RW, Schift H, Gobrecht J, Smith P. Hot embossing in polymers as a direct way to pattern resist. *Microelectron Eng* 1998; 41–42: 575–578.

57. Heyderman LJ, Schift H, David C, Ketterer B, Auf der Maur M, Gobrecht J. Nanofabrication using hot embossing lithography and electroforming. *Microelectron Eng* 2001; 57–58: 375–380.

58. Lee G-B, Chen S-H, Huang G-R, Sung W-C, Lin Y-H. Microfabricated plastic chips by hot embossing methods and their applications for DNA separation and detection. *Sensors Actuators B Chem* 2001; 75: 142–148.

59. Yin Z, Cheng E, Zou H, Chen L, Xu S. Fabrication of two dimensional polyethylene terephthalate nanofluidic chip using hot embossing and thermal bonding technique. *Biomicrofluidics* 2014; 8: 066503.

60. Laksanasopin T, Guo TW, Nayak S, Sridhara A a, Xie S, Olowookere OO, Cadinu P, Meng F, Chee NH, Kim J, Chin CD, Munyazesa E, Mugwaneza P, Rai AJ, Mugisha V, Castro AR, Steinmiller D, Linder V, Justman JE, Nsanzimana S, Sia SK. A smartphone dongle for diagnosis of infectious diseases at the point of care. *Sci Transl Med* 2015; 7: 273re1.

61. Ahn CH, Choi J-W, Beaucage G, Nevin J, Lee J-B, Puntambekar a., Lee RJY. Disposable Smart Lab on a Chip for Point-of-Care Clinical Diagnostics. *Proc IEEE* 2004; 92: 154–173.

62. Ben azouz A. *Microfluidic Device Prototyping via Laser Processing of Glass and Polymer Materials*. Dublin City University, 2013.

63. Hnatovsky C, Taylor RS, Simova E, Rajeev PP, Rayner DM, Bhardwaj VR, Corkum PB. Fabrication of microchannels in glass using focused femtosecond laser radiation and selective chemical etching. *Appl Phys A* 2006; 84: 47–61.

64. Lorenz H, Despont M, Fahrni N, LaBianca N, Renaud P. SU-8 : a low-cost negative resist for MEMS. *J Microelectromechanical Syst* 1997; 121: 2–6.

65. Mitri E, Birarda G, Vaccari L, Kenig S, Tormen M, Grenci G. SU-8 bonding protocol for the fabrication of microfluidic devices dedicated to FTIR microspectroscopy of live cells. *Lab Chip* 2014; 14: 210–8.

66. Nemani K V., Moodie KL, Brennick JB, Su A, Gimi B. In vitro and in vivo evaluation of SU-8 biocompatibility. *Mater Sci Eng C* 2013; 33: 4453–4459.

67. Esch MB, Kapur S, Irizarry G, Genova V. Influence of master fabrication techniques on the characteristics of embossed microfluidic channels. *Lab Chip* 2003; 3: 121.

68. Jo B-H, Van Lerberghe LM, Motsegood KM, Beebe DJ. Three-dimensional micro-channel fabrication in polydimethylsiloxane (PDMS) elastomer. *J Microelectromechanical Syst* 2000; 9: 76–81.

69. Hofmann O, Niedermann P, Manz A. Modular approach to fabrication of three-dimensional microchannel systems in PDMS—application to sheath flow microchips. *Lab Chip* 2001; 1: 108–114.

70. Yang Y, Li C, Kameoka J, Lee KH, Craighead HG. A polymeric microchip with integrated tips and in situ polymerized monolith for electrospray mass spectrometry. *Lab Chip* 2005; 5: 869–76.

71. Liu J, Chen C-F, Tsao C-W, Chang C-C, Chu C-C, DeVoe DL. Polymer Microchips Integrating Solid-Phase Extraction and High-Performance Liquid Chromatography Using Reversed-Phase Polymethacrylate Monoliths. *Anal Chem* 2009; 81: 2545–2554.

72. Liu J, Ro K-W, Nayak R, Knapp DR. Monolithic column plastic microfluidic device for peptide analysis using electrospray from a channel opening on the edge of the device. *Int J Mass Spectrom* 2007; 259: 65–72.

73. Chemical Retrieval on the Web (CROW). Polymer Properties Database. *CROW's Polymer Physics* www.polymerdatabase.com (2018, accessed 5 June 2018).

74. Zeon Corporation. ZEONOR COP Technical Data Sheet http://www.zeon.co.jp/content/200181692.pdf (2012, accessed 5 June 2018).

75. Zeon Corporation. ZEONEX COP Technical Data Sheet http://www.zeon.co.jp/content/200181690.pdf (2016, accessed 5 June 2018).

76. Iliescu C, Taylor H, Avram M, Miao J, Franssila S. A practical guide for the fabrication of microfluidic devices using glass and silicon. *Biomicrofluidics* 2012; 6: 016505.

77. Becker H, Gärtner C. Polymer microfabrication methods for microfluidic analytical applications. *Electrophoresis* 2000; 21: 12–26.

78. Mair D a, Rolandi M, Snauko M, Noroski R, Svec F, Fréchet JMJ. Room-Temperature Bonding for Plastic High-Pressure Microfluidic Chips. *Anal Chem* 2007; 79: 5097–5102.

79. Ogilvie IRG, Sieben VJ, Floquet CF a, Zmijan R, Mowlem MC, Morgan H. Solvent processing of PMMA and COC chips for bonding devices with optical quality surfaces. *14th Int Conf Miniaturized Syst Chem Life Sci* 2010; 1244–1246.

80. Mecomber JS, Stalcup AM, Hurd D, Halsall HB, Heineman WR, Seliskar CJ, Wehmeyer KR, Limbach PA. Analytical Performance of Polymer-Based Microfluidic Devices Fabricated By Computer Numerical Controlled Machining. *Anal Chem* 2006; 78: 936–941.

81. Ben Azouz A, Vázquez M, Brabazon D. Developments of Laser Fabrication Methods for Lab-on-a-Chip Microfluidic Multisensing Devices. In: Hashmi S (ed) *Comprehensive Materials Processing*. Oxford, UK: Elsevier Ltd, 2014, pp. 447–458.

82. Nwankire CE, Czugala M, Burger R, Fraser KJ, O'Connell TM, Glennon T, Onwuliri BE, Nduaguibe IE, Diamond D, Ducrée J. A portable centrifugal analyser for liver function screening. *Biosens Bioelectron* 2014; 56: 352–358.

83. Duffy E, Padovani R, He X, Gorkin R, Vereshchagina E, Ducrée J, Nesterenko E, Nesterenko PN, Brabazon D, Paull B, Vázquez M. New strategies for stationary phase integration within centrifugal microfluidic platforms for applications in sample preparation and pre-concentration. *Anal Methods* . Epub ahead of print 2017. DOI: 10.1039/C7AY00127D.

84. Islam M, Natu R, Martinez-Duarte R. A study on the limits and advantages of using a desktop cutter plotter to fabricate microfluidic networks. *Microfluid Nanofluidics* 2015; 19: 973–985.

85. Vázquez M, Brabazon D, Shang F, Omamogho JO, Glennon JD, Paull B. Centrifugally-driven sample extraction, preconcentration and purification in microfluidic compact discs. *TrAC Trends Anal Chem* 2011; 30: 1575–1586.

86. Shah S, Senapati S, Klacsmann F, Miller D, Johnson J, Chang H-C, Stack M. Current Technologies and Recent Developments for Screening of HPV-Associated Cervical and Oropharyngeal Cancers. *Cancers (Basel)* 2016; 8: 85.

87. Focke M, Kosse D, Müller C, Reinecke H, Zengerle R, von Stetten F. Lab-on-a-Foil: microfluidics on thin and flexible films. *Lab Chip* 2010; 10: 1365.

88. Sugioka K, Hanada Y, Midorikawa K. 3D Microstructuring of Glass By Femtosecond Laser Direct Writing and Application To Biophotonic Microchips. *Prog Electromagn Res Lett* 2008; 1: 181–188.

89. De Marco C, Suriano R, Levi M, Turri S, Eaton S, Cerullo G, Osellame R. Femtosecond laser fabrication and characterization of microchannels and waveguides in methacrylate-based polymers. *Microsyst Technol* 2011; 18: 183–190.

90. Nejadmalayeri AH, Herman PR, Burghoff J, Will M, Nolte S, Tünnermann A. Inscription of optical waveguides in crystalline silicon by mid-infrared femtosecond laser pulses. *Opt Lett* 2005; 30: 964.

91. Marcinkevicius A, Juodkazis S, Mizeikis V, Watanabe M, Matsuo S, Nishii J, Misawa H. Fabrication of 3D interconnected network of microchannels inside silica by femtosecond irradiation and etching. In: Gower MC, Helvajian H, Sugioka K, Dubowski JJ (eds) *Laser Applications in Microelectronic and*

Optoelectronic Manufacturing VI. SPIE Proceeedings, 2001, pp. 469–477.

92. Xu B-B, Zhang Y-L, Xia H, Dong W-F, Ding H, Sun H-B. Fabrication and multifunction integration of microfluidic chips by femtosecond laser direct writing. *Lab Chip* 2013; 13: 1677.

93. Sugioka K, Cheng Y. Femtosecond laser processing for optofluidic fabrication. *Lab Chip* 2012; 12: 3576.

94. Bellouard Y. The Femtoprint Project. *J Laser Micro/Nanoengineering* 2012; 7: 1–10.

95. Briggs M, Clements H, Wynne N, Rennie A, Kellett D. 3D printed facial laser scans for the production of localised radiotherapy treatment masks – A case study. *J Vis Commun Med* 2016; 39: 99–104.

96. Lupeanu M, Rennie A, Eggbeer D, Neagu C. Redesign of custom-fitted surgical guide with targeted functional analysis fabricated via SLM. In: Rennie AEW, Bocking CE (eds) *Rapid Design, Prototyping and Manufacturing: Proceedings of the twelfth conference on*. Lancaster: CRDM Ltd, 2011, pp. 173–181.

97. Huang Y, Leu MC, Mazumder J, Donmez A. Additive Manufacturing: Current State, Future Potential, Gaps and Needs, and Recommendations. *J Manuf Sci Eng* 2015; 137: 014001.

98. Guo Q, Cai X, Wang X, Yang J. "Paintable" 3D printed structures via a post-ATRP process with antimicrobial function for biomedical applications. *J Mater Chem B* 2013; 1: 6644.

99. Crump SS. *Apparatus and method for creating three-dimensional objects*. US Patent 5,121,329, US: United States Patent and Trademark Office, 1992.

100. Tsuda S, Jaffery H, Doran D, Hezwani M, Robbins PJ, Yoshida M, Cronin L. Customizable 3D Printed 'Plug and Play' Millifluidic Devices for Programmable Fluidics. *PLoS One* 2015; 10: e0141640.

101. Symes MD, Kitson PJ, Yan J, Richmond CJ, Cooper GJT, Bowman RW, Vilbrandt T, Cronin L. Integrated 3D-printed reactionware for chemical synthesis and analysis. *Nat Chem* 2012; 4: 349–354.

102. Dragone V, Sans V, Rosnes MH, Kitson PJ, Cronin L. 3D-printed devices for continuous-flow organic chemistry. *Beilstein J Org Chem* 2013; 9: 951–959.

103. Kitson PJ, Rosnes MH, Sans V, Dragone V, Cronin L. Configurable 3D-Printed millifluidic and microfluidic 'lab on a chip' reactionware devices. *Lab Chip* 2012; 12: 3267.

104. Kitson PJ, Symes MD, Dragone V, Cronin L. Combining 3D printing and liquid handling to produce user-friendly reactionware for chemical synthesis and purification. *Chem Sci* 2013; 4: 3099–3103.

105. Mathieson JS, Rosnes MH, Sans V, Kitson PJ, Cronin L. Continuous parallel ESI-MS analysis of reactions carried out in a bespoke 3D printed device. *Beilstein J Nanotechnol* 2013; 4: 285–291.

106. Morgan AJL, Hidalgo San Jose L, Jamieson WD, Wymant JM, Song B, Stephens P, Barrow DA, Castell OK. Simple and Versatile 3D Printed Microfluidics Using Fused Filament Fabrication. *PLoS One* 2016; 11: e0152023.

107. Gaal G, Mendes M, de Almeida TP, Piazzetta MHO, Gobbi ÂL, Riul A, Rodrigues V. Simplified fabrication of integrated microfluidic devices using fused deposition modeling 3D printing. *Sensors Actuators B Chem* 2017; 242: 35–40.

108. Krejcova L, Nejdl L, Rodrigo MAM, Zurek M, Matousek M, Hynek D, Zitka O, Kopel P, Adam V, Kizek R. 3D printed chip for electrochemical detection of influenza virus labeled with CdS quantum dots. *Biosens Bioelectron* 2014; 54: 421–427.

109. Moore JL, McCuiston A, Mittendorf I, Ottway R, Johnson RD. Behavior of capillary valves in centrifugal microfluidic devices prepared by three-dimensional printing. *Microfluid Nanofluidics* 2010; 10: 877–888.

110. Fee C, Nawada S, Dimartino S. 3D printed porous media columns with fine control of column packing morphology. *J Chromatogr A* 2014; 1333: 18–24.

111. Anderson KB, Lockwood SY, Martin RS, Spence DM. A 3D Printed Fluidic Device that Enables Integrated Features. *Anal Chem* 2013; 85: 5622–5626.

112. Erkal JL, Selimovic A, Gross BC, Lockwood SY, Walton EL, McNamara S, Martin RS, Spence DM. 3D printed microfluidic devices with integrated versatile and reusable electrodes. *Lab Chip* 2014; 14: 2023–2032.

113. Kruth J, Badrossamay M, Yasa E, Deckers J, Thijs L, Humbeeck J Van. Part and material properties in selective laser melting of metals. *16th Int Symp Electromachining* 2010; 1–12.

114. Nelson J, Galloway G, Rennie AEW, Abram TN, Bennett GR. Effects of scan direction and orientation on mechanical properties of laser sintered polyamide-12. *Int J Adv Des Manuf Technol* 2014; 7: 19–25.

115. Burns N, Burns M, Travis D, Geekie L, Rennie AEW. Designing Advanced Filtration Media through Metal Additive Manufacturing. *Chem Eng Technol* 2016; 39: 535–542.

116. Hasib H, Rennie A, Burns N, Geekie L. Pressure drop and velocity simulations in non-stochastic lattice structure for filter applications fabricated using additive manufacturing. *Filtr Soc* 2016; 16: 97–102.

117. Capel AJ, Edmondson S, Christie SDR, Goodridge RD, Bibb RJ, Thurstans M. Design and additive manufacture for flow chemistry. *Lab Chip* 2013; 13: 4583.

118. Gibson I, Rosen D, Stucker B. *Additive Manufacturing Technologies*. 2nd ed. New York, NY, US: Springer New York, 2015.

119. Hull CW. *Apparatus for production of three-dimensional objects by stereolithography*. US Patent 4,575,330, US: United States Patent and Trademark Office, 1986.

120. Waldbaur A, Carneiro B, Hettich P, Wilhelm E, Rapp BE. Computer-aided microfluidics (CAMF): from digital 3D-CAD models to physical structures within a day. *Microfluid Nanofluidics* 2013; 15: 625–635.

121. Au AK, Huynh W, Horowitz LF, Folch A. 3D-Printed Microfluidics. *Angew Chemie Int Ed* 2016; 55: 3862–3881.

122. Amin R, Knowlton S, Hart A, Yenilmez B, Ghaderinezhad F, Katebifar S, Messina M, Khademhosseini A, Tasoglu S. 3D-printed microfluidic devices.

Biofabrication 2016; 8: 022001.

123. Gong H, Bickham BP, Woolley AT, Nordin GP. Custom 3D printer and resin for 18 μm × 20 μm microfluidic flow channels. *Lab Chip* 2017; 17: 2899–2909.

124. Honegger T, Elmberg T, Berton K, Peyrade D. Visible microlaser two-photon polymerization in a microfludic cell: A resist study. *Microelectron Eng* 2011; 88: 2725–2728.

125. Ostendorf A, Chichkov BN. Two-photon polymerization: A new approach to micromachining. *Photonics spectra*.

126. Xia H, Wang J, Tian Y, Chen Q-D, Du X-B, Zhang Y-L, He Y, Sun H-B. Ferrofluids for Fabrication of Remotely Controllable Micro-Nanomachines by Two-Photon Polymerization. *Adv Mater* 2010; 22: 3204–3207.

127. Wang J, He Y, Xia H, Niu L-G, Zhang R, Chen Q-D, Zhang Y-L, Li Y-F, Zeng S-J, Qin J-H, Lin B-C, Sun H-B. Embellishment of microfluidic devices via femtosecond laser micronanofabrication for chip functionalization. *Lab Chip* 2010; 10: 1993–1996.

128. Waheed S, Cabot JM, Macdonald NP, Lewis T, Guijt RM, Paull B, Breadmore MC. 3D printed microfluidic devices: enablers and barriers. *Lab Chip* 2016; 16: 1993–2013.

129. Beauchamp MJ, Nordin GP, Woolley AT. Moving from millifluidic to truly microfluidic sub-100-μm cross-section 3D printed devices. *Anal Bioanal Chem* 2017; 409: 4311–4319.

130. Takenaga S, Schneider B, Erbay E, Biselli M, Schnitzler T, Schöning MJ, Wagner T. Fabrication of biocompatible lab-on-chip devices for biomedical applications by means of a 3D-printing process. *Phys status solidi* 2015; 212: 1347–1352.

131. Su C-K, Peng P-J, Sun Y-C. Fully 3D-Printed Preconcentrator for Selective Extraction of Trace Elements in Seawater. *Anal Chem* 2015; 87: 6945–6950.

132. Dawson RJ, Patel AJ, Rennie AEW, White S. An investigation into the use of additive manufacture for the production of metallic bipolar plates for polymer electrolyte fuel cell stacks. *J Appl Electrochem* 2015; 45: 637–645.

133. The Ultimate Guide to Stereolithography (SLA) 3D Printing. *Formlabs website* https://formlabs.com/blog/ultimate-guide-to-stereolithography-sla-3d-printing/ (2017, accessed 11 April 2018).

134. Jacobs PF. Fundamentals of Stereolithography. In: Marcus HL, Beaman JJ, Barlow JW, Bourell DL, Crawford RH (eds) *Solid Freeform Fabrication Symposium: Proceedings of the 3rd*. Austin, Texas: The University of Texas at Austin, 1992, pp. 196–211.

135. Waheed S, Cabot JM, Macdonald NP, Lewis T, Guijt RM, Paull B, Breadmore MC. 3D printed microfluidic devices: enablers and barriers. *Lab Chip* 2016; 16: 1993–2013.

136. Zissi S, Bertsch A, Jézéquel J-Y, Corbel S, Lougnot DJ, André JC. Stereolithography and microtechniques. *Microsyst Technol* 1996; 2: 97–102.

137. Shankar Limaye A, Rosen DW. Compensation zone approach to avoid print-through errors in mask projection stereolithography builds. *Rapid Prototyp J*

2006; 12: 283–291.

138. Shankar Limaye A. *Multi-Objective Process Planning Method For Mask Projection Stereolithography*. Georgia Institute of Technology, 2007.

139. Senapati S, Basuray S, Slouka Z, Cheng L-J, Chang H-C. A Nanomembrane-Based Nucleic Acid Sensing Platform for Portable Diagnostics. In: *Top Curr Chem*. 2011, pp. 153–169.

140. Breadmore MC, Wolfe KA, Arcibal IG, Leung WK, Dickson D, Giordano BC, Power ME, Ferrance JP, Feldman SH, Norris PM, Landers JP. Microchip-based purification of DNA from biological samples. *Anal Chem* 2003; 75: 1880–1886.

141. Cady NC, Stelick S, Batt CA. Nucleic acid purification using microfabricated silicon structures. *Biosens Bioelectron* 2003; 19: 59–66.

142. Zhang L, Rafei SM, Xie L, Chew MBR, Ji HM, Chen Y, Rajoo R, Ong KL, Tan R, Lau SH, Chow VTK, Heng CK, Teo KH, Kang TG. A self-contained disposable cartridge microsystem for dengue viral ribonucleic acid extraction. *Sensors and Actuators B-Chemical* 2011; 160: 1557–1564.

143. Reedy CR, Hagan K a, Strachan BC, Higginson JJ, Bienvenue JM, Greenspoon SA, Ferrance JP, Landers JP. Dual-domain microchip-based process for volume reduction solid phase extraction of nucleic acids from dilute, large volume biological samples. *Anal Chem* 2010; 82: 5669–5678.

144. Senapati S, Slouka Z, Shah SS, Behura SK, Shi Z, Stack MS, Severson DW, Chang HC. An ion-exchange nanomembrane sensor for detection of nucleic acids using a surface charge inversion phenomenon. *Biosens Bioelectron* 2014; 60: 92–100.

145. Drummond TG, Drummond TG, Hill MG, Hill MG, Barton JK, Barton JK. Electrochemical DNA sensors. *Nat Biotechnol* 2003; 21: 1192–9.

146. DETAX Audio. Freeprint Mould Material Safety Data Sheet. 2015; 1–5.

147. Comina G, Suska A, Filippini D. Low cost lab-on-a-chip prototyping with a consumer grade 3D printer. *Lab Chip* 2014; 14: 2978–82.

148. Mott EJ, Busso M, Luo X, Dolder C, Wang MO, Fisher JP, Dean D. Digital micromirror device (DMD)-based 3D printing of poly(propylene fumarate) scaffolds. *Mater Sci Eng C* 2016; 61: 301–311.

149. Shaikh KA, Ryu KS, Goluch ED, Nam J-M, Liu J, Thaxton CS, Chiesl TN, Barron AE, Lu Y, Mirkin CA, Liu C. A modular microfluidic architecture for integrated biochemical analysis. *Proc Natl Acad Sci* 2005; 102: 9745–9750.

150. Yuen PK. SmartBuild–A truly plug-n-play modular microfluidic system. *Lab Chip* 2008; 8: 1374.

151. Langelier SM, Livak-Dahl E, Manzo AJ, Johnson BN, Walter NG, Burns MA. Flexible casting of modular self-aligning microfluidic assembly blocks. *Lab Chip* 2011; 11: 1679.

152. Chen A, Pan T. Three-dimensional fit-to-flow microfluidic assembly. *Biomicrofluidics* 2011; 5: 046505.

153. Bhargava KC, Thompson B, Malmstadt N. Discrete elements for 3D microfluidics. *Proc Natl Acad Sci* 2014; 111: 15013–15018.

154. Sun K, Wang Z, Jiang X. Modular microfluidics for gradient generation. *Lab Chip* 2008; 8: 1536.

155. Fredrickson CK, Fan ZH. Macro-to-micro interfaces for microfluidic devices. *Lab Chip* 2004; 4: 526.

156. van Deemter JJ, Zuiderweg FJ, Klinkenberg A. Longitudinal diffusion and resistance to mass transfer as causes of nonideality in chromatography. *Chem Eng Sci* 1995; 50: 3869–3882.

157. Jacobs PF. *StereoLithography and Other RP&M Technologies: From Rapid Prototyping to Rapid Tooling*. Society of Manufacturing Engineers, 1995.

158. Vitale A, Cabral J. Frontal Conversion and Uniformity in 3D Printing by Photopolymerisation. *Materials (Basel)* 2016; 9: 760.

159. Adzima B. The Ember Printer: An Open Platform for Software, Hardware, and Materials Development. In: *UV&EB WEST Conference, Redondo Beach, CA*. 2015.

160. Asiga Inc. PlasClear Technical Datasheet. *Asiga website* https://www.asiga.com/media/main/files/materials/ (2013, accessed 16 May 2018).

161. Yanyan Tang. *Stereolithography Cure Process Modeling*. Georgia Institute of Technology, 2005.

162. Tang Y, Henderson C, Muzzy J, Rosen DW. Stereolithography cure modelling and simulation. *Int J Mater Prod Technol* 2004; 21: 255.

163. Formlabs Inc. Clear Photopolymer Resin for Form 1+ and Form 2 - Material Properties. *Formlabs website* https://formlabs.com/media/upload/Clear-DataSheet.pdf (2016, accessed 16 May 2018).

164. Formlabs Inc. Clear Photoreactive Resin for Form 1, Form 1+, Form 2 - Safety Data Sheet. *Formlabs website* https://formlabs.com/media/upload/Clear-SDS_u324bsC.pdf (2016, accessed 16 May 2018).

Appendix A Supplementary figures for Chapter 4

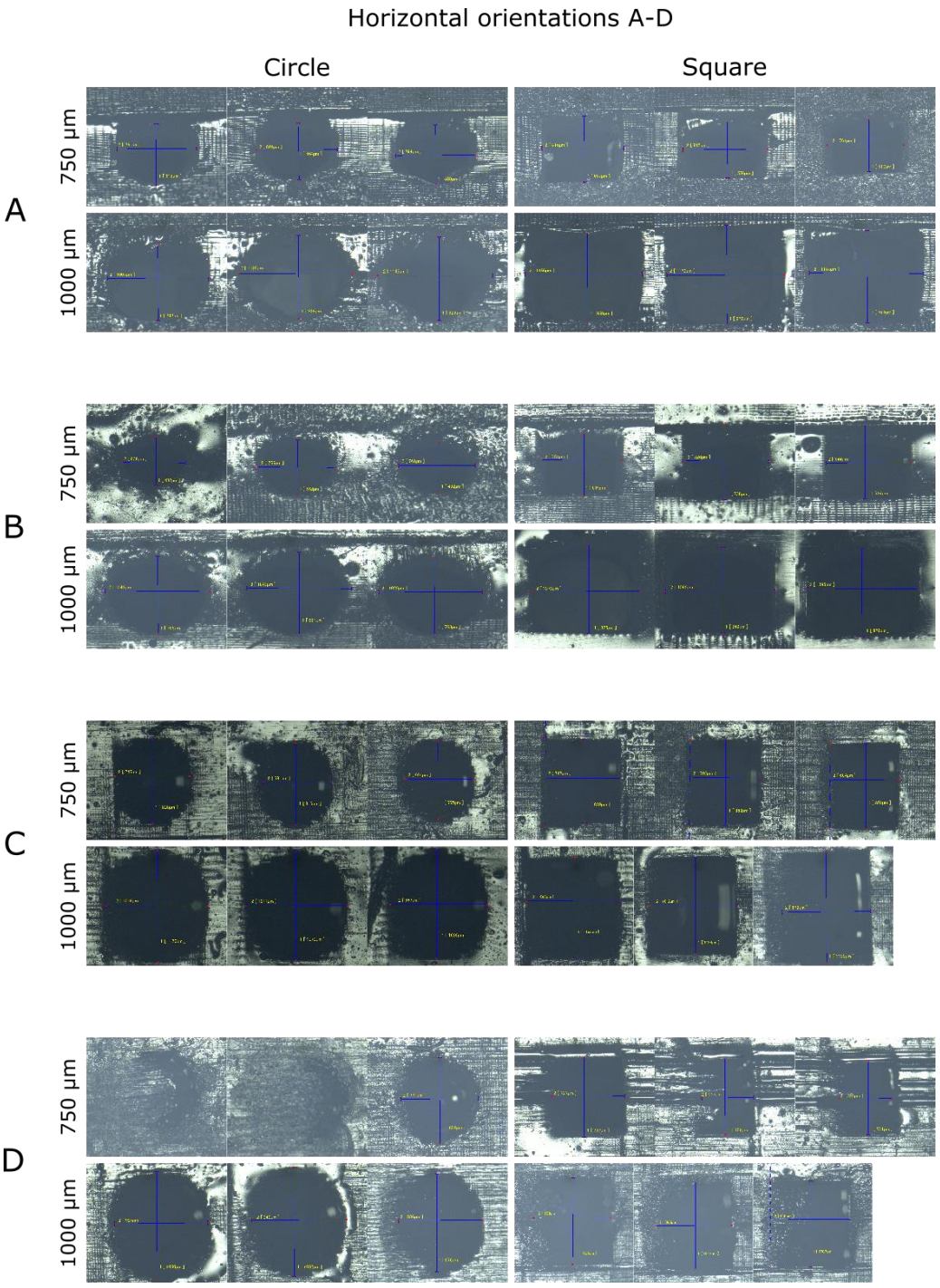

Figure A.1. Microfluidic channels printed in horizontal orientations A-D. Measured values are significantly different from the input dimension according to the Dunnett post-test.

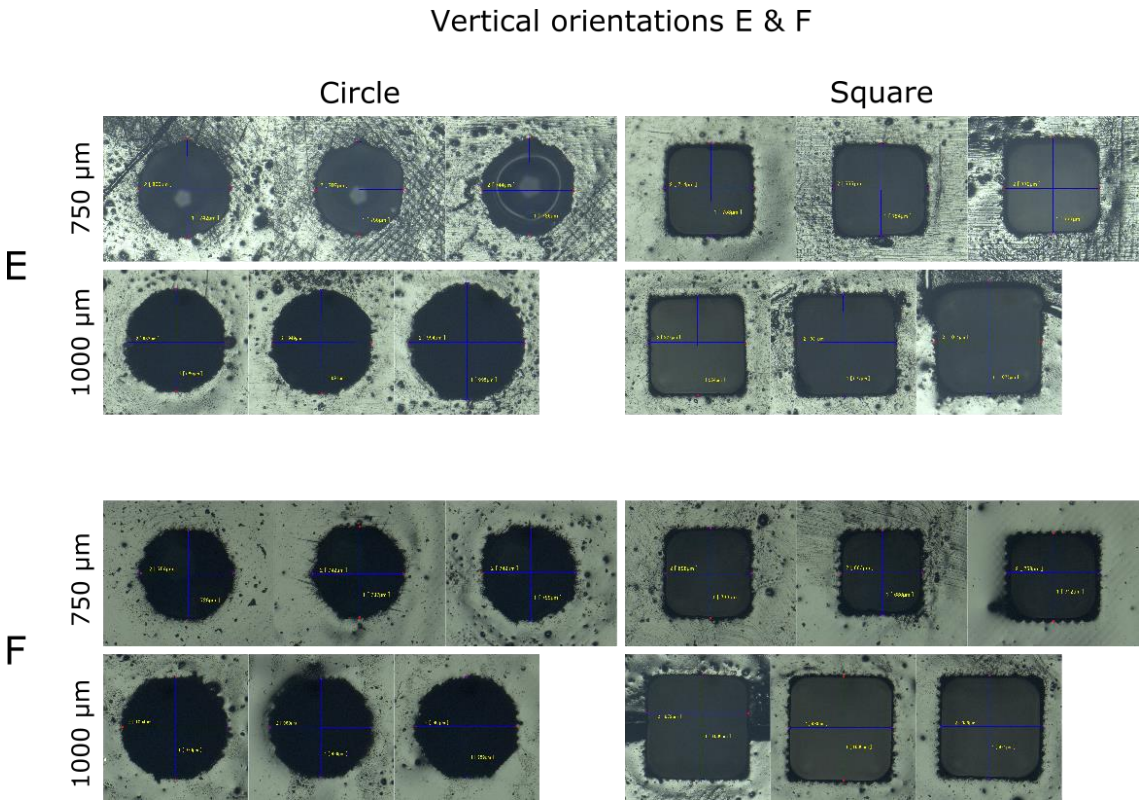

Figure A.2. Microfluidic channels printed in vertical orientations E and F. The Dunnett post-test shows that the measured values for orientations E and F are the only channel measurements to show correlation with the input values for all shapes and input dimensions

Appendix B Photopolymer material data sheets

Freeprint Mould/Shell Material Properties

Product: **Freeprint® mould / shell**

Date: **06.10.2015**

Freeprint ® mould / shell is a light-curing resin, (meth)acrylate based, for the generative production of all types of hard otoplastics, for systems with LED 405 nm.

Property	Test method	Freeprint® mould / shell
Colour	Standard Light Box	In transparent colourless, rose, red and blue; opaque beige and black
Viscosity	CP: gap 0,052 mm, cone 35 mm/ 1°; 23°C, shear rate 80 1/s	622 mPas
Initial hardness without post curing	Zwick H04.3150	74 Shore D
Final hardness	Zwick H04.3150	79 Shore D
Flexural strength	Accord. to DIN EN ISO 178	75 MPa
Flexural Modulus	Accord. to DIN EN ISO 178	1900-2100 MPa

Tests are carried out at 23 °C / 73 °F room temperature (Otoflash 171, 2 times with 2000 flashes, nitrogen). All given data describe the typical properties/values.

The properties depend on the building parameters, the cleaning, drying and post curing process.

Formlabs Clear FLGPCL03 Material Properties[163,164]

	METRIC[1]		IMPERIAL[1]		METHOD
	Green[2]	Postcured[3]	Green[2]	Postcured[3]	
Tensile Properties					
Ultimate Tensile Strength	38 MPa	65 MPa	5510 psi	9380 psi	ASTM D 638-10
Young's Modulus	1.6 GPa	2.8 GPa	234 ksi	402 ksi	ASTM D 638-10
Elongation at Failure	12%	6.2%	12%	6.2%	ASTM D 638-10
Flexural Properties					
Flexural Modulus	1.25 GPa	2.2 GPa	181 ksi	320 ksi	ASTM C 790-10
Impact Properties					
Notched IZOD	16 J/m	25 J/m	0.3 ft-lbf/in	0.46 ft-lbf/in	ASTM D 256-10
Temperature Properties					
Heat deflection temp. @ 264 psi	42.7 °C	58.4 °C	108.9 °F	137.1 °F	ASTM D 648-07
Heat deflection temp. @ 66 psi	49.7 °C	73.1 °C	121.5 °F	163.6 °F	ASTM D 648-07

NOTES:

[1]Material properties can vary with part geometry, print orientation, print settings and temperature.

[2]Data was obtained from green parts, printed using Form 2, 100 µm, Clear settings, without additional treatments.

[3] Data was obtained from parts printed using Form 2, 100 µm, Clear settings and post-cured with 1.25 mW/cm² of 405 nm LED light at 60 °C for 60 minutes.

Percent weight gain over 24 hours for a printed and post-cured 1 x 1 x 1 cm cube immersed in respective solvent:

Mechanical Properties	24 HR WEIGHT GAIN (%)
Acetic Acid, 5 %	< 1
Acetone	sample cracked
Isopropyl Alcohol	< 1
Bleach, ~5 % NaOCl	< 1
Butyl Acetate	< 1
Diesel	< 1
Diethyl glycol monomethyl ether	1.7
Hydrolic Oil	< 1
Skydrol 5	1
Hydrogen Peroxide (3 %)	< 1
Isooctane	< 1
Mineral Oil, light	< 1
Mineral Oil, heavy	< 1
Salt Water (3.5 % NaCl)	< 1
Sodium hydroxide (0.025 %, pH = 10)	< 1
Water	< 1
Xylene	< 1
Strong Acid (HCl Conc)	distorted

	Value	Unit	Method
Specific Gravity	1.09 – 1.12	g/cm^3	
Boiling Point	> 100	°C	
Flash Point	> 100	°C	
Ignition Temperature	no data		
Lower Explosion Limit	no data		
Upper Explosion Limit	no data		
Viscosity	850 – 900	cps	@ 25 °C (77 °F)

Vapour Pressure: Not established
Solubility in Water: Only very slightly soluble
Solubility in Organic Solvents: Soluble in organic solvents
Volatile Characteristics: Negligible
Electrostatic Discharge: Safe
Electric Conductivity: Dielectric

Appendix C Supplementary figures for Chapter 6

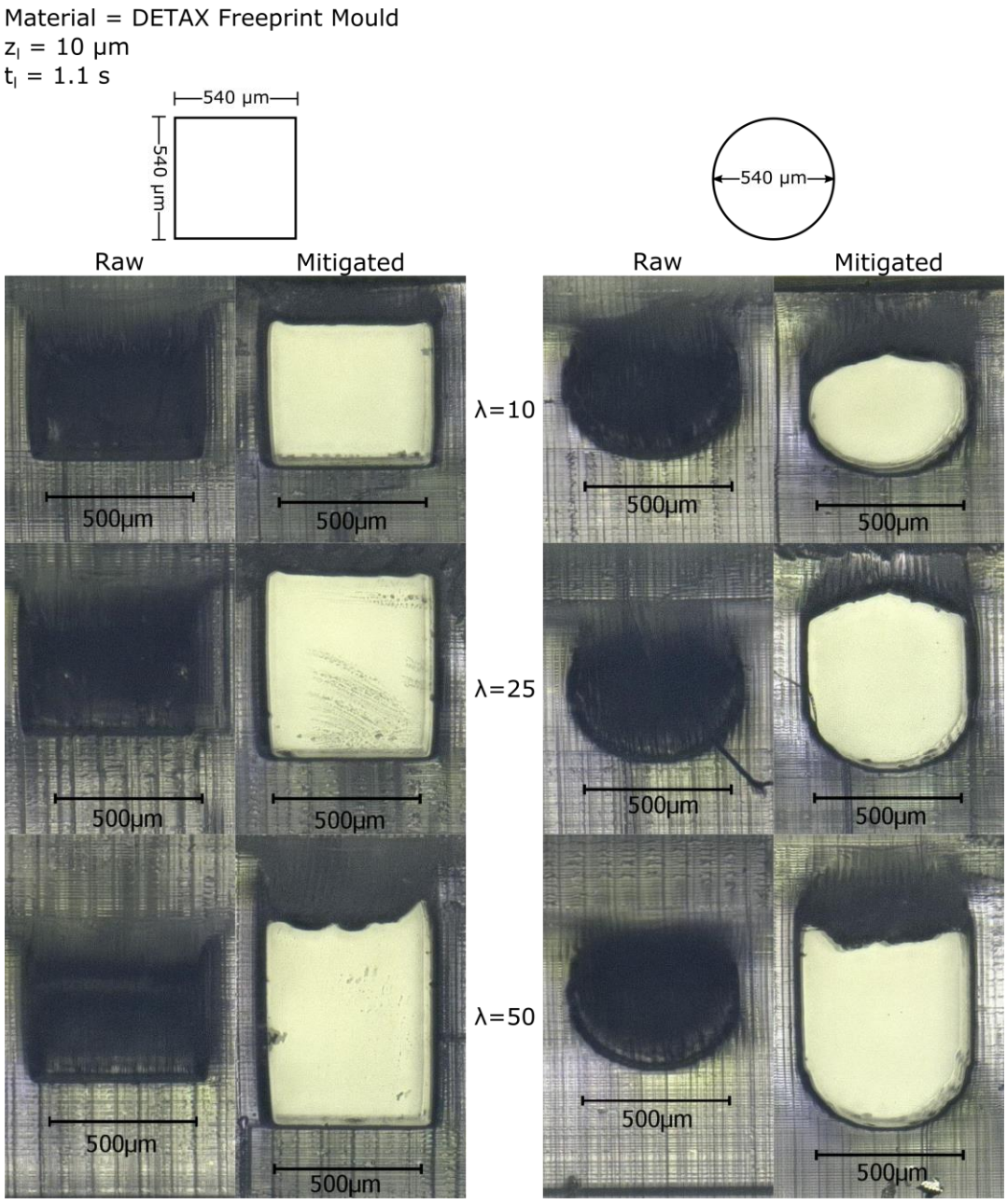

Figure C.1. Raw (unmodified) and mitigated (modified) microfluidic channel models printed in DETAX Freeprint mould photopolymer resin with slice thickness and exposure time settings $z_l = 10$ µm, and $t_l = 1.1$ s respectively.

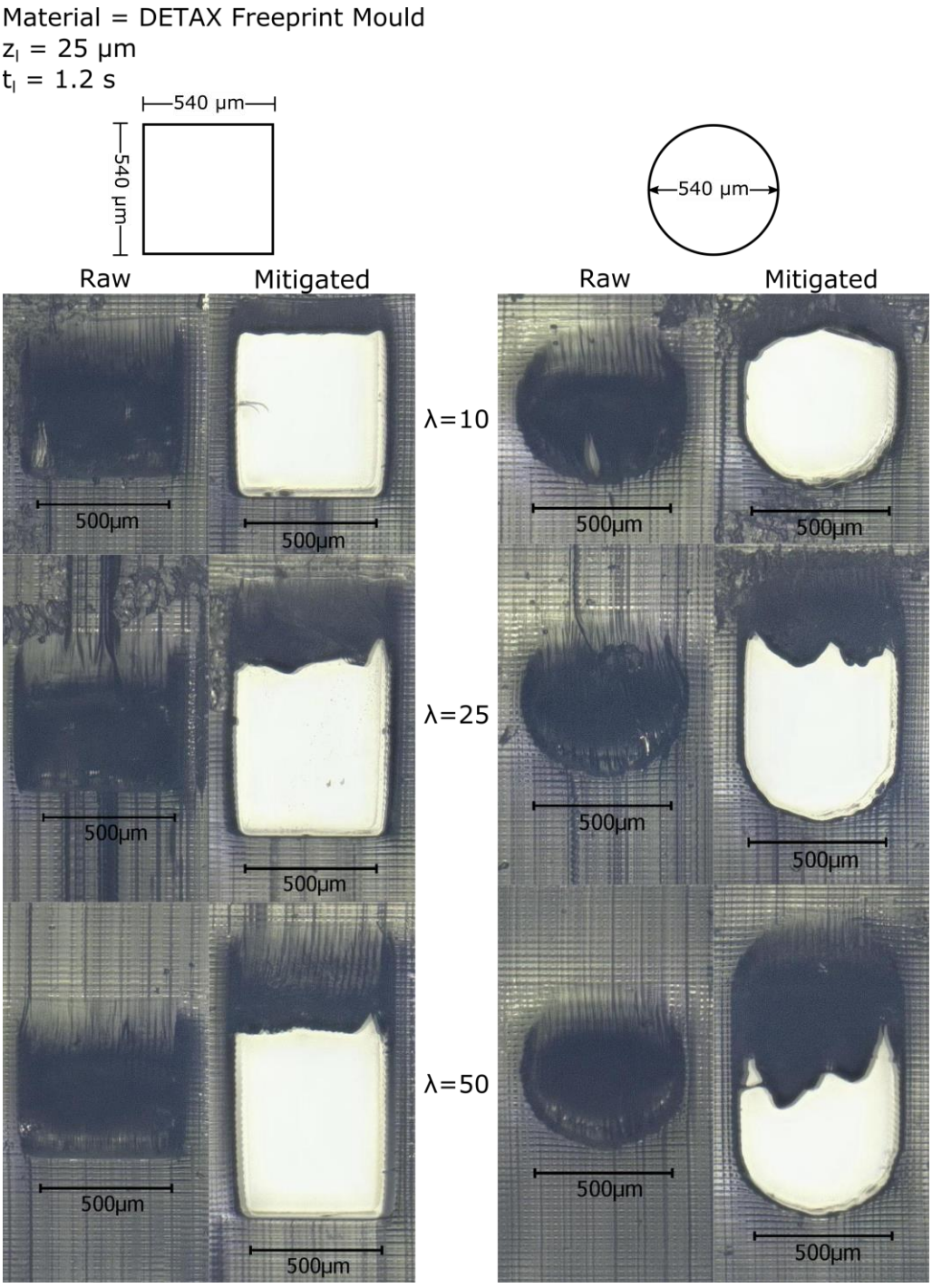

Figure C.2. Raw (unmodified) and mitigated (modified) microfluidic channel models printed in DETAX Freeprint mould photopolymer resin with slice thickness and exposure time settings $z_l = 25$ µm, and $t_l = 1.2$ s respectively.

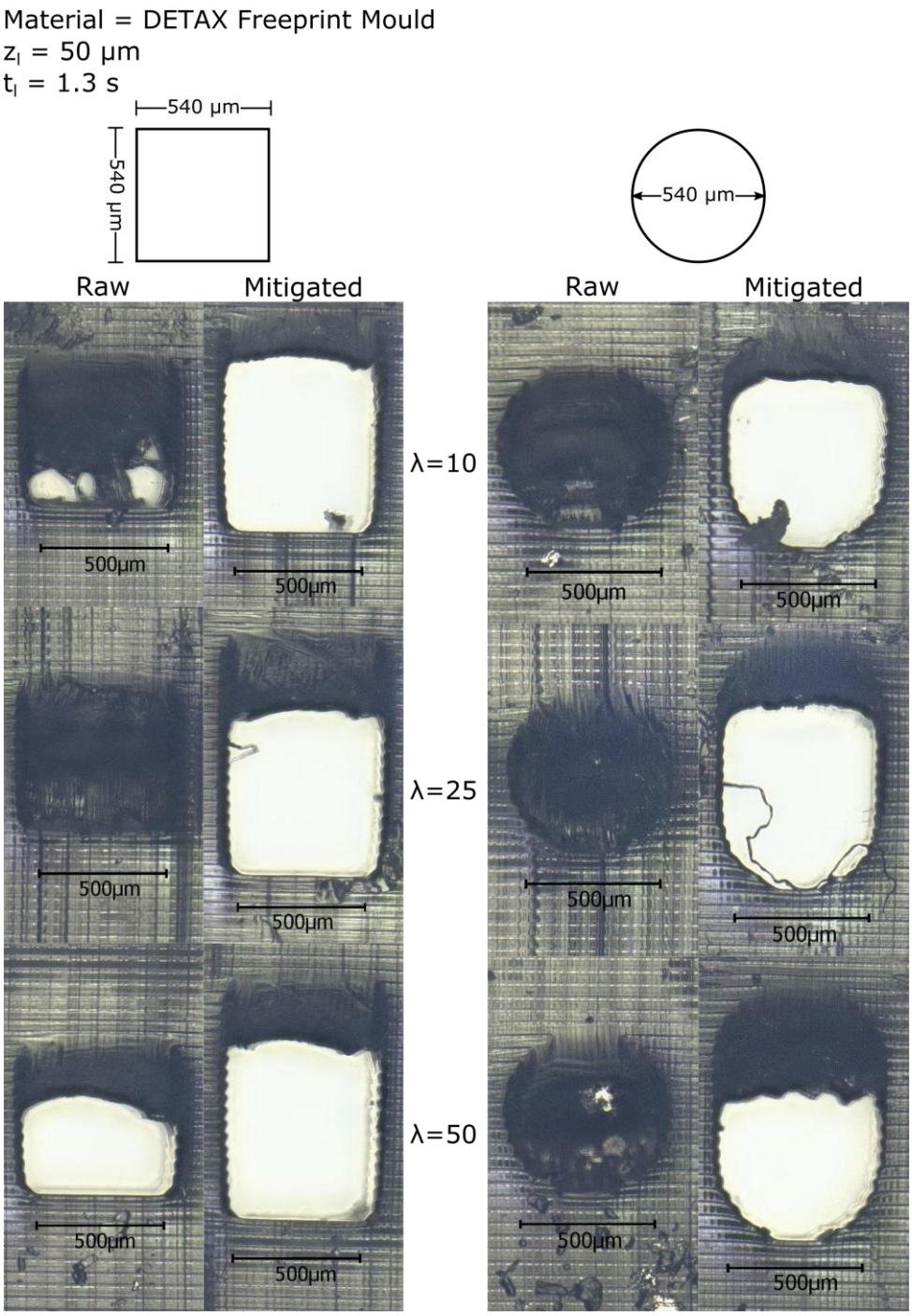

Figure C.3. Raw (unmodified) and mitigated (modified) microfluidic channel models printed in DETAX Freeprint mould photopolymer resin with slice thickness and exposure time settings $z_l = 50$ µm, and $t_l = 1.3$ s respectively.

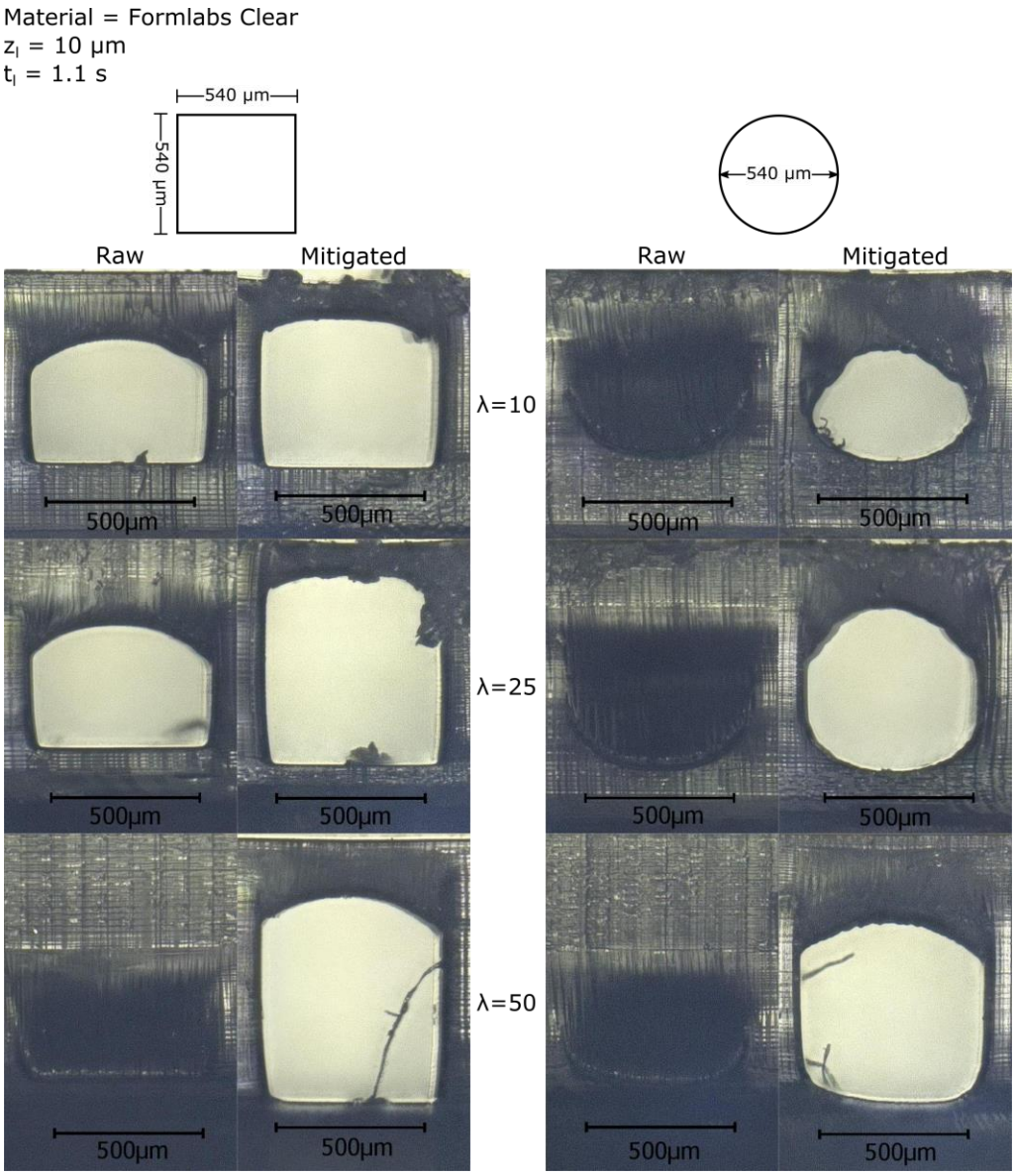

Figure C.4. Raw (unmodified) and mitigated (modified) microfluidic channel models printed in Formlabs Clear photopolymer resin with slice thickness and exposure time settings $z_l = 10$ µm, and $t_l = 1.1$ s respectively.

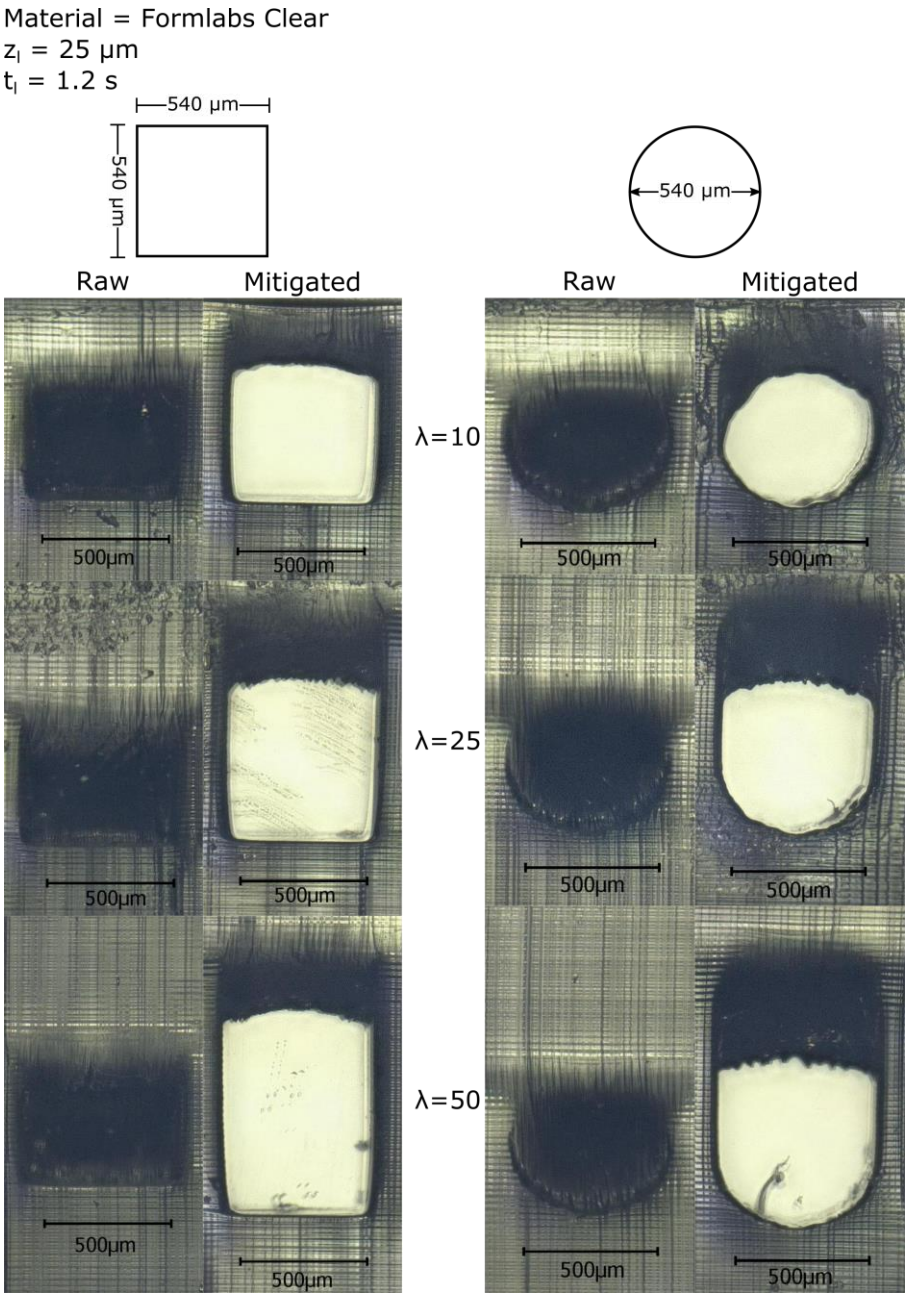

Figure C.5. Raw (unmodified) and mitigated (modified) microfluidic channel models printed in Formlabs Clear photopolymer resin with slice thickness and exposure time settings $z_l = 25$ µm, and $t_l = 1.2$ s respectively.

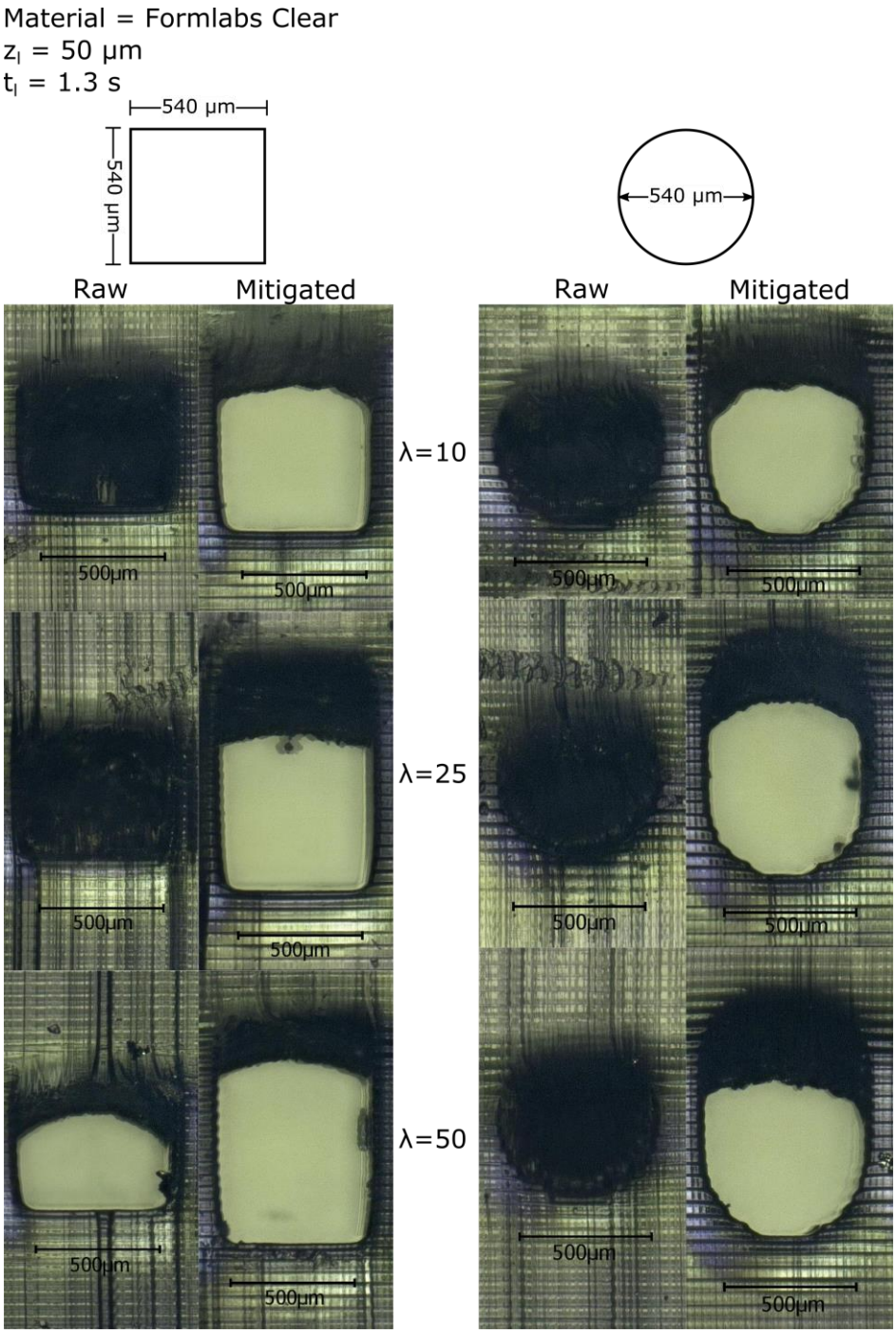

Figure C.6. Raw (unmodified) and mitigated (modified) microfluidic channel models printed in Formlabs Clear photopolymer resin with slice thickness and exposure time settings $z_l = 50$ µm, and $t_l = 1.3$ s respectively.

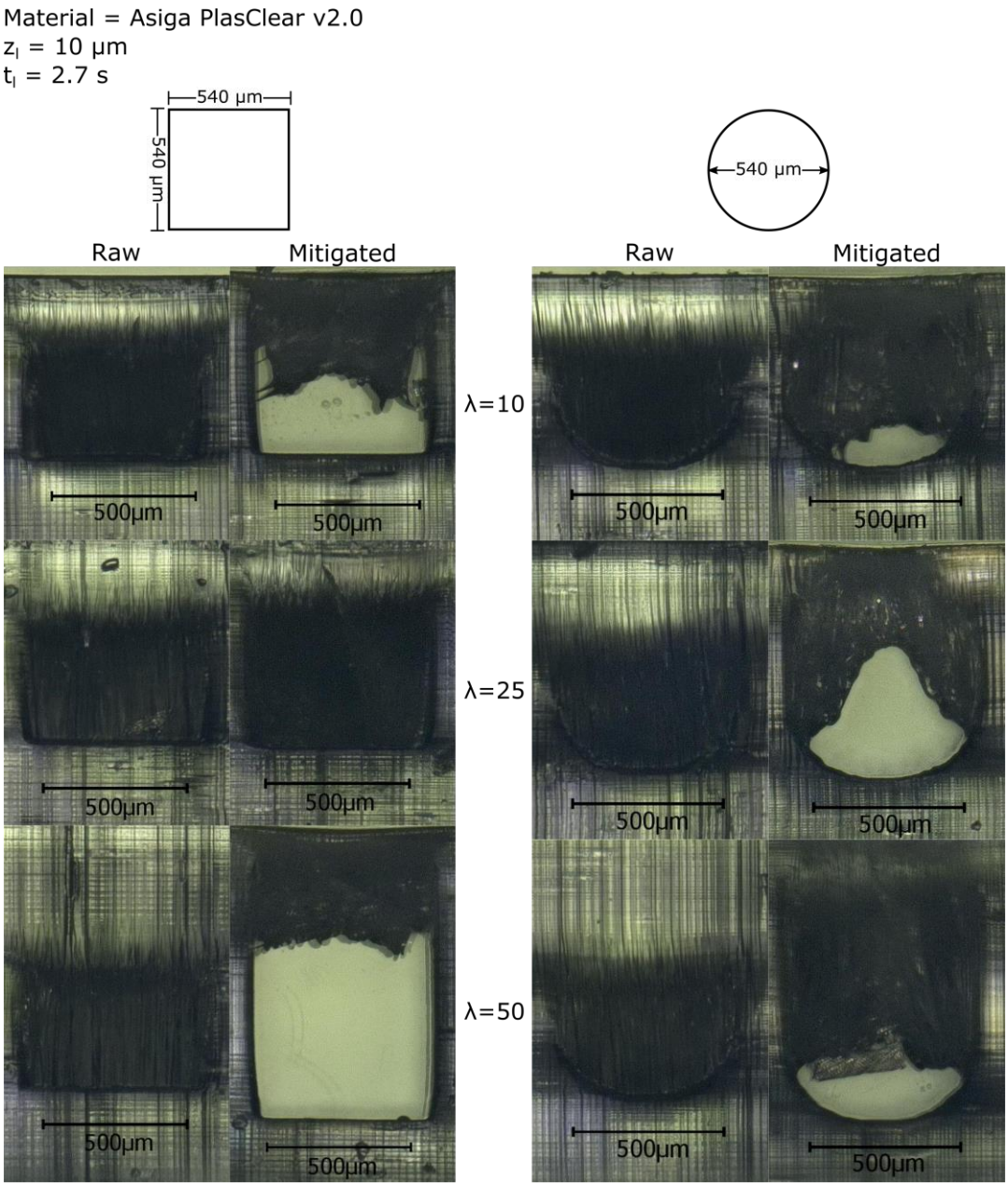

Figure C.7. Raw (unmodified) and mitigated (modified) microfluidic channel models printed in Asiga PlasClear v2.0 photopolymer resin with slice thickness and exposure time settings $z_l = 10$ µm, and $t_l = 2.7$ s respectively.

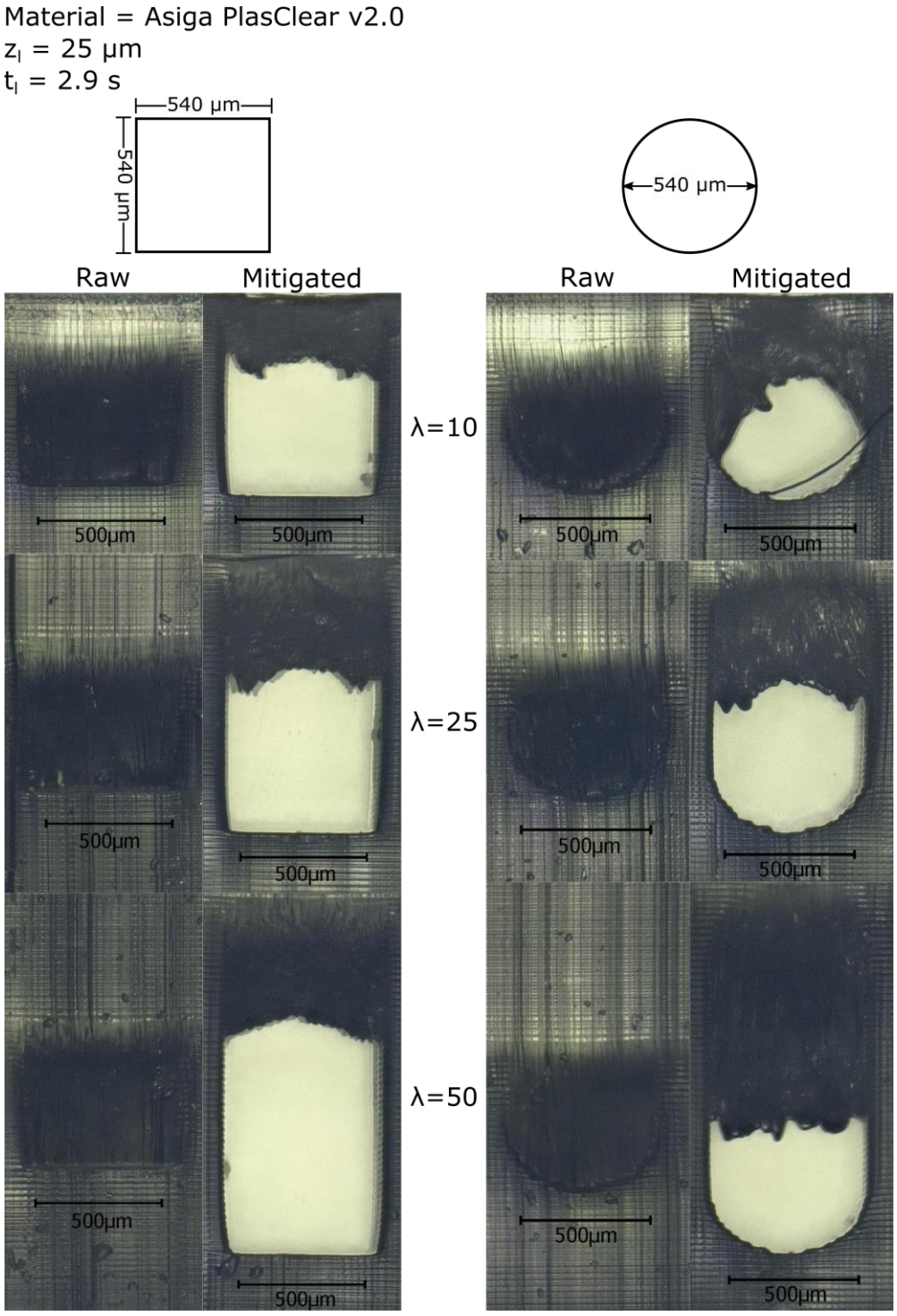

Figure C.8. Raw (unmodified) and mitigated (modified) microfluidic channel models printed in Asiga PlasClear v2.0 photopolymer resin with slice thickness and exposure time settings $z_l = 25$ µm, and $t_l = 2.9$ s respectively.

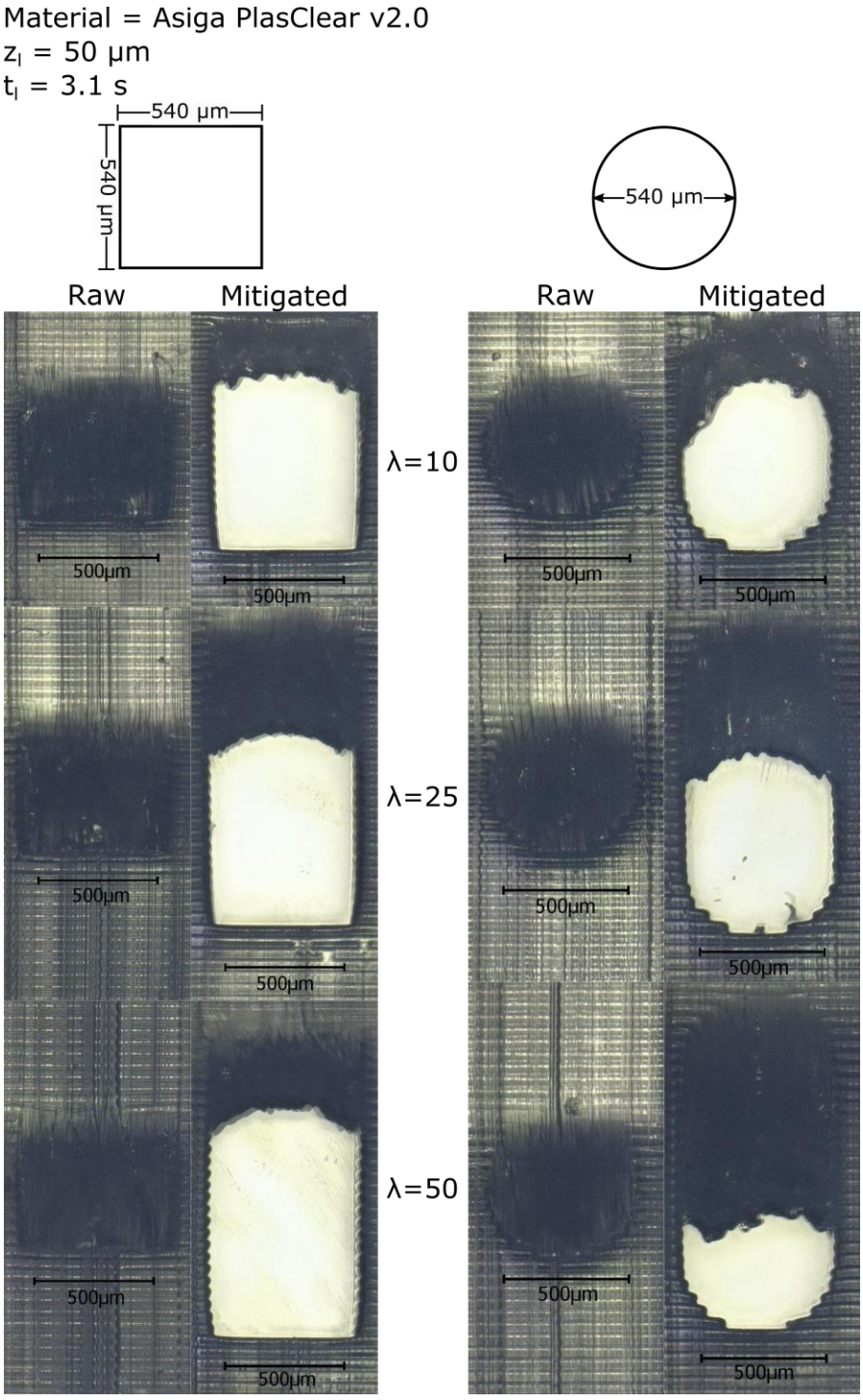

Figure C.9. Raw (unmodified) and mitigated (modified) microfluidic channel models printed in Asiga PlasClear v2.0 photopolymer resin with slice thickness and exposure time settings $z_l = 50$ µm, and $t_l = 3.1$ s respectively.